CZECH TECHNICAL UNIVERSITY IN PRAGUE

Faculty of Civil Engineering

Department of Mechanics

Design of a porous metal structure for use in intraosseous parts of dental and orthopedic implants

Návrh porézní kovové struktury nitrokostních částí dentálních a ortopedických implantátů

DOCTORAL THESIS

Ing. Luboš Řehounek

Doctoral Study Program: Civil Engineering
Branch of Study: Physical and Materials Engineering

Doctoral thesis tutor:	doc. Ing. Jan Vorel, Ph.D.
Doctoral thesis specialist tutor:	doc. Ing. Aleš Jíra, Ph.D.

Prague, 2023

CONFLICT OF INTEREST STATEMENT

Doctoral student's name: Luboš Řehounek

Name of dissertation: Design of a porous metal structure for use in intraosseous parts of dental and orthopedic implants

As the author of this dissertation, I declare no conflict of interest. I claim I wrote this dissertation solely myself, provided with professional consultations from my specialist tutor doc. Ing. Aleš Jíra, Ph.D. and my tutor doc. Ing. Jan Vorel, Ph.D.

I also declare that I abided by the Methodical guideline No. 1/2009 for adhering to ethical principles when elaborating an academic final thesis. All literature and materials used in the writing of this dissertation are properly cited in References.

Prague, 13.10.2023 Signature

https://doi.org/10.14311/dis.fsv.2023.016

Acknowledgment

I want to express gratitude toward my specialist tutor, Mr. Aleš Jíra, whose expert guidance I always appreciated throughout my university studies. I also appreciate the editorial and practical advice of my tutor, doc. Ing. Jan Vorel, Ph.D. I would also like to thank Mr. Hideyuki Mimata from RCCM, Japan, who provided me with clinical data for the numerical model.

Abstract

This thesis outlines the basic biological and mechanical requirements for intraosseous parts of implants equipped with porous parts and emphasizes dental restorations, where small dimensions of implants seem to provide geometrically challenging but nonetheless beneficial integration of porous layers. Porous structures offer a unique way of matching the global modulus of the implant with bone by reducing the stiffness of the implant. This reduction of stiffness is advantageous as it reduces the stress shielding effect. The design, 3D modeling of the porous structure, investigation of its properties and development of a gyroid-equipped dental implant and its numerical quantitative computed tomography-based finite element analysis (QCT/FEA) model were given the most attention. The gyroid is a porous structure that has recently been rapidly emerging in scientific literature and has taken a significant foothold in restorative medicine, reportedly reducing the stress shielding effect and improving clinical performance. The optimal pore size and wall width were determined from the literature research and previous experiments. The most suitable materials and means of production of porous structures are discussed, as are complications that arise when 3D printing fine trabeculae and walls. Multiple variants of the gyroid and trabecular structures were 3D-printed for mechanical tests, and their evaluation was confronted with a QCT/FEA model of the human mandible of an anonymous patient with a custom-designed gyroid-equipped dental implant. The simulations show that implant bodies with lower moduli provide favorable stress distributions in bone and lower peaks of stress. The work also concludes that the optimal global modulus of the structure should be ca. three to ten GPa.

Keywords: Gyroid, Porous, Dental, Implant, Stress Shielding, QCT/FEA.

Abstrakt

Tato práce se zaměřuje na biologické a mechanické požadavky na nitrokostní části implantátů s porézními povrchovými strukturami a dává důraz na aplikaci v dentálních implantátech, kde malé rozměry implantátů představují náročnější, ale neméně přínosnou integraci povrchových vrstev. Porézní struktury představují unikátní způsob sjednocení globálního modulu pružnosti kosti a implantátu snížením tuhosti implantátu. Tato redukce tuhosti je přínosná, protože snižuje účinek napěťového štítu. Největší pozornost byla věnována návrhu a 3D modelování porézní struktury, zkoumání jejích vlastností a vývoji gyroidního dentálního implantátu a jeho numerického modelu. Gyroid je porézní struktura, která se ve vědecké literatuře objevuje čím dále častěji a zajistila si již své vlastní místo v oblasti náhrad, kde je její výhodou redukce napěťového štítu a zlepšování klinické funkce. Z literatury a již dříve provedených experimentů byla vyhodnocena optimální velikost pórů a tloušťka stěn struktury. Dále jsou diskutovány vhodné materiály pro výrobu a také úskalí výroby metodou 3D tisku, která vznikají při tištění tenkých stěn a úzkých trámců. Pro účely mechanických zkoušek bylo vyrobeno několik variant trabekulárních a gyroidních struktur a jejich následně zjištěné mechanické vlastnosti byly přeneseny do konečněprvkového modelu lidské mandibuly anonymního pacienta s gyroidním, dentálním implantátem. Simulace dokazují, že tělesa implantátů s nižšími moduly pružnosti zlepšují rozdělení napětí v kosti a zmenšují lokální extrémy napětí. Dalším závěrem práce je optimální globální modul pružnosti struktury, který by měl být v rozmezí ca. tři až deset GPa.

Klíčová slova: gyroid, porézní, dentální, implantát, napěťový štít, QCT/FEA.

Contents

List of Abbreviations

AM	Additive Manufacturing
BCC	Body-Centered Cubic
BCs	Boundary Conditions
BEC	Basic Element Cell
BIC	Bone-Implant Contact
BII	Bone-Implant Interface
CAD	Computer-Aided Design
cp-Ti	Commercially Pure Titanium
CT	Computed Tomography
DICOM	Digital Imaging and Communications in Medicine
DLP	Digital Light Processing
EBM	Electron Beam Melting
ELI	Extra Low Interstitial
FDM	Fused Deposition Modeling
FEA	Finite Element Analysis
FEM	Finite Element Method
HCP	Hexagonal Close-Packed
HU	Hounsfield Unit Scale
MJF	Multi Jet Fusion
MoE	Molybdenum Equivalency Index
MPI	Message Passing Interface
PBF	Powder Bed Fusion
QCT/FEA	Quantitative Computed Tomography-based Finite Element Analysis
RCCM	Research Center of Computational Mechanics
ROI	Range of Interest
SLA	Stereolithography (printing process)
SLM	Selective Laser Melting
SLS	Selective Laser Sintering
STL	Stereolithography (file extension)
TPMS	Triply-Periodic Minimal Surface
TSA	Total Shoulder Arthroplasty

1 Introduction

The goal of this dissertation is to present a novel, porous surface of dental and orthopedic implants in the form of a sheet-based gyroid structure with defined pore sizes that creates a mechanical interlock between metal and bone to improve both primary and secondary stability and create a smooth transition of mechanical properties to diminish the adverse effects of stress shielding.

The success rate of conventional, homogeneous dental implants is over 90% as of 2021 [1]. Retrospective studies show that most implant failures occur during the early stages of implantation (about 6.7% of all dental implants fail during the early stages) [2]. To prevent the early loss of stability without the presence of infection (aseptic loosening), geometrical modifications of the intraosseous parts of implants, e.g. porous tantalum (Ta) [3] are introduced in order to make the conditions better for osseointegration. These geometrical modifications usually aim to reduce the overall stiffness of the implant to prevent stress shielding (described in Chapter 2.4. The first titanium (Ti) dental implants were designed by Per-Ingvar Brånemark and their numerous variants are still widely used with satisfactory results. However, these implants are quickly becoming obsolete as they can no longer meet the patients' demand for rapid healing and quick osseointegration [4]. Other retrospective studies present multivariate analyses that show a significant association between the failure of the implant and a bad mechanical coupling and short implants [5].

To counteract these shortcomings, a porous layer on an implant has the potential to create an interface with a gradient of material properties, thus reducing the effects of stress shielding on surrounding bone and creating a hybrid bone-metal biomaterial with an interconnected system of metal pores filled with ingrown bone tissue [6]. A comparison between a conventional, homogeneous dental implant and one with a porous surface is shown in Figure 1. This thesis describes a novel gyroid structure that can be used as a load-bearing part of any implant (e.g. femoral and acetabular components, dental implants and others). A sample sheet gyroid structure is illustrated in Figure 2.

Porosity and bone ingrowth are phenomena positively influencing osseointegration of metal implants and were described in detail by many reputable works [7–10]. As in vivo research on animal models shows ([6]—my previous work and [11]), newly formed bone beams after implantation are (with good implant topology) able to grow inside the body of the implant and create a bone-metal composite material with a continuous change in the values of Young's Modulus (E). This continuous transition of mechanical properties and bone ingrowth are the main motivating factors for the design of porous structures in implants as they prevent rapid material change and mitigate the effects of stress shielding [12].

Figure 1: Comparison between the geometry of a conventional, homogeneous threaded dental implant (left, [13]), a push-in homogeneous implant (center, [14]) and a sample dental implant with a porous, gyroid surface (right).

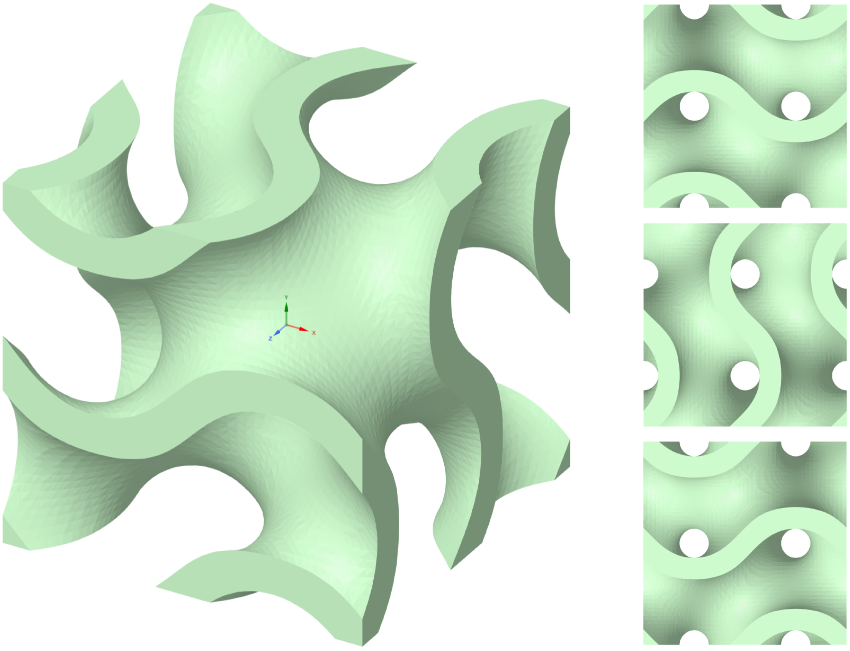

Figure 2: Basic element cell (BEC) of a sheet gyroid structure that will be discussed. On the left is the structure's trimetric view, images on the right are the structure's side views.

Structural porosity aims to substitute traditional surface treatments that modify surface topography, surface energy and resulting contact angle and wettability, osseointegration and cell proliferation [15]. The historical approach using traditional machining methods is to manufacture a homogeneous implant and create a porous outer layer by various treatments. The surface treatment increases the surface area or carries a healing agent.

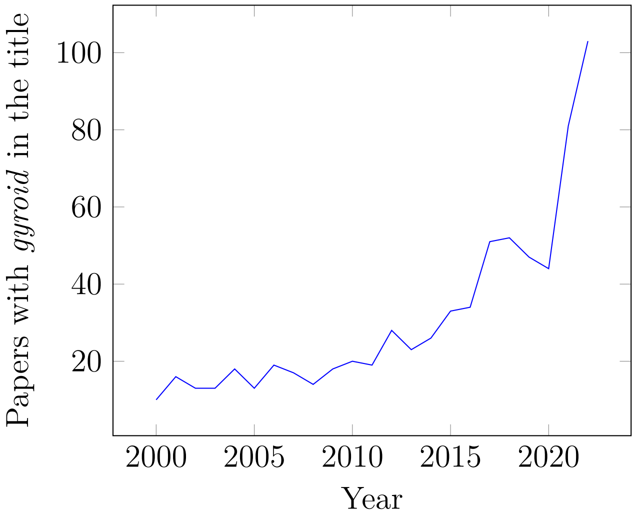

Figure 3: Popularity of the word *gyroid* in titles of scientific literature over the past 23 years, beginning in 2000. Research was performed in databases of Google Scholar.

Surface treatment is usually performed by the following methods:

- Sandblasting
- Acid-etching
- Laser ablation
- Anodic oxidation
- Plasma spraying and ion deposition

Introducing porosity on a structural level (as opposed to traditional surface treatment) is a less conventional process that makes the implant production easier to modify on the go and also makes it easier to produce custom-tailored products by making it a one-stage process that can be modified for individual products, unlike a well-optimized bulk production process for a single product. However, 3D printing is not the definitive go-to option for all applications and still carries a degree of uncertainty in terms of production quality as demonstrated on specimens in Chapters 7 and 8. Furthermore, some 3D-printed parts may still require machining (a good example is the internal thread of a dental implant's stem). Optimal pore sizes and topography are investigated in Chapter 2.2. The technology predominantly used to produce porous metal structures is 3D printing (specifically selective laser sintering—SLS, or selective laser melting—SLM, discussed in Chapter 3).

The porous geometry of the gyroid structure is well-suited for additive manufacturing (AM). Conventional machining does not lend itself to creating porous structures (inside porosity cannot be achieved by machining). The rising popularity of these topics (and the contemporary relevance of this thesis) in scientific literature is shown on a graph in Figure 3.

2 Osseointegration

When discussing orthopedic and dental implants, we should make the distinction between their biological aspects, biocompatibility, osseointegration and their mechanical and material properties. Considering these subjects are closely connected, it is brought to the reader's attention that they are discussed individually. However, the topics intertwine and will often refer to each other.

2.1 Porous and Homogeneous Structures

Porous surfaces and structures provide greater surface area and assure an interlocking mechanism from early stages after implantation. Existing in vivo research has shown that porous structures have benefits in regard to density of osteocytes at the bone-implant interface (BII) [16]. 3D-printed porous scaffolds with interconnected pores should allow the formation of vascularized tissue, which is required to supply nutrients and oxygen to growing cells inside the pores [17]. Another benefit of porous structures is a reduced elastic modulus E resulting in a reduction of the stress shielding effect ([6], described in Chapter 2.4). Porous trabecular structures made of tantalum have been used in implantology for several years [17, 18]. Therefore, porous structures seem to have benefits in regard to osseointegration. Moreover, applying a TiO_2 porous layer on the outer layer of a homogenous implant can potentially lead to wear debris, particle deposition and subsequent necrosis, therefore negatively impacting osseointegration [19].

However, the geometry of the porous surface affects the quality of the final product in terms of manufacturing. The method of manufacturing is an important factor. My recent research (TAČR project no. TJ01000328) revealed that 3D printed trabecular systems are unreliable and are prone to beam splitting and discontinuities in individual beams, which they comprise of. These production inhomogeneities can lead to wear debris and subsequent necrosis [20]. Moreover, since they have primarily sharp edges, only ligament tissue forms in their vicinity, preventing actual bone growth. These shortcomings can be eliminated by using wall-based structures with a system of interconnected pores. One such structure is the gyroid, which is described by the combination of the sine and cosine functions and represents a wall system. The gyroid (as well as trabecular structures) belongs to the category of 3D scaffolds with interconnected communicating pores. With wall systems, it is presumed that the splitting, chipping and discontinuities of beams of the individual trabeculae is eliminated by the nature of the wall structure. Compared to trabecular structures, gyroid scaffolds are more reliable and have higher strength while still retaining low elastic moduli similar to human cancellous bone [21]. The geometrical parameters of the gyroid influence its mechanical resistance [22]. At present time, gyroid structures are the subject of many research projects in the field of biocomposites and biomimetic materials. However, they are not being developed for the purpose of load-bearing implants. Some research has been made about non-gradient gyroid structures comparing pore shapes and sizes [23]. However, these findings have yet to be applied in developments of a load-bearing structural member. The porosity and elastic properties could potentially allow for manufacture of an implant without a designated homogeneous core, thus making the whole load-bearing part porous. A solution using a porous outer layer with the gyroid structure has the potential to provide better primary short- and secondary long-term stability by allowing the bone to grow inside the implant itself and provide sufficient permeability for proliferation of bone cells [24]. I have already participated in a research showing that bone cells can grow inside a porous structure, a fact that was verified by an in vivo experiment on a laboratory pig model [6].

2.2 Porosity and Pore Sizes

Optimal porosity of open-structure implants has already been investigated in the early 1980s [25]. The authors found that optimal pore sizes for fixation strength are in the range of 50–400 µm in implants with a porous outer layer. However, this study offered only examples of structures made of sintered metal powder with a wide spread of pore sizes. In a later study [26], authors performed in vitro tests on titanium implants with drilled cylindrical channels of various (300–1000 µm) diameters. The fastest migration of cells was achieved in channels with a diameter of 600 µm, and the slowest was in 1000 µm channels. Mineralization and differentiation of tissue were also most observable in channels with diameters in the 400–600 µm range, despite 300 µm channels having the highest density of cells. The authors attributed the success of the optimal range of 400–600 µm to not having a cellular density too high as to inhibit the distribution of oxygen and nutrients, agents which are needed for cellular differentiation.

Many studies were also performed on animal models both in vivo and in vitro. Authors Van Bael et al. [27] performed in vitro tests of 6 porous structures with three different pore shapes (triangle, square and hexagon) and two sizes (500 and 1000 µm). One day following colonization, a greater number of cells was observed at the 500 µm pore size, an observation which reversed after 14 days in favor of the 1000 µm pore size. Pore shape did not have any significant effect on cell proliferation. These results have been later corroborated by another group of researchers with nearly identical model parameters [28]. Another study [29] presented research on porous Ti structures that concluded the optimal pore size to be 400 µm and also stated that pore smoothness and roundness positively affect the overall reliability of the structure and its mechanical properties[1]. Another research [9] also stated the optimal pore size for fixation strength and osseointegration to be 600 µm, corroborating the optimal range of 400–600 µm.

The human trabecular bone has about 70–90% porosity [30]; therefore, one might conclude that the optimal range of the overall implant porosity should be the same. However, this range only considers the biological requirements. If we weigh in the mechanical requirements, too, we get a range that is relatively lower. This can be observed from the equation proposed by Liu [31] that describes the relation between the tensile strength and porosity of a porous material in uniaxial tension:

$$\sigma = K(1-\theta)^n \sigma_0 \tag{1}$$

where σ and σ_0 are the tensile strength of the porous material and its corresponding compact equivalent material, respectively, θ is the overall porosity, K is a material constant dependent on material type and manufacturing process, and n is the plastic brittle index that varies in the range of 1.0–1.5 for metals (1.0 for metals with good ductility like tin (Sn) and copper (Cu) and 1.5 for metals with poor ductility, like titanium [32]). We can see the relationship between porosity and strength for different values of n in Figure 4.

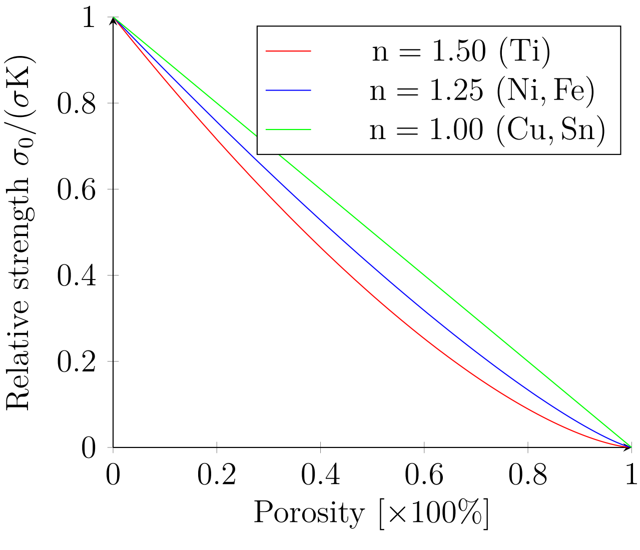

Figure 4: Graphical representation of Equation (1) provided by [31] for different values of the exponent n that represents plasticity of materials.

The relation between relative strength and porosity presented in Figure 4 shows that if one were to abide by the biological requirements on porosity (70–90%), the strength of the structure would drop to ca. 10–20%, as most implants are made from Ti or its alloys.

---

[1] The research was performed on porous Ti non-gyroid structures, but the gyroid also benefits from round shapes as it is a combination of the sine and cosine functions

Schwarz [33] performed an extensive study to compare different variants of channel-like porous titanium. He found the optimal parameters to be 400 µm pore size and 40% overall porosity for osseointegration in combination with static strength. Vasconcellos [30] corroborated this research by stating that the optimal overall porosity for osseointegration is in the range of 20–50%. Another study confirming this result can be found in [34]. The overall consensus on the optimal pore size and the overall porosity among researchers was utilized for the gyroid structure's design. However, as explained in Chapter 8.2, we can afford to increase the porosity with a sheet-based gyroid structure.

For reference, authors [35] calculated the porosity of the human mandibular condyle using micro CT (Computed Tomography) from an experiment. Their results are added along with the results of other authors [36–40] for other parts of the human body in Table 1.

Table 1: Porosities of various trabecular and cortical human bones. Values obtained by micro CT. Authors [35–40].

	Mandib. condyle	Femoral shaft	Femoral neck	General value
Trabecular porosity [%]	79.3	N/A	N/A	>50
Cortical porosity [%]	3.5	>5	>10	N/A

2.3 Biocompatibility

2.3.1 Basic Principles

Every foreign body that is placed inside a living organism has to be biocompatible to minimize the probablility of an adverse reaction. Titanium and its alloys, such as Ti-6Al-4V, are considered biocompatible as they have low electric current conductivity that enables a formation of a thin TiO_2 layer [41]. This passive, corrosion-resistant oxide layer is preserved in the pH of the human body as the isoelectric point of Ti-6Al-4V is ca. 5–6 [42]. These values enable an almost risk-free placement of the alloy inside the human body in the form of an implant. This fact proves to be advantageous in the aggressive environment of the human body. However, it is no guarantee that significant amounts of Ti, Al or V will not be released into the body as the Ti-6Al-4V alloy is known to be prone to mechanical abrasion [43]. The alloy is mostly used for orthopedic implants, bone prosthetics, joint replacements, fixation screws and joint heads. Notably, pure cp-Ti (Commercially Pure Titanium) has even better corrosion resistance than Ti-6Al-4V and is, therefore, considered the most widely used material solution with the best biocompatibility in implantology [42].

Biocompatibility can be further facilitated by applying a surface treatment. Generally, it is recognized that rough-surface implants have excellent bone-implant contact (BIC). Therefore, choosing a means of manufacturing, such as 3D printing, that produces rough surfaces by definition, is viable. Other means of producing surface roughness are laser ablation, plasma Ti coating, plasma etching, ceramic particle abrasion, anodization or acid-etching. Surface treatment is not important for this particular 3D printing application and, therefore, not an integral part of this thesis.

2.3.2 Biocompatibility Experiments

To measure biocompatibility, we can use a test of bone cell proliferation on specimens made from different metals. This approach was used by Matsuno et al. [44], who made a comparative study of individual elements in regard to proliferation of bone cells and percentage of bone in contact with the implant. The highest amount of newly-formed bone after a measured period of time was observed in niobium (Nb), then tantalum (Ta) and subsequently titanium. Furthermore, they observed the greatest BIC after four weeks in Ti and Ta. Eisenbarth et al. [45] found that Ti is very biocompatible, but Ta and Nb offer even better biocompatibility. These results confirmed the conclusions by Matsuno.

From this, we can infer that Ti, Nb and Ta have the best biocompatibility of all metal elements. Despite the Ti-6Al-4V alloy still being dominant (it is sometimes called the *workhorse alloy*), new alternatives, such as the β Ti alloys Ti-35Nb-6Ta or Ti-30Nb-17Ta, and many others, are emerging. I attribute the success of the Ti-6Al-4V alloy to wide availability, inexpensiveness and good standardization.

However, cp-Ti and Ti-6Al-4V also have their disadvantages. Vanadium (V) is reportedly cytotoxic [46], and patients often show signs of neurological damage caused by aluminum (Al) [47]. Both the element and the alloy also have low abrasion resistance. Hence, debris from implants can be deposited inside the patient's body. Decades ago, a research was published that discussed the cytocompatibility of Ti-6Al-4V on an animal model and found that due to abrasion, particles of the material are being deposited into the animals' bodies [48, 49]. The authors reported increased levels of Ti and V in lung tissue and increased levels of Al in muscle and lung tissue and lymph nodes. A large concentration of Ti was also reported in bone at the peri-implant area. Authors [50] also found that Ti is not soluble in physiological environment and was not found in the animals' urine. However, the authors found that Al and V are soluble and were found in the urine.

2.4 Stress Shielding

In terms of biocompatibility, one of the biggest concerns is the global modulus of the implant. As the values of modulus of cp-Ti and the Ti-6Al-4V alloy (Table 4) are ca. 4–6× higher than those of human bone (ca. 17.1 ± 3.5 GPa according to [51], but vary among different people based on age, sex, exercise and other factors), the bone around the implant often suffers from an adverse effect called stress shielding. Since implant moduli are higher than bone moduli, most loads are transferred into the implant, leaving the bone unloaded. In the absence of load, the bone begins to lose its mass at the peri-implant area and starts to degrade [52]. This degradation is caused by a lack of mechanical stimuli. This unwanted effect incentivizes the development of β Ti alloys as they offer lower elastic moduli—see Chapter 4.4. Bone subsequently atrophies and loses its density [53]. To mitigate this effect, we can consider two solutions:

1. Reduction of the *material* modulus
2. Introducing porosity, which in turn lowers the *global* modulus of the whole implant

As Table 4 suggests, there are materials (namely the β Ti alloys) that can reduce the values of modulus to 71 GPa or lower, based on alloying elements. Modifying alloys this way is a good but costly solution to lower the material modulus.

The proposed solution in this thesis is based on a porous structure that reduces the *global* modulus of the entire implant or its surface, depending on the design. As already mentioned above, porosity can reduce the global modulus by one order of magnitude, as demonstrated in a modified table from one of my previous research works (Table 2, [54]). This reduction of modulus is beneficial for approaching the moduli of human bone. Some radiographs showing the effects of stress shielding are shown in Figures 5 and 6. One of the most cited research papers on this topic by D.R. Sumner and J.O. Galante [55] is a study done in 1992 where the authors point out the importance of the shape and material properties of implants based on an in vivo canine model. Especially the stiffness at the BII plays a vital role as comparison between a stiff and a porous-coated implant revealed that unwanted local bone atrophy occurred with the former, but beneficial bone hypertrophy occurred with the latter. The cobalt-chromium (Co-Cr) implant with the highest E had the worst results.

Research points out that stress shielding is a significant contributor towards long-term bone remodeling and plays an important role in bone atrophy and bone hypertrophy. Figure 5, which is provided by another impactful work by J. Nagels et al. [56] shows the effects of stress shielding on a humeral implant. These authors also presented that patients who are affected by osteoporosis are at a greater risk of stress-shielding-induced bone loss. The authors also found that stress shielding occurs significantly more often for patients with long humeral stems than for patients with short ones. I deduce this could also be true for other elongated implants (e.g. femoral stems, dental implants), where (as J. Nagels et al. also state) bending of long stems causes unwanted stress on proximal bone areas (closer to the point of attachment). In contrast, a shorter stem transfers the load more proportionately. For example, we can see this trend in dental and femoral components, where the market share of short implants is increasing.

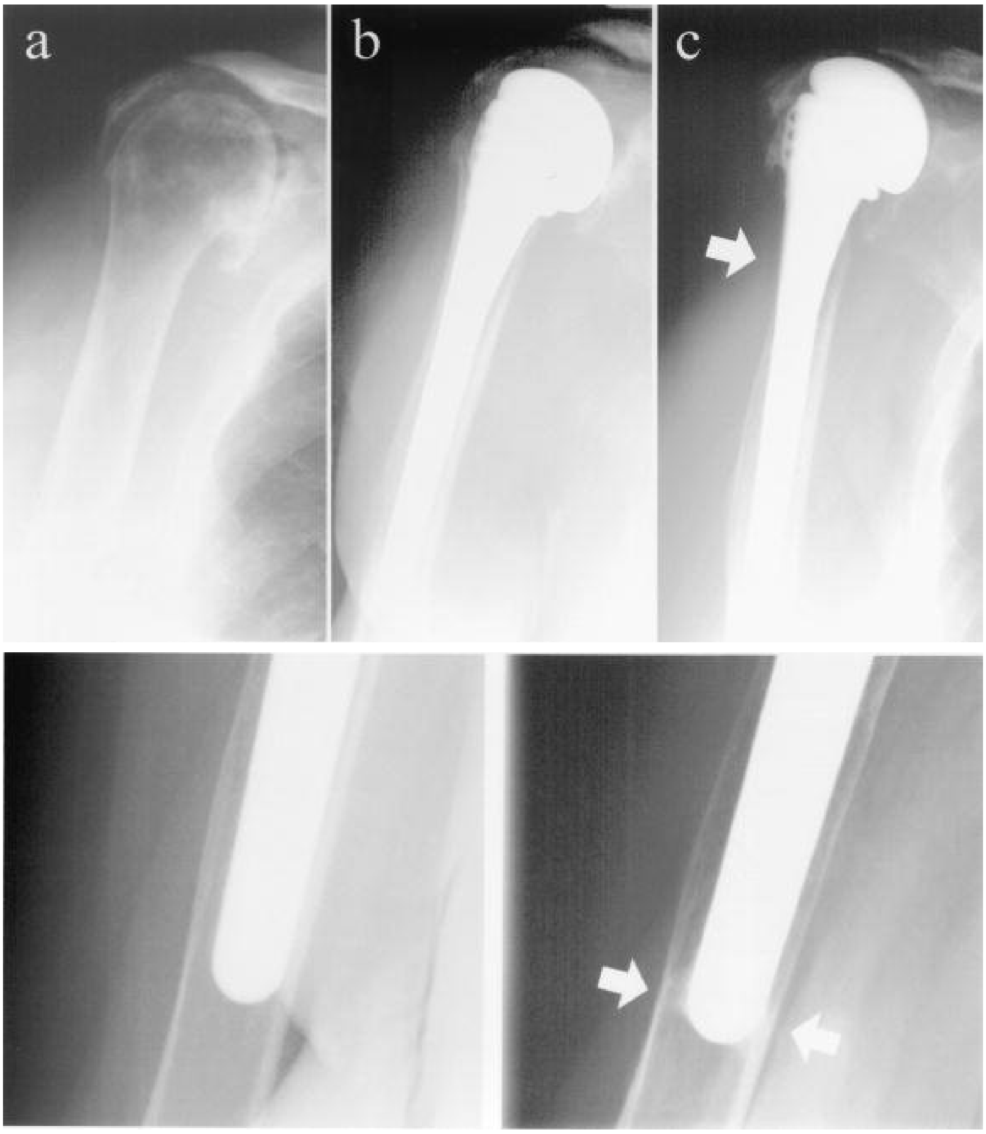

Figure 5: Images showing the effects of stress shielding on a humeral implant of two different patients who undertook total shoulder arthroplasty (TSA). Top row: a) Preoperative image, b) Postoperative image, c) Image after 7 years. Arrow shows bone atrophy of the cortical bone around the implant as a result of stress shielding. Bottom row: two images illustrating the effects of stress shielding around the apical area of a humeral implant. Left—postoperative image, right—image after 6 years. Stress shielding can be observed around the arrows. Authors of the images are J. Nagels et al. [56].

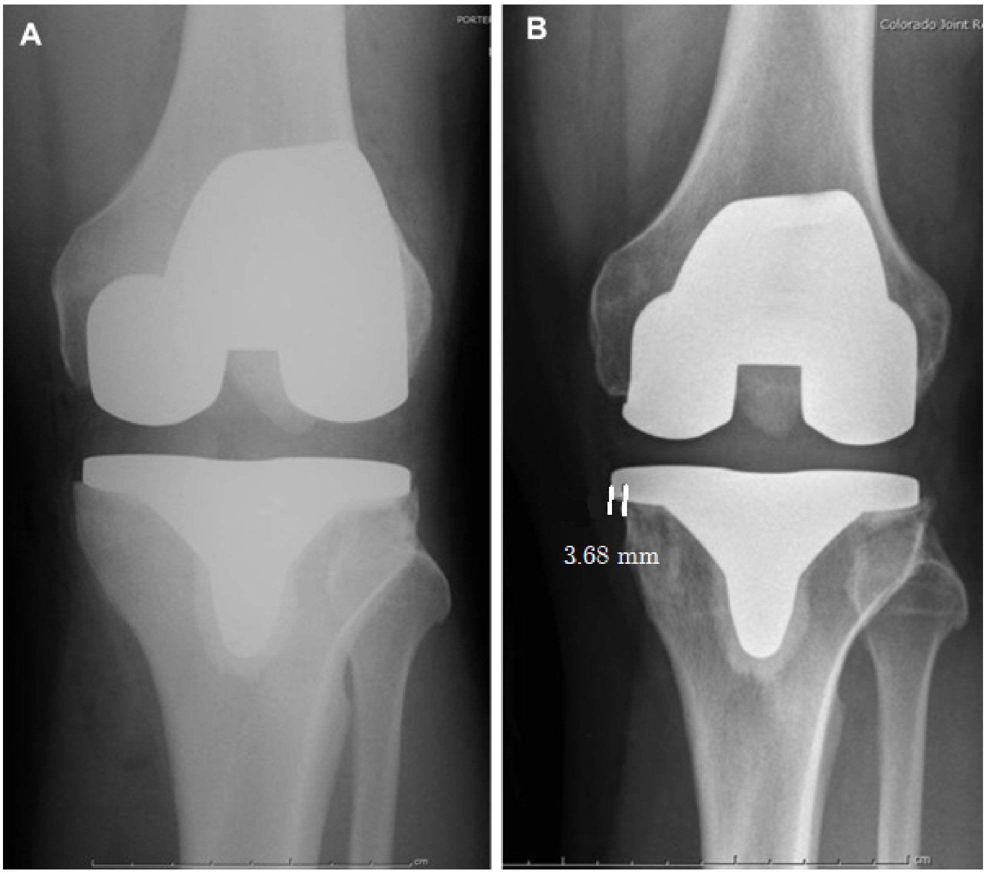

Figure 6: A radiograph showing the magnitude of the stress shielding effect with a direct comparison between the immediate, postoperative image (left) that shows no bone loss and the two-year postoperative knee radiograph (right) showing almost 4 mm medial tibial bone loss [57].

Table 2: Values of E calculated based on finite element method (FEM) simulations of gyroid structures (my previous research [54]). Note that pore sizes do not necessarily indicate a dramatic evolution of E in this case—it is governed by porosity instead.

Material or structure	Young's Modulus E [GPa]
Gyroid pore size 400 µm	14.57
Gyroid pore size 450 µm	12.98
Gyroid pore size 700 µm	12.20
Gyroid pore size 850 µm	11.10
Base Ti-6Al-4V material	120.00

3 Metal 3D Printing

This chapter includes basic comparisons between traditional machining technology and AM technologies, mainly 3D printing relevant for manufacture of implants—selective laser sintering (SLS), selective laser melting (SLM) and electron beam melting (EBM), all powder bed fusion technologies (PBF). Other 3D printing technologies, such as fused deposition modeling (FDM), stereolithography (SLA), digital light processing (DLP), multi jet fusion (MJF) and other technologies will not be discussed as they cannot be effectively used for manufacturing metal intraosseous parts of implants and their discussion would, therefore, be redundant for this work (they mostly work with polymers).

All three PBF technologies have one thing in common—they use a protective atmosphere to shield the solidifying parts from oxidation and other sources of contamination. As will be discussed, this process creates (among many benefits) a notable inconvenience as filling the chamber with protective gasses (argon, helium) and creating a vacuum is expensive and, therefore, unprofitable for small batches of products.

The standard workflow for PBF technologies is similar for SLS, SLM and EBM and is described in the following diagram:

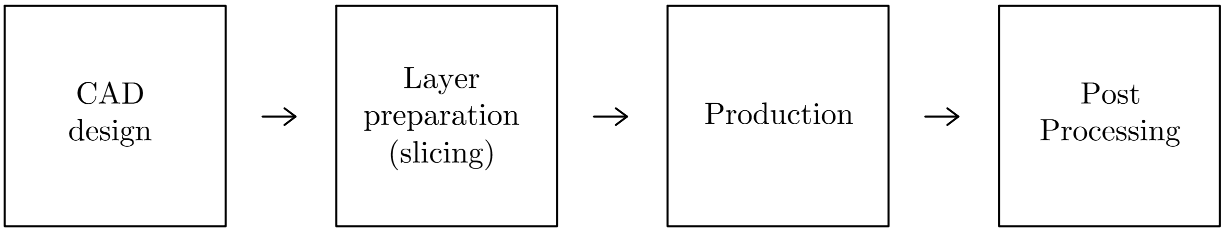

Figure 7: Brief illustration of PBF technologies' workflow.

3.1 Selective Laser Sintering

SLS is an AM method that is long in development and is currently being used in many engineering applications where machining falls short on geometrical demands and where companies want to deliver repeatable, customized and high-quality powdered parts for various applications, including automotive, aerospace and medical industries [58]. This AM process employs a high-powered laser that scans the machine's bed layer by layer. The high-powered laser is delivered through a set of mirrors to fuse the materials' particles precisely (not fully melting them) at about 85% of their melting point [59] and achieving a bond on a molecular level, rather than fully melting the powder (like SLM does). However, SLS is still considered a limited-precision technology as its precision threshold is directly bound to the size of the largest grain of the metal powder being used.

This process creates a product with a controllable porosity level as the material is not fully melted but fused instead. One of the main advantages of this technology is the ability to work with materials comprising of different elements as the machine does not require a set melting point for one individual element. For example, the SLS technology is widely used to print from the Ti-6Al-4V powder.

SLS can sometimes be used without post-processing (some biomedical applications, prototypes) but usually requires infiltration, polishing or other post-processing to be usable for load-bearing or mechanical applications [60].

3.2 Selective Laser Melting

SLM is the other of the two PBF technologies. Compared to SLS, it fully melts the powder in each layer, making a much less porous product. Since local melt pools are created, products with density $> 99\%$ can be achieved [61]. Therefore, SLM products have much better mechanical properties than SLS products [62]. However, the use of SLM also brings requirements on materials—one can only use a metal element, or an alloy, with the same melting point, as the intensity of the laser has to be set to that number. Therefore, using alloys with elements with different melting points (we can invoke the standard Ti-6Al-4V alloy) is not possible. The most common materials used for SLM are, e.g. the 316L stainless steel, pure aluminum or pure titanium in powder form.

3.3 Electron Beam Melting

Electron beam melting (EBM) is yet another AM process that utilizes a protective chamber and metal powder, but uses an electron beam instead of a focused laser. Similarly to SLS and SLM, an electron emitter scans the bed and sends electrons to pre-defined locations where heat is produced, and metal powder is solidified. When Ti alloys are used, EBM can produce higher-density parts than SLM and is reported to have superior quality [63].

During the printing process, a vacuum is created in the protective chamber (ca. 10^{-4} to 10^{-5} mbar), which helps Al and Ti alloys by shielding them from oxygen and nitrogen. Then, a small amount of a helium gas bleed in a controlled vacuum of ca. 10^{-3} mbar is delivered into the chamber to prevent the build up of smoke [64]. Finally, the protective chamber is flooded with helium and the parts cool down for several hours.

Without proper heat treatment, EBM-created parts from the conventional Ti-6Al-4V alloy are usually brittle and hard as they mainly have α' martensitic structure and small amounts of β phase compared with bulk material [63]. Still, even with proper processing and heat treatment, some defects inevitably arise and usually produce crack initiation sites near them. These defects mainly manifest during fatigue tests, as EBM parts still show large scattering in high cycle fatigue despite its efficacy in producing high-density products [65].

Based on the powder that is used, various parameters have to be defined, such as scanning speed, electron beam spot size, size of the melt pool, input voltage and others. Therefore, using EBM machines requires skilled personnel and improper machine control may result in bad microstructure of the product [63].

3.4 Benefits of Metal 3D Printing

As the parts produced by AM methods do not require machining and, therefore, do not suffer a material loss, one of the great benefits of both SLS and SLM is financial savings. The estimate for these savings is ca. 50% [66] and also includes further costs associated with machining. For companies, the ratio of bought to used material can be reduced from ca. 40 : 1 to approximately 1 : 1 [67]. However, the purchase costs of SLS and SLM machines and powder price are higher.

In the field of implants, where patient-specific custom solutions are often required, there is particular demand [68] for 3D-printed custom implants (both polymer and metal products) as customization is easy and can be done in a short amount of time. Mass customization is the main envisioned benefit as more and more technologies emerge that can utilize patient-specific CT-scan data to create a custom implant or a prosthetic. Authors [69] state that the most significant benefit of mass customization with 3D printing is eliminating the need for re-calibration of assembly lines, moulding etc., while still satisfying the market demand by maintaining cost-effective mass production.

One of the main advantages of metal SLS and SLM printing is its superior precision and high quality of printing (the lower resolution limit of PBF—SLS and SLM technologies—is ca. in the dozens of µm [69], depending on the machine). It is, however, essential to remember that when the user approaches the lower resolution limit, discontinuities and defects might occur (more on this in Chapter 7). It is also worth noting that regardless of the precision of the laser, one cannot ever achieve resolutions finer than what the base powder material allows for (the largest grain size), especially in SLS, where particles are only sintered and largely retain their original shape.

3.5 Challenges of Metal 3D Printing

As SLS products are porous by nature, shrinkage might occur during the post-processing stage while oven heating [70]. According to Balc et al. [70] and also my personal experience from observing fatigue testing, SLS products are also less durable than their machined counterparts and are more fragile. SLS and SLM products are often put through a series of post-processing treatments to counteract these shortcomings. These may include heat treatment, polishing, painting or furnace infiltration [71]. However, the central potentials of 3D printing—the ”print on demand” and its simple production process—are greatly diminished with each added production step [58]. Other defects may also occur and include uneven layers, improperly fused particles, formation of cracks or reaching the accuracy limit of the machine [72].

Formation of a non-reactive oxide layer, which is typical for SLS and SLM, also inhibits metallurgical bonding between individual layers during the process of 3D printing [58]. This layer then causes spheroidization of the powder because of contamination by oxygen [73]. This contamination can be either in the form of an oxide, trapped gas in the powder bed of the machine or impurities within the powder [74]. Usually, spheroidization occurs due to the strain-induced grain boundary migration [75] (the movement of the boundary between adjacent grains of a material).

3.6 Powder Production

In order to properly use the aforementioned PBF production methods, a special powdered material has to be used so that the scanning laser or electron beam can precisely fuse the material in the required places and nowhere else. This can be (to some level) achieved by using a powder that is fine enough so that its maximum grain size does not exceed the required precision of the product (usually, thin walls and sections can be a problem).

The quality of the input powder is also essential, as improper particle size or distribution can cause uneven layer heights, improper particle flow and poor packing density [76]. By nature, the particle size cannot be greater than the layer height [77]. Even distribution of powder on the base plate, which depends on powder quality, is also important for a good quality product [78]. Bad distribution of particle size can happen during the production of the powder. Today, we recognize multiple atomization processes [76, 79]:

1. Gas atomization (air and inert gas atomization, vacuum inert gas atomization, electrode induction gas atomization, water and ultra-high pressure water atom.)
2. Plasma atomization
3. Plasma rotating electrode

With the gas atomization process, producing a fine enough powder requires using a medium that breaks the liquid, molten metal into a spray that freezes into a powder [79]. Whether it is a method based on air, gas or water, it includes a high-velocity medium to cool down the molten metal after being pushed through a (usually ceramic) nozzle to break apart or ”atomize” into a fine metal powder.

The latter two approaches produce a higher quality powder with fewer irregularities and better spheroidicity [76]. To achieve the best possible results, the authors also recommend using powders with few surface irregularities (satellites), low internal porosity, high purity and tight distribution of particles. Poorly solidified products can contain unwanted pores and residual stresses. These can promote the creation of cracks and delamination between individual layers [80]. Pores, spheroidization and rough surfaces are amongst the most common defects of products made by SLM [81].

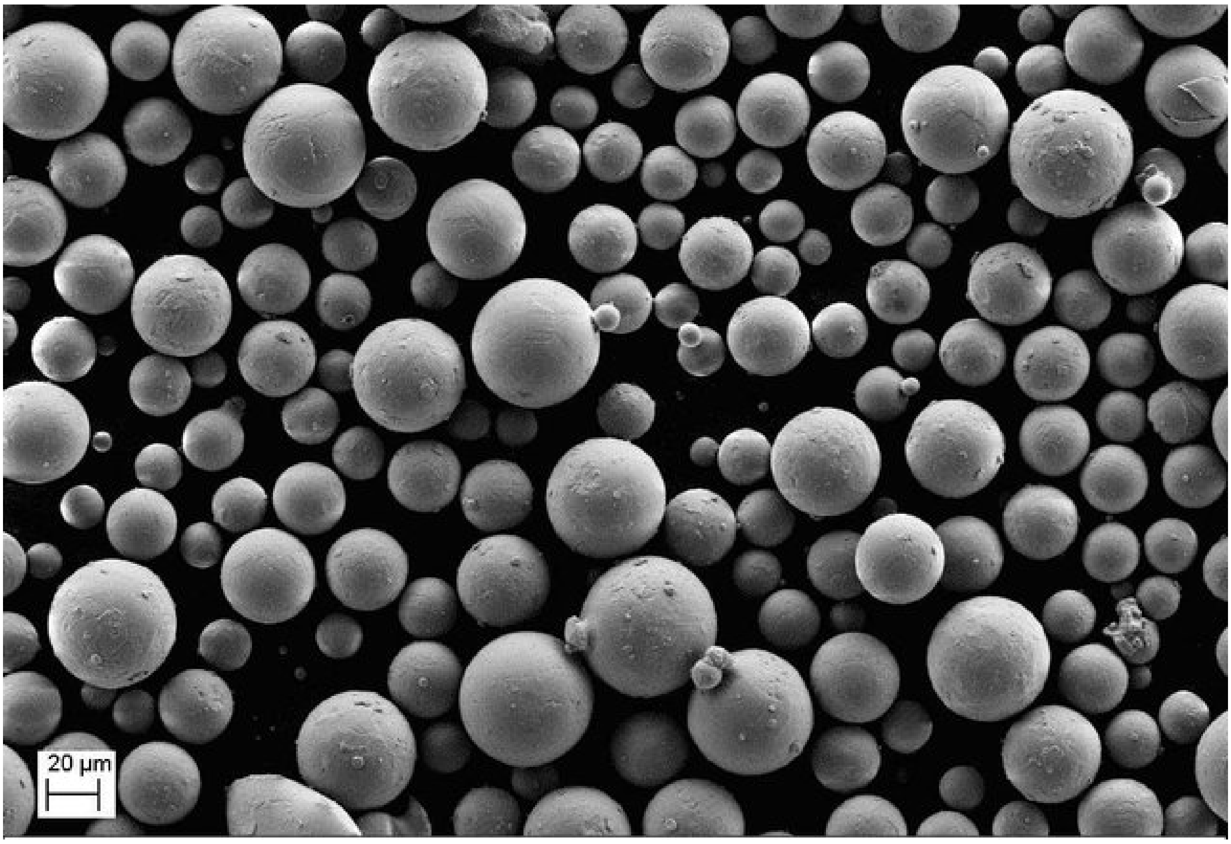

Figure 8: Ti-6Al-4V powder irregularities. The picture shows good spheroidicity, but the particle size distribution is uneven, and powder has a lot of balling—unwanted connections of individual spheres [82].

Depending on the intended use of the final product, it is also recommended to perform surface treatments for SLM-made parts to remove particle debris, reduce surface spheroidization and achieve an even surface (sandblasting, acid-etching, chemical mechanical polishing and others [81]). The inclusion of this process would be identified as a difficulty in other industries. However, for the purpose of osseointegration, it is near-beneficial to have an uneven surface composition (greater surface area generally means better conditions for bone ingrowth and ongrowth).

4 Materials

The material that is predominantly used in implantology is titanium and its alloys. This chapter will guide the reader through the most common Ti-based materials and their allotropic modifications, which are viable for application in manufacturing of implants.

Before we explore the individual materials and their specifics, let us lay out a basic overview of conventional materials' most commonly measured mechanical properties. We are especially interested in their elastic modulus—usually, the lower, the better—and yield strength, as it dictates the point at which the material becomes unusable for medical purposes. However, ductility, defined either as percentage elongation or the difference between the yield and ultimate strength, is also beneficial.

Table 3: Basic mechanical properties of materials most commonly used for orthopedic and dental implants [83].

Material	Microstructure	Modulus [GPa]	Yield Strength [MPa]	Ult. Tens. Strength [MPa]
Stainless Steel		200	170–750	465–950
Co-Cr-Mo alloy		200–230	275–1585	600–1795
cp-Ti	α	105	692	785
Ti-6Al-4V	α+β	110	850–900	960–970
Ti-6Al-7Nb	α+β	105	921	1024
Ti-5Al-2.5Fe	α+β	110	914	1033
Ti-12Mo-6Zr-2Fe	Metastable β	74–85	1000–1060	1060–1100
Ti-15Mo-5Zr-3Al	Metastable β	75	870–968	882–975
	Aged β+α	88–113	1087–1284	1099–1312
Ti-15Mo-2.8Nb-3Al	Metastable β	82	771	812
	Aged β+α	100	1215	1310
Ti-13Nb-13Zr	α'+β	79	900	1030
Ti-15Mo-3Nb-0.3O	Metastable β	82	1020	1020
Ti-35Nb-7Zr-5Ta	Metastable β	55	530	590
Ti-35Nb-7Zr-5Ta-0.4O	Metastable β	66	976	1010

4.1 Phases of Ti alloys and their stabilizing elements

Regarding the structure of titanium as an allotropic element, we can distinguish between three types of Ti alloys:

1. α Ti alloys
2. α+β Ti alloys
3. β Ti alloys

The standardized cp-Ti grades have the α structure, the most common and widely used Ti-6Al-4V alloy is α+β and the β Ti alloys are considered more of an alternative material option in implantology (based on my market research shown in Chapter 5).

However, β Ti alloys have significant advantages compared to the α+β alloys—lower moduli, superior corrosion resistance and higher strength [84]. Their disadvantage is an exceptionally high cost of manufacturing. Therefore, their use is limited to special applications, such as high-performance components of industrial machines, crankshafts of racecars and custom-made implants.

Titanium is an allotropic material; therefore it can exist in multiple configurations of the crystal lattice. The α phase has a hexagonal close-packed (HCP) crystal structure, as opposed to the β phase, which has a center-oriented structure (body-centered cubic—BCC), as shown in Figure 9. To stabilize the desired Ti phase, we can use alloying elements to achieve different properties of the final alloy. The choice of alloying elements is connected with the ability of individual elements to stabilize either Ti phase.

Elements that reduce the α/β transus temperature (ca. 882 °C) and stabilize the high-temperature β phase can be divided into two groups—the β-isomorphous and β-eutectoid [85]. Elements that form the β-isomorphous structure (binary Ti alloys) are V, Mo, Nb, Ta, W, Re and others. A binary alloy only consists of 2 metals, e.g. Ti-Ta or Ti-Mn. Elements that form the β-eutectoid structure are Cr, Fe, Mn, Cu, Ni, Co, H, Ag, Au, Pb and others.

Another Ti phase is the ω phase. It is a metastable phase that forms in Ti alloys with elements that stabilize the β phase of the alloy, mainly during hardening from high temperatures (β phase region) or during solution annealing. This phase gives the alloy strength but increases its brittleness. By adding elements like Al (an α stabilizer), Zr or Sn (neutral, but acting like α stabilizers along with other α stabilizers), we can suppress the formation of the ω phase and facilitate formation of the α phase of the alloy [86].

The last group of metals in regard to stabilization are neutral metals. These metals are not primarily used as stabilizers of individual Ti phases but for other reasons, such as strengthening of the alloy. Elements Zr, Sn, Si and Hf fall into this category [86].

4.2 Pure Titanium

Historically, there were many materials orthopedic and dental implants were made from. Today, mainly Ti and its alloys are used for manufacturing implants as Ti has a very high strength-to-weight ratio and is abundant. It has excellent corrosion resistance while being biocompatible. Its biocompatibility can be attributed to a thin (about 4 nm thick) oxide layer that forms on its surface [87]. It has been used since the 1960s in orthopedics with great success, but many reports have already been submitted that question its biocompatibility and point out the possibility of immunogenicity and inflammatory mediators [88]. An increasing number of patients with titanium allergy or intolerance leads to the development of other alloys or using other elements for orthopedic and dental implants. Moreover, adhesion of pure Ti is questionable, as it does not *truly* come in contact with bone but rather forms a thin (ca. 10 nm thick) non-mineral layer that prevents true adhesion. However, Ti still has over 50 years worth of data that proves its reliability, especially in restorative dentistry, dating back to the first Brånemark implant in 1965. Mechanical properties of pure titanium according to the ASTM [89] standard are given in Table 4.

Table 4: Mechanical properties of different grades of commercially pure titanium (cp-Ti) according to the ASTM standard [89]. Note that ASTM F67 Gr. 5 Ti is, in fact, the Ti-6Al-4V alloy (while sharing the cp-Ti grade numbering) according to the ASTM standard nomenclature. Last β alloy included for comparison [90].

Alloy/grade	Compressive strength [MPa]	Offset yield strength 0.2% [MPa]	Elongation at fracture [%]	Elastic modulus [GPa]
ASTM F67 Gr. 1	240	170	24	103–107
ASTM F67 Gr. 2	345	275	20	103–107
ASTM F67 Gr. 3	450	380	18	103–107
ASTM F67 Gr. 4	550	483	15	103–107
ASTM F67 Gr. 5	860	795	10	114–120
Ti-30Nb-17Ta	530	N/A	47	71

Every external body inserted in contact with living tissue must be biocompatible to reduce the probability of adverse reactions. Both cp-Ti and Ti alloys fill this role very well, forming a thin oxide layer by electrochemical oxidation that ensures good corrosion resistance [41].

4.3 Ti-6Al-4V Alloy

The standard alloy that has been used for prosthetics, implants and other biomedical applications is Ti-6Al-4V. Its main benefits are an outstanding strength-to-weight ratio

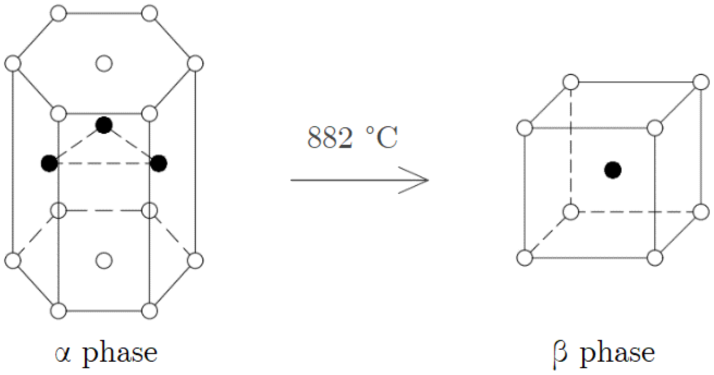

Figure 9: Both allotropic forms of Ti with their transus temperatures [92]. The structure on the left is called the hexagonal close-packed (HCP) structure, and the one on the right is the body-centered cubic (BCC) structure. The transus occurs at about 882 °C.

and excellent resistance to the external environment as it outmatches many other previous alternatives such as stainless steel or Co-Cr alloys [91]. The often-labeled *gold standard* alloy is 90% titanium, 6% aluminum and 4% vanadium and has a density of 4500 $\mathrm{kgm^{-3}}$. It is an α+β alloy as its elements stabilize both phases (Al is an α stabilizer and V is a β stabilizer). The α phase can be observed as an HCP structure and the β phase as the BCC structure; both are shown in Figure 9.

By alloying, it is possible to achieve various material properties. In the case of Ti-6Al-4V, the alloying elements are aluminum and vanadium. Aluminum, an α phase stabilizer, makes the alloy stronger, resistant to corrosion and improves weldability. Vanadium stabilizes the high-strength β phase below the transus temperature (ca. 882 °C after cooling, see Figure 9). Therefore, the whole alloy has the α+β character. Heat treatment and ageing cause precipitate formation in the material that does not enable movement of dislocations inside of it under load. The entanglement of dislocation loops subsequently captures and absorbs all cracks, creating a material that has greater toughness [93].

The Ti-6Al-4V alloy is usually made in 2 variants—the standard Ti-6Al-4V and Ti-6Al-4V ELI (Extra Low Interstitial), which is an alloy of higher purity that abides by stricter specifications for content of other elements (Fe, C, O) and also has less variance of Al content. It is, therefore, a more expensive, higher-quality alloy manufactured in a more controlled environment. Table 5 presents an overview of the chemical compositions of both alloy variants and cp-Ti of different grades.

Recently, an emerging, attractive alternative is the group of β Ti alloys, such as Ti-30Nb-17Ta. These alloys are free of Al and V, demonstrably toxic materials, have better biocompatibility and also ca. 10× lower value of corrosion current density than Ti-6Al-4V (0.078 $\mu A/cm^2$ for Ti-30Nb-17Ta compared to 0.686 $\mu A/cm^2$ for Ti-6Al-4V) [90]. Some of these alloys are included in Table 5, where their mechanical properties are listed.

Table 5: Chemical composition of different grades of cp-Ti and Ti-6Al-4V alloys [89,94–96]. Also published in my master's thesis [97].

Ti type	N	C	H	Fe	O	Al	V	Ti
cp-Ti Gr. 1	0.03	0.10	0.015	0.02	0.18	-	-	remainder
cp-Ti Gr. 2	0.03	0.10	0.015	0.03	0.25	-	-	remainder
cp-Ti Gr. 3	0.03	0.10	0.015	0.03	0.35	-	-	remainder
cp-Ti Gr. 4	0.03	0.10	0.015	0.05	0.40	-	-	remainder
cp-Ti Gr. 5 (Ti-6Al-4V)	0.05	0.08	0.015	0.30	0.20	5.50–6.75	3.50–4.50	remainder
Ti-6Al-4V ELI	0.05	0.08	0.012	0.10	0.13	5.50–6.50	3.50–4.50	remainder

4.4 Beta Ti Alloys

The defining attribute of β Ti alloys is their ability to remain 100% stable after cooling back from the β phase temperature back to room temperature. This stability is achieved by alloying titanium with β-stabilizing elements. By adding different elements, we can stabilize different titanium allotropic structures. Some elements can lower the transus temperature at which the transformation from the α to β phase occurs. This temperature is considered the lowest temperature at which titanium has 100% β phase. Other elements can be used for increasing the size of the β or α phase or to create their combination [98].

4.4.1 Beta Phase Subgroups

Generally, β Ti alloys can be subdivided into three groups. They are the pseudo β alloys, metastable β alloys and stable β alloys. For the scope of this thesis, I focus mainly on the second group, the metastable β alloys, which have excellent biocompatibility and are suitable for use in implants [99].

Metastable β Ti alloys mainly comprise of the BCC β phase, but can also contain a small amount of martensitic, non-thermal ω phase and particles of HCP α phase based on the alloy's composition and its thermomechanical processing [99]. One of the main characteristics of metastable β titanium alloys is their high amount of β-stabilizing elements. Thanks to this high amount, it is possible to preserve almost 100% of the metastable β phase after cooling back to room temperature from the field of the β phase above the transus temperature (ca. 882 °C). As an example of these alloys, we can mention the Ti-3Al-8V-6Cr-4Mo-4Zr alloy, which is often used in aerospace engineering for bolts and screws [100].

Table 6: Critical concentrations (wt.%) of β-stabilizing elements of binary Ti alloys required for 100% preservation of the BCC β phase after cooling back to room temperature by various authors.

Element	Isomorphous or eutectoid	Crit. conc. (wt.%) [98]	Crit. conc. (wt.%) [101]	Crit. conc. (wt.%) [102]
Molybdenum	Isomorphous	10.0	10.0	10.0
Niobium	Isomorphous	36.0	28.0	28.0
Tantalum	Isomorphous	45.0	22.0	22.0
Vanadium	Isomorphous	15.0	6.7	12.5
Tungsten	Isomorphous	22.5	4.4	5.9
Cobalt	Eutectoid	7.0	14.3	26.7
Copper	Eutectoid	13.0	7.7	15.0
Chrome	Eutectoid	6.5	16.0	18.4
Iron	Eutectoid	3.5	29.0	19.3
Manganese	Eutectoid	6.5	15.4	22.6
Nickel	Eutectoid	9.0	11.1	24.6

4.4.2 Development of Beta Alloys and the MoE Index

The first titanium materials and alloys to hit the market were either cp α Ti or its basic alloy Ti-6Al-4V (or its pure ELI variant). These alloys were initially designed for use in aerospace engineering but also found use in biomedical engineering thanks to their biocompatibility [99]. However, recent development focuses on producing alloys without Al or V as their cytotoxicity was reported about 20 years ago already [103]. Vanadium is cytotoxic mainly in its V4+ and V5+ forms and in the form of oxides such as V_2O_5, which badly influences the reproduction cycles of mammals [104]. Despite being less toxic than vanadium, aluminum is also connected to adverse effects, such as neurotoxicity and Alzheimer's disease [105].

Another shortcoming of α+β alloys compared with β alloys is their low abrasion resistance, resulting in continuous particle debris deposition inside the patient's body. The α+β alloys also have relatively high elastic modulus E compared with human bone (α+β alloys have ca. 110–120 GPa, human bone has ca. 25–30 GPa [106]) which is a significant mismatch and leads to the stress shielding effect that is described in detail in Chapter 2.4. This mismatch led to the development of β Ti alloys, which can be designed to have much lower moduli.

The β Ti alloys took off in the 1990s when many new alloys were developed. Before listing them, we can explain the molybdenum equivalency index (MoE). This dimensionless number states the ratio between the stabilizing effects of an element compared to that of molybdenum (Mo). Molybdenum was cited as a reference element as it is one of the most significant β-stabilizing elements of Ti alloys. For example, we can mention the Ti-16Mo alloy, which has MoE = 15, as molybdenum has an index of MoE = 1. Iron has MoE = 2.9, therefore being 2.9× stronger β-stabilizer than molybdenum. Examples of aforementioned alloys are namely Ti-29Nb-13Ta (MoE = 11.0), Ti-29Nb-13Ta-4.6Zr (MoE = 10.2), Ti-12Mo-6Zr-2Fe (MoE = 16.8), Ti-13Nb-13Zr (MoE = 1.4), Ti-25Nb-5Ta-7Zr (MoE = 9.7) and Ti-15Mo (MoE = 15.0). These alloys have much lower values of elastic moduli E when compared with traditional materials (Figure 10) and another benefit is the use of non-toxic elements as they do not contain Al or V [99]. It is important to mention that molybdenum equivalency is an empirical instrument based on comparison of binary Ti alloys. For clarity, the MoE indices are shown in Table 6, where critical concentrations of individual elements for preserving 100% of the β phase after cooling to room temperature are listed (notice that the critical concentration of molybdenum is 10% and its MoE = 1). The MoE index can be further supplied with Figure 10, where binary, ternary and quaternary Ti alloys are sorted by their MoE index.

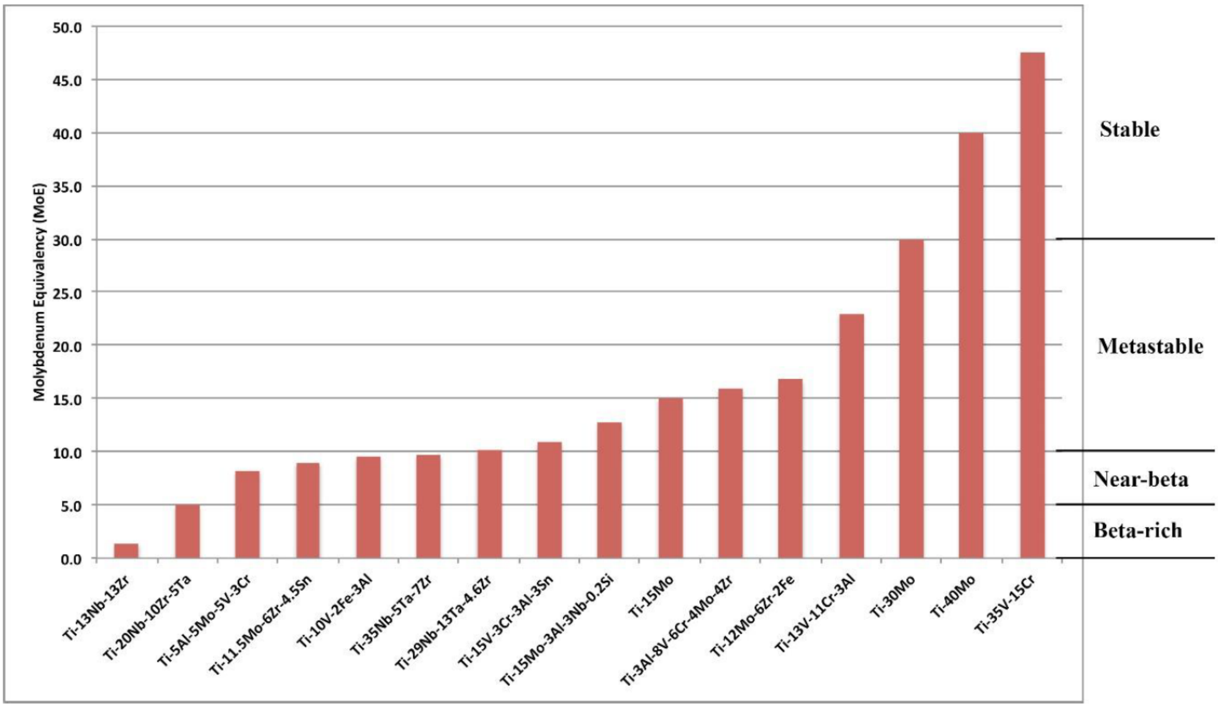

Figure 10: Binary, ternary and quaternary commercially significant β Ti alloys. Categories are as follows: 0 < MoE < 5 alloys are β-rich, 5 < MoE < 10 alloys are pseudo β, 10 < MoE < 30 alloys are metastable and MoE > 30 are β-stable [99].

4.4.3 Beta-Ti Alloys Cell Proliferation

The β Ti alloys also show they are much better in cell proliferation when compared with α+β alloys. The results of Hussein et al. [90] show that the main cause of cytotoxicity is the release of metal ions, which is greatly inhibited in their tested β Ti alloy (Ti-17Nb-6Ta) because of the compact surface granted by a very firm oxide layer and the resulting corrosion resistance, which was measured to be 10× better than that of Ti-6Al-4V. Cell proliferation of Ti-Nb-Ta alloys was reported to be in the range of 94–98% when tested for cytotoxicity. Furthermore, as the release of metal ions from materials could not be completely eliminated, the correlation with cell proliferation implies that alloying with Nb and Ta shows no cytotoxic effect [107].

Researchers Kuroda et al. [108] performed an experiment to investigate cytotoxicity of β Ti alloyed with tantalum and varying amounts of zirconium and found no amount of the β-stabilizing Zr is cytotoxic for osteoblasts.

Authors Li et al. [109] investigated another β Ti alloy, the Ti–26Nb–2Fe–4Sn alloy, and found that its has good potential for biomedical applications as it has a very low modulus $E = 58$ GPa and good yield and tensile strength strength (592 and 622 MPa, respectively), while showing better cell viability than their control group after 7 days of culturing.

Cardoso et al. [110] performed cytotoxicity tests on their β Ti-Mo-Nb alloy and found it viable with good adhesion and no cytotoxic effect.

The literature on β Ti alloys is rapidly broadening and these findings of other authors show that β Ti alloys will be relevant in the future—once they become more accessbible. Also, they are going to be very helpful in reducing the stress shielding effect as they generally have much lower moduli that match better with human bone.

5 Market Research

As a follow-up to the material research, the following market research is provided regarding the choice of materials in dental implants, where I originally intended to use porous structures. It should be restated, though, that porous structures are not limited to dental implants. On the contrary, they are very well-suitable for bigger implants, such as femoral or acetabular components and other applications. Table 7 shows the basic geometry, material choices and other properties of dental implants from various European manufacturers. The short research shows that discussed post-processing methods are applied even in traditional machining methods. The table also shows that the most common materials are the Ti-6Al-4V alloy and various forms of cp-Ti. The most commonly used materials in metal SLS and SLM 3D printing are also Al, Ti, steel and their alloys (each with various and different challenges, such as oxide layer formation and low boiling point for Al or relatively high costs for powdered Ti and its alloys) [111].

Table 7: Summary illustrating the materials and post-processing methods of some of the most important European dental implant manufacturers who use machining. The table shows that the majority of manufacturers still mostly use the trusty Ti-6Al-4V alloy, with variants of cp-Ti in second place. The information is gathered from the manufacturers' websites and may be incomplete for some of them because of their policies.

Manufacturer	**Material**	**Treatments and notes**
Lasak	cp-Ti grade 4	Bridges and individual abutments. Also CoCr, Ti, ZrO_2.
Straumann	Ti-15Zr, ZrO_2	Roxolid Ti-15Zr implants and cp-Ti abutments.
Medico Dent	Ti-6Al-4V	Three implant systems. Also cp-Ti grade 4. Sandblasting, mechanical polishing.
Anthogyr	Ti-6Al-4V	
Bego Implant Systems	cp-Ti grade 4	Sandblasting, acid etching. Microstructured homogeneous surface TiPurePlus.
BioComp Dental	Ti-6Al-4V	
Bredent	Ti-6Al-4V	
Camlog Implant system	Ti-6Al-4V	Ceramic particle blasting, acid etching.
Dentatus	Ti-6Al-4V	Ceramic particle blasting.
Dentaurum	Ti-6Al-4V	Ceramic particle blasting.

Dentsply	cp-Ti grade 4	
IhdeDental	cp-Ti grade 4, Ti-6Al-4V	Sandblasting, electrochemical activation.
Eckerman Dental Implant system	cp-Ti, Ti-6Al-4V	
Implants Diffusion International	Ti-6Al-4V	
JMP Dental	cp-Ti grade 4, Ti grade 9 (Ti-3Al-2.5V)	
Leone	Ti-6Al-4V	Sandblasting, particles R_a=25 µm.
Nobel Biocare	cp-Ti grade 4, Ti-6Al-4V	Implants cp-Ti grade 4, arch replacements Ti-6Al-4V.
OsteoCare Dental Implant System	Ti-6Al-4V	
Schütz Dental	cp-Ti grade 4, Ti-6Al-4V	Ca. 75% cp-Ti grade 4 and ca. 25% Ti-6Al-4V.
SIC invent	cp-Ti grade 4	
Sweden & Martina	Ti-6Al-4V	
Sybron Implant Solutions	cp-Ti grade 4, Ti-6Al-4V	
TBR implants group	cp-Ti grade 4	Sandblasting, acid etching, gingival implant zirconium Y-TZP.
Timplant	cp-Ti grade 4	
ZL-Microdent Attachment	cp-Ti grade 2	
Dental Tech	Ti-6Al-4V	Sandblasting, acid etching, some gingival components mechanically polished.
Alpha-Bio Tec	Ti-6Al-4V ELI	NanoTec surface—coarse grain sandblasting and acid etching

Furthermore, authors Oliveira and Reis [112] did an extensive study on manufacturers of dental implants, their manufacturing methods and other important properties of implants in 2019. They found that the most popular method among AM processes is SLS, followed by SLM and EBM. They also stated that among the reviewed group of implants by various manufacturers, AM-made implants offered the same or better performance in mechanical tests, evaluation of micro CT imaging and histological analyses compared to their machined counterparts.

Moreover, case reports with follow-ups between two months and five years showed good osseointegration, bone-implant connection, and continuous bone remodeling. However, the same reports also showed two fractures of 3D-printed implants in a 5-year follow-up without citing a cause. These were probably cased by inadequate quality control as discontinuities in porous parts ultimately reduce fatigue strength, as discussed in Chapter 3.5. Also, we can easily attribute that the prevalence of Ti-6Al-4V is present because it is an already established material (unlike most β Ti alloys), and manufacturers do not need to go through a lengthy legislative process to use it in their products.

6 The Gyroid Structure

The gyroid structure is the central point of innovation the thesis tries to bring forward and I present a way it could enrich manufacturing of implants. The gyroid can take various forms but is essentially a triply-periodic minimal surface (TPMS) structure that is combined using the sine and cosine functions to create a porous system of interconnected pores.

6.1 Minimal Surfaces

Minimal surfaces (a category where the gyroid belongs) are—by their very nature and name—surfaces that span a specific boundary and create the smallest possible area for their boundary curve (this is synonymous with having zero boundary curvature).

In the past (prior to the widespread computer era, ca. before the year 1990), various mathematical methods had to be applied to prove the existence of newly-created minimal surfaces as their visualisation is not easy for the human mind nor they are easy to draw on a piece of paper [113]. Today, the application of modern numerical methods enables this process much better.

The easiest-to-imagine minimal surface is the soap bubble. It forms if we submerge a piece of a closed, bent wire into a soap solution. The bubble will form a minimal surface that encompasses its boundary. The resulting surface will be minimal as the surface tension at every point of the surface is in equilibrium. In differential geometry, this can be translated into having zero mean curvature. In other words, the curvatures along the principal curvature planes are opposite and the same at every point. This characteristic implies that every point on the surface is a saddle point. See the illustration in Figure 11. The definition of zero mean curvature can be provided by Equation 2:

$$H = (k_1 + k_2)/2 = 0 \tag{2}$$

where H is mean curvature of the surface and k_1 and k_2 are curvatures in the principal curvature planes of the surface [114].

6.2 Triply-Periodic Minimal Surfaces (TPMS)

The structures shown in Figure 12 are TPMS named after Neovius (1883), Fischer and Koch (1988) and the gyroid came about in May of 1970 in a technical note of the NASA scientist Alan Schoen titled *Infinite periodic minimal surfaces without self-intersections* [116].

Also, it has to be granted that they possess translational symmetry and do not intersect, as finding surfaces that intersect is not an interesting problem as they are abundant [113].

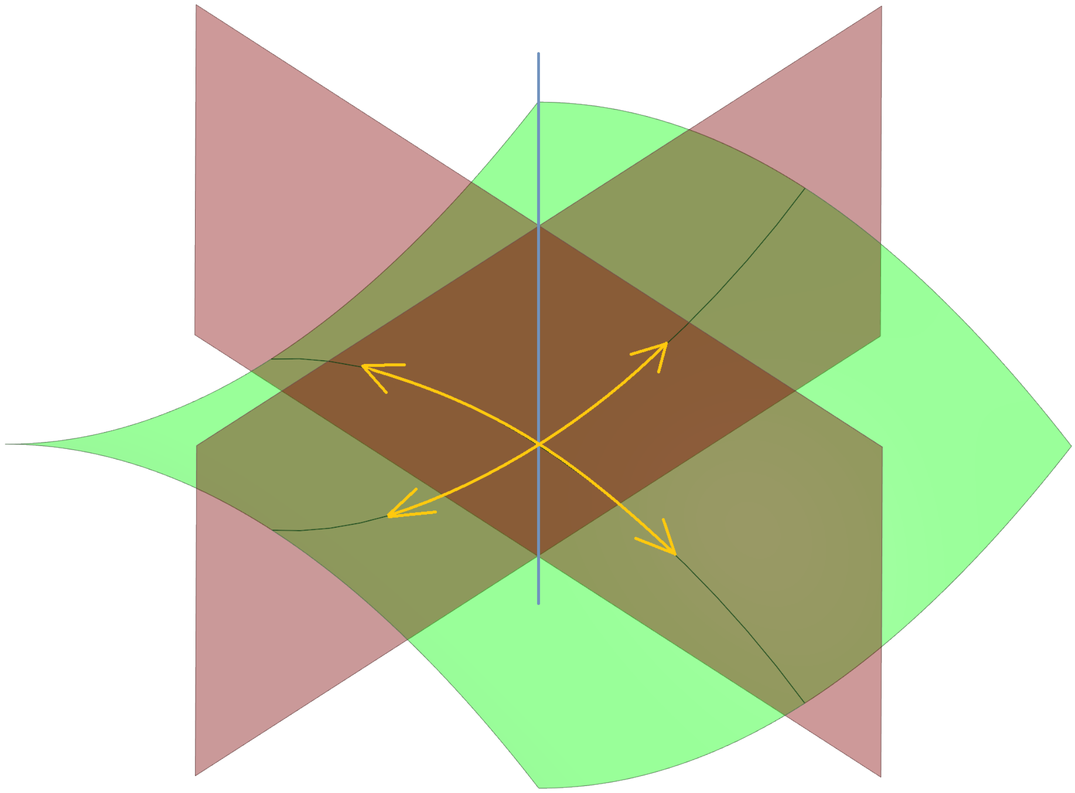

Figure 11: Every point on a minimal surface (green) has to have zero mean curvature. This manifests along the principal curvature planes (red) on an example of a saddle. This saddle can, in fact, be found at any point of any minimal surface by definition. If we rotate the section plane and display another cutout with a different normal vector (portrayed here as the blue line formed by intersecting the principal curvature planes), the same will hold true.

Notably, TPMS structures are not symmetrical in their mirror planes but have translational symmetry instead.

6.3 Gyroid Construction

In the previous chapter, we discussed TPMS in general. We can take the process a step further and try to generate a structure instead of a surface. A gyroid structure generated this way has one solid phase and one void domain. We can approximate the gyroid with a relatively simple equation given below:

$$sin(\overline{x})cos(\overline{y}) + sin(\overline{y})cos(\overline{z}) + sin(\overline{z})cos(\overline{x}) - t = 0 \tag{3}$$

Equation 3 represents the *single* gyroid structure. Symbols $\overline{x}$, $\overline{y}$ and $\overline{z}$ are modified spatial coordinates defined as:

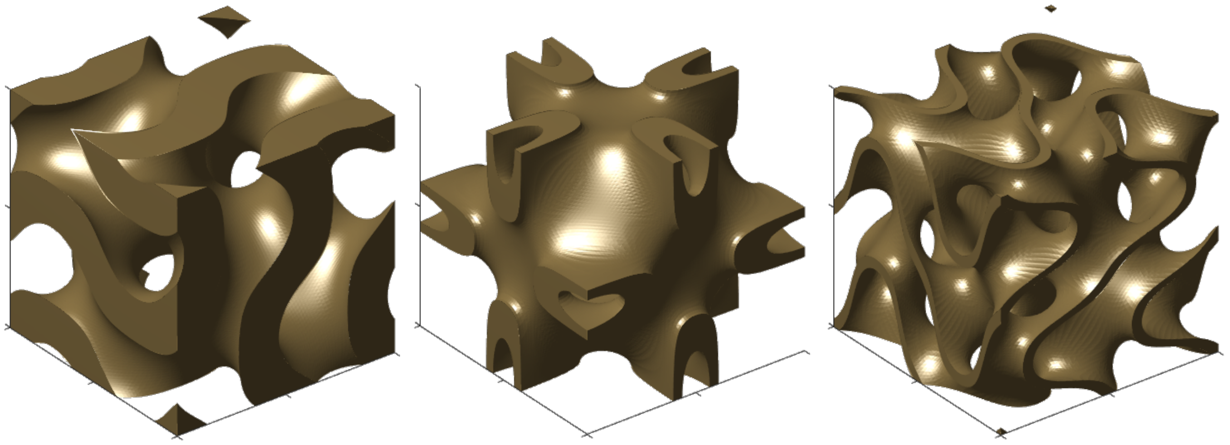

Figure 12: Various TPMS structures embedded in a unit cube. From left—the gyroid structure, Neovius structure, Fischer-Koch S structure. Note that porosity is not the same for demonstration purposes. All sides have a length of π. Figure taken from my published work [115].

$$\overline{x} = \frac{2\pi x}{a}, \quad \overline{y} = \frac{2\pi y}{a}, \quad \overline{z} = \frac{2\pi z}{a}$$

where a is the edge length of the gyroid's circumscribing cube and the constant curvature of the gyroid structure is determined by the parameter t. With variations of t, we can achieve different structural characteristics. The gyroid resembles (according to its t value) either a *tubular* (trabecular, beam) or a *sheet* (wall) system. However, manipulation of t should be done with caution as t has limitations, mainly manifesting with coarse meshes, as shown in Figure 13.

After generating the gyroid TPMS, a CAD (Computer-Aided Design) environment can be used to enclose the desired domain and create a solid structure (gyroids generated this way have one solid and one void domain). In Figure 14, we can observe the differences between the tubular and sheet variants of the structure. Also, authors Li et al. [117] corroborate the study of parameter t by stating $t = 1.41$ breaks the structure's connections for the tubular variant and eliminates the possibility of clearing up debris after printing for the sheet variant (too dense and pores are no longer interconnected). Also, specifying $t = 0$ divides the design space into two fractions with identical volumes. The subsequent enclosure of one of the domains then creates a gyroid with a 50% density [117]. Moreover, Li et al. found the governing equation for relative density of the gyroid. This equation was acquired by data fitting of repeatedly generated gyroids with different densities to be as shown in Equation 4.

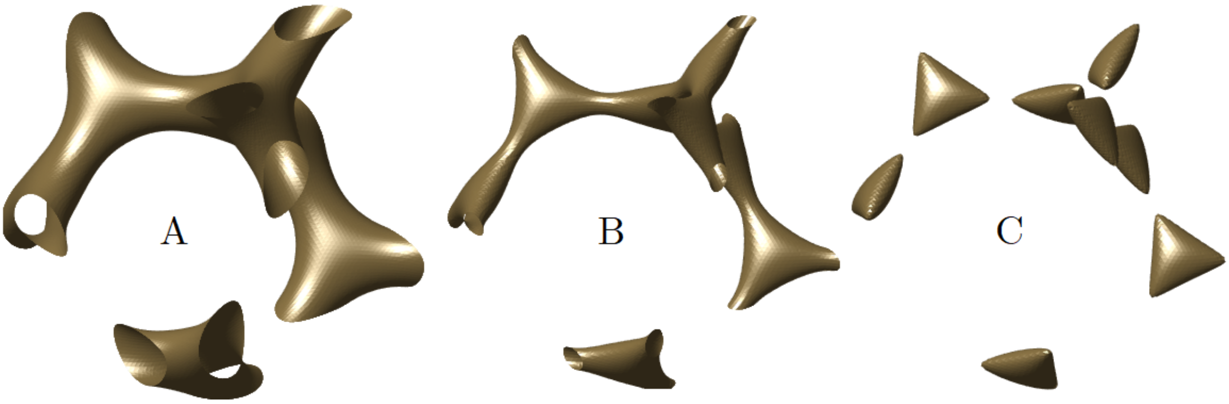

Figure 13: Single gyroid tubular TPMS generated with Equation 3 with different values of parameter t. Surfaces need to be enclosed for FEM in order to perform analyses on solids. The boundary cube has a length of $a = 2\pi$. A) $t = 1.2$, B) $t = 1.38$, C) $t = 1.41$. The parameter t has a domain of $(-1.5; 1.5)$. When approaching values of $t = \pm 1.5$, deformities, discontinuities and other losses of shape start to occur. Notably, these discontinuities are not truly disconnected surfaces, but they are so thin that the triangulation used to tessellate the structure would have to be so fine that it would increase the generating time dramatically. Here, the tessellation has the same coarseness across all values of t, so the thin surfaces at C) are not represented at all. Figure taken from my published work [115].

$$\rho_g = 0.3325 \cdot t + 0.501 \tag{4}$$

where $|t| \leq 1.5$. Therefore, specifying a $t = 1.41$ gives us a density of $\rho_g \doteq 0.970$ (almost completely solid) and $t = 0$ gives $\rho_g \doteq 0.501$, as previously stated to be the case.

So far, we have introduced the geometry of the single gyroid structure, but there are many other gyroids. The following equation describes the double gyroid structure:

$$\Big[sin(\overline{x})cos(\overline{y}) + sin(\overline{y})cos(\overline{z}) + sin(\overline{z})cos(\overline{x})\Big]^2 - t^2 = 0 \tag{5}$$

where all parameters have the same meaning as in Equation 3. The graphical representation of the structure is displayed in Figure 16.

Chirality (handedness) is another important property of the gyroid structure—it does not possess mirror symmetry but rather translational symmetry. It is naturally asymmetric, and as Chin and Coveney [118] proved, its BEC cannot be divided along any plane or axis and superimposed on the other part.

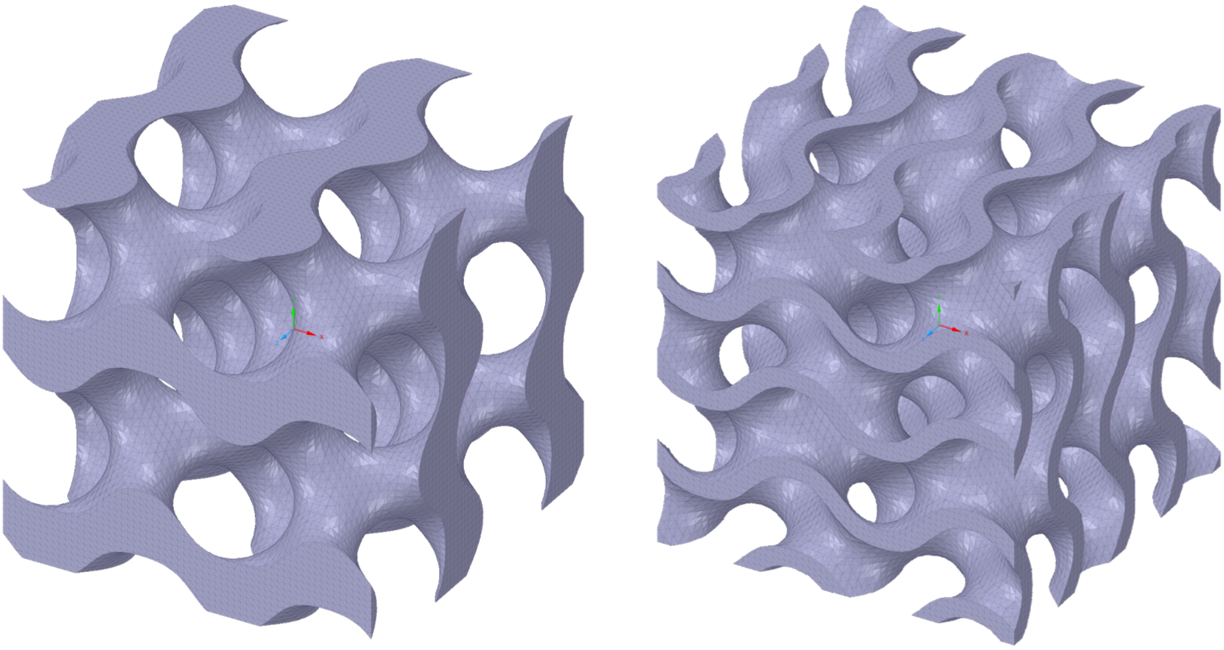

Figure 14: Both variants of the single gyroid structure that have different values of parameter t. Left—the tubular (beam-like) system, right—the sheet (wall-like) system. The image shows structures with different porosities for ease of understanding. Notice the aforementioned minimal characteristic of the surface—any given point on the surface is a saddle point with properties mentioned in Figure 11. Both variants have a length of 2π. Notice how the tubular variant on the left resembles the trabecular structure described in Chapter 7.3. The trabecular character will later prove unreliable because of the beams' splitting, making the wall-like character of the sheet variant superior. Figure taken from my published work [115].

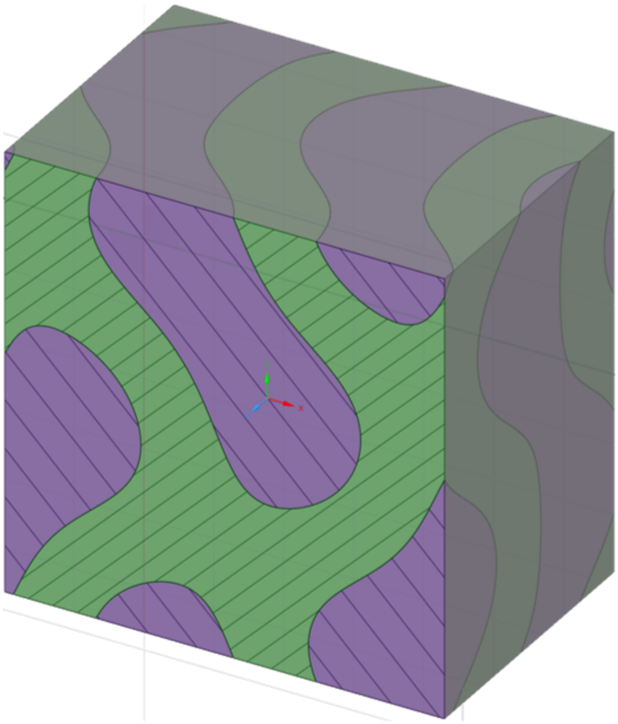

Figure 15: A cross-section of a BEC of a single gyroid (purple) structure with the remaining volume of a circumscribed unit cube—the void domain—filled with another solid (green). Interestingly, the void domain is another gyroid structure, usually with an inverse character (tubular vs. sheet). The character of either structure is influenced by the parameter t. Figure taken from my published work [115].

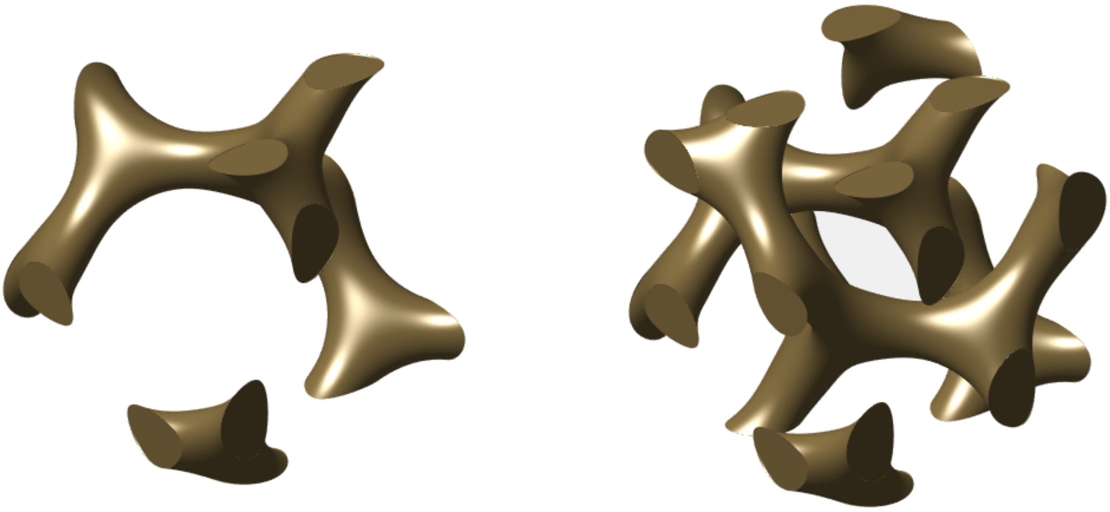

Figure 16: Illustration of the double gyroid structure on its tubular variant. The left picture shows a single gyroid structure for comparison, and the one on the right is the double gyroid generated using Equation 5.

6.4 Functional Grading

Gradient porosity (or material grading, tailored material distribution) is a novel way of designing structures that need to fit specific criteria for applications where continuity needs to be maintained, but the function of the structure varies across its geometry. As an example, we can imagine that we need the best (highest) values of mechanical properties at the core of the implant, where forces are generally going to be at their highest, but less so at the implant's peripheries where the load intensity goes down and the need to maintain a good, open porosity for bone ingrowth takes precedence. I would also like to point out that graded gyroid structures should work very well as structurally functional heat exchangers due to their manageable density profiles and controllable and vast surface area (Figure 17). Therefore, we can modify the porosity to adhere to our needs according to the location.

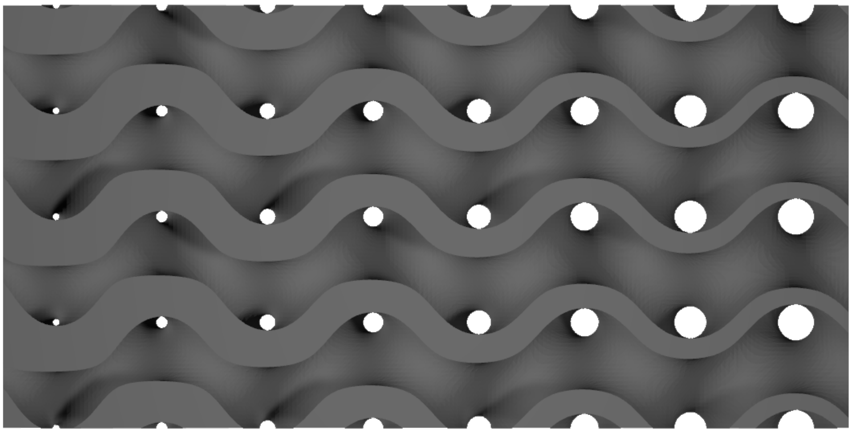

Figure 17: Functionally graded gyroid .STL model with porosity varying from 20% to 80% in the left-right direction. This variation in porosity can potentially be explored to also be radial or multidirectional. Varying porosity can be beneficial when the design calls for a homogeneous implant core (0% porosity) and an outer osseointegration layer with a designed porosity for bone ingrowth as specified in Chapter 2.2. This gradient structure and its potential are not investigated in the thesis but are mentioned in its Conclusions. Its construction and application on an implant would require more attention as the porosity would need to be continuously changing radially from the center to the outer surface and from the tip of the homogeneous stem toward the implant's apex—hemispherically, in two directions. However, if the mathematical apparatus was developed, it could provide an interesting and unusual custom-made implant design.

7 Micromechanical Analyses

For objective comparison of mechanical properties of intraosseous parts of dental implants, segments of human teeth and materials used for conventional implants (the standard Ti-6Al-4V alloy) and specimens made by AM (namely 3D printing using the Rematitan Ti-6Al-4V powder), micromechanical analyses were performed. The micromechanical tests were conducted in the Faculty of Civil Engineering, CTU Prague laboratories using a CSM Instruments Nanoindenter. Also, a microscopic analysis of 3D-printed specimens was performed, and the mechanical properties of trabecular structures were evaluated.

The results of both types of mechanical tests are essential to understand the behavior of the gyroid structure. Most of the following results were published in my authored or co-authored works, where I participated by preparing meshes for FEA.

7.1 Analysis Parameters

The results of experiments can be the primary input parameters for numerical modeling of two-phase tissue models and other simulations of mechanical behavior of porous structures manufactured using additive technology and conventionally machined implants. Micromechanical analyses can then serve for the verification of material properties given by the manufacturer of the material (this has a good use in 3D printing where sintered or melted metal powders are used). Also, they can be used to compare 3D-printed and traditionally machined specimens. For the purpose of this analysis, a nanoindentation measurement with the aim of comparing the Ti-6Al-4V Rematitan alloy used for 3D printing and the conventional Ti-6Al-4V ELI alloy used for machined implants was performed. These results are then confronted (Table 8) with results of micromechanical measurements of human enamel and dentin known from previous experiments [119–121].

The analyses were performed using the CSM Instruments Nanoindenter (Anton Paar, GmbH, Graz, Austria) in the laboratories of the Faculty of Civil Engineering, CTU Prague. The specimens were embedded in epoxy resin, cut in the transverse direction on a slow-spinning saw and subsequently ground and polished until the desirable quality was reached. Sandpapers with grit of 1200–4000 were used. Concerning the elimination of surface tension and shear stiffness in the atom structure of the material, the mode of directed force with cyclic loading and a force range of 10–70 mN was used. The force was delivered in seven cycles at a loading velocity of 180 mN/min. The graph of the loading curve is shown in Figure 18. Analyses of micromechanical properties have shown their dependence on indent depth (load force) across all specimens (Figure 20).

7.2 Nanoindentation of Human Teeth and Ti-6Al-4V

Conducted analyses show a difference of microhardness H_{IT} and reduced modulus E_r between biological materials and the Ti-6Al-4V alloy (both forged and 3D-printed). On the contrary, the Ti-35Nb-6Ta alloy shows a good match of mechanical properties with human enamel. A good match of material properties is beneficial as it decreases the effects of stress shielding (Chapter 2.4). This comparison is not given on E but on values of reduced elastic modulus E_r. Since no common and biocompatible material to this date can match the properties of cancellous bone (a metal that would have the *global* modulus E so small), another approach is to develop porous structures (see Chapter 6.1).

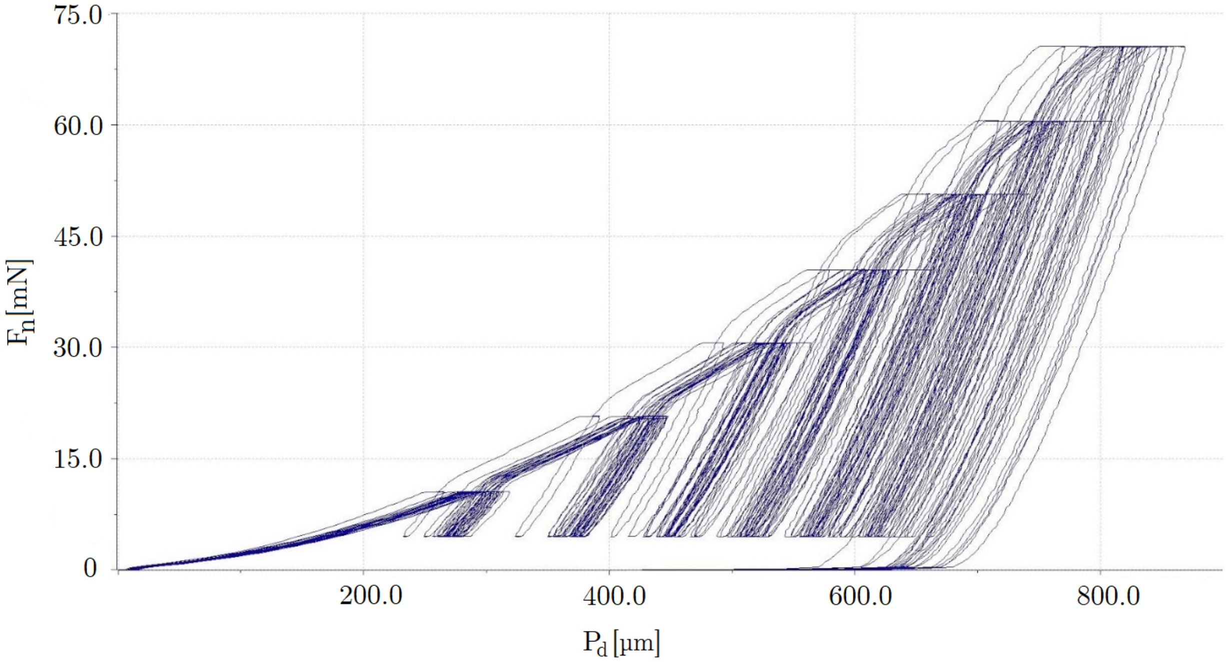

Figure 18: Indentation curves from the cyclic analysis describing the relationship between indent depth P_d and loading force F_n in the Ti-6Al-4V Rematitan material.

Table 8: Comparison of basic micromechanical parameters (H_{IT}—reduced hardness, E_r—reduced elastic modulus) in analyzed materials using a load force of 30 mN. Some values are a part of my previous works [97, 119–121] and also [122].

Parameter	Dentine	Enamel	Ti-6Al-4V forged Medin	Ti-6Al-4V forged Straumann	Ti-6Al-4V forged Lasak	Ti-6Al-4V 3D-printed ProSpon	Ti-35Nb-6Ta forged ÚJP Praha
H_{IT} [GPa]	1.057	3.790	4.580	3.420	3.306	5.187	2.984
E_r [GPa]	26.9	79.7	118.5	117.4	115.9	118.1	81.6

7.3 Nanoindentation of Trabecular Structures

The AM technologies offer wide variability in structural geometry and morphology of intraosseous parts of implants. From the solution of previous projects, we had several specimens of trabecular structures at hand. For the purpose of micromechanical analyses, Diamond 14 type structure specimens were manufactured (Figure 19).

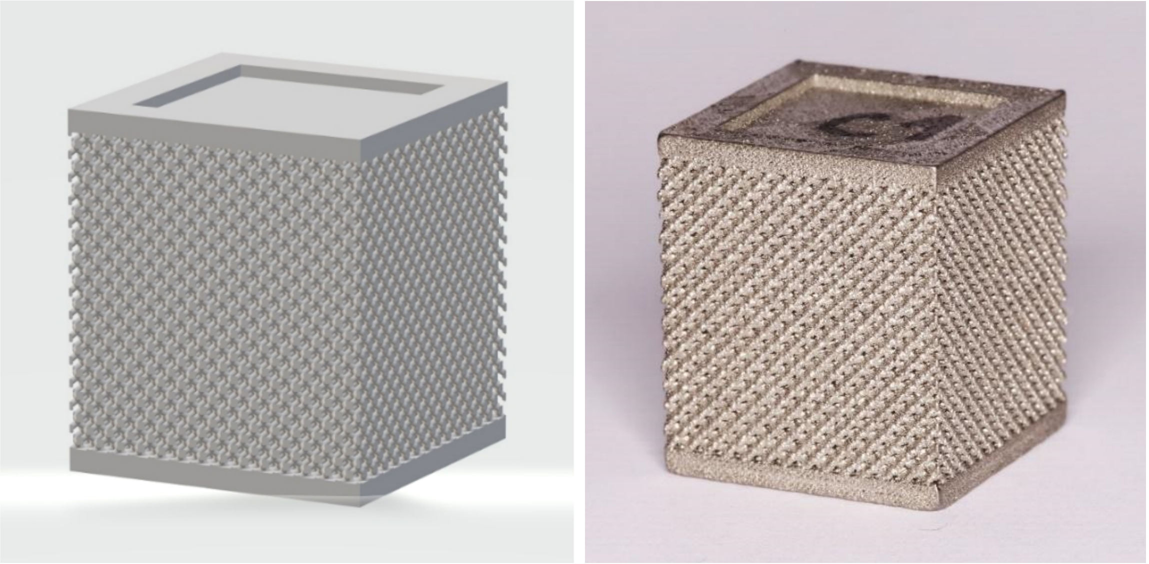

Figure 19: The geometry model (left) and a 3D-printed specimen (right) of the Diamond 14 trabecular structure made by the ProSpon company. The specimens were 3D printed using the Rematitan Ti-6Al-4V metal powder using the SLM technology. Figure taken from a co-authored published work [123].

This structure was also embedded in epoxy resin and cut in the transverse direction, then ground and polished to desirable quality with sandpapers with a grit of 1200–4000. The indentation measurement was performed on the edge of the specimen and in its center. Indentation at different locations was performed to determine the homogeneity of mechanical properties across the cross-section. The main parameters were reduced hardness H_{IT} and reduced modulus E_r. Loading was performed in the mode of controlled force in cyclic mode with a range of 10–70 mN. Graphs presented in Figure 20 show a significant spread of properties between the specimen's edges and its center.

The trend of E_r shows much greater dependence on the location of the indent than H_{IT}. For smaller forces, the difference in these properties between the specimen's center and its edges is ca. 15%. For maximal force, this difference is ca. 40% already. Great spread of E_r can be attributed to heat treatment, which is necessary to perform after printing to stabilize the inner tension of the specimen.

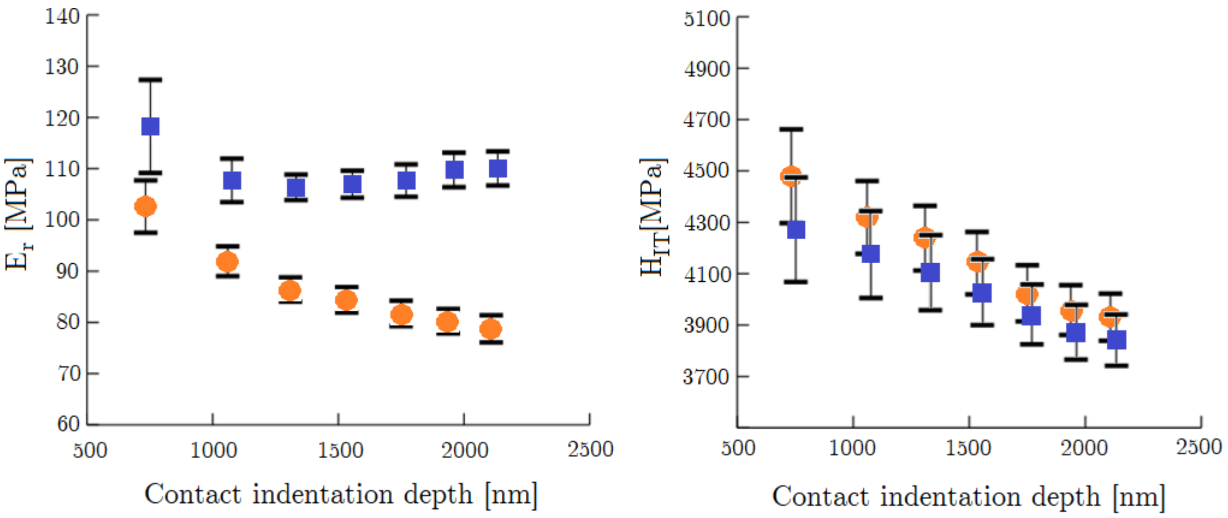

Figure 20: Dependence of reduced modulus E_r (left) and reduced hardness H_{IT} (right) on indentation depth measured during cyclic loading. Blue squares represent the specimen's center; orange circles represent its edges [122].

7.3.1 Microscopic Analysis of Trabecular Structures

Basic optical analysis on the aforementioned trabecular specimens was performed to evaluate the morphology of the surface (see Figure 21 for defects). The surface morphology was mainly a point of concern due to discontinuities, defects and possible local geometry problems. The specimens that looked the worst to the naked eye were chosen for the analysis. These specimens were initially made for uniaxial tensile tests but were discarded for this test due to the observed defects. The tensile tests were instead realized on specimens with a modified geometry shown in Figure 24. More on this in Chapter 8.1. These defects could have happened during the production of the specimens due to uneven distribution of heat and uneven thermal expansion. Even though there are two junctions, the cracks only occur at one of them. As the printer moves the extruder head systematically up in the vertical direction, the first one, the *homogeneous-trabecular* junction, is problem-free. However, the cracks occur at the upper *trabecular-homogeneous* junction, as the trabecular part cools down from printing temperatures rapidly compared with the newly-built homogeneous part. Therefore, the trabecular beams contract at the upper junction, ripping themselves apart from the matrix and causing structural dislocations (Figure 21).

Another category of defects found by the optical analysis are discontinuities of individual beams inside the structure (Figure 23). These defects can cause particle debris, subsequent necrosis and aseptic loosening of implants (loosening without infection). The question arises as to whether widening the beams can eliminate this negative effect. The width of beams was 200–300 µm. With these settings, we approach the precision threshold

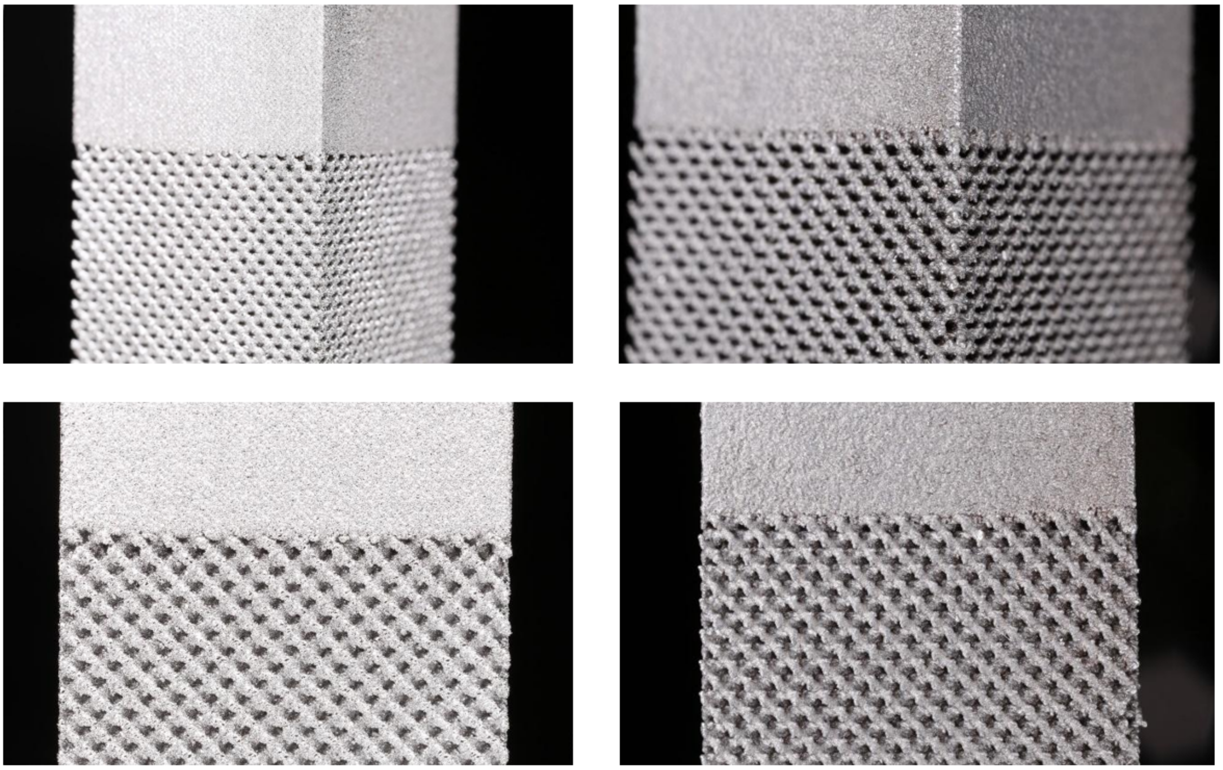

Figure 21: Optical images of defects formed at the trabecular-homogeneous junction. Left column—specimens made by ProSpon, spol. s.r.o., right column—specimens made by Global Biomedica, s.r.o.

of contemporary metal 3D printers. However, if we widen the beams, increasing the size of each individual cell, we also increase the size of the overall implant, which might be unacceptable for some applications. Another defect that was found was bits of slag located inside the structure (Figure 23). This defect should, however, not occur when applying the structure on the stem of an implant.

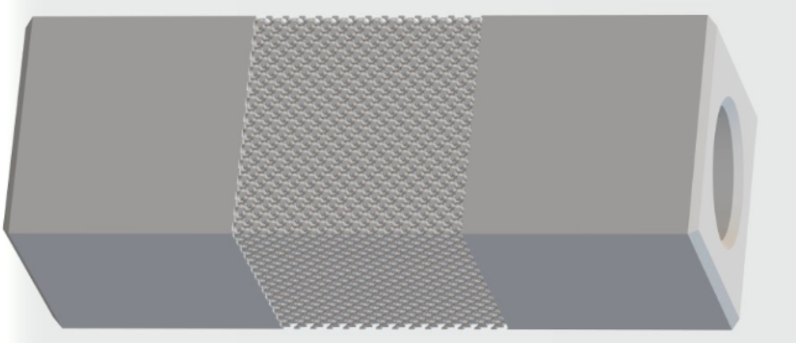

Figure 22: Original geometry model for the 3D-printed specimens (trabecular Diamond 14 structure, uniaxial tensile tests). The model was later modified due to printing defects.

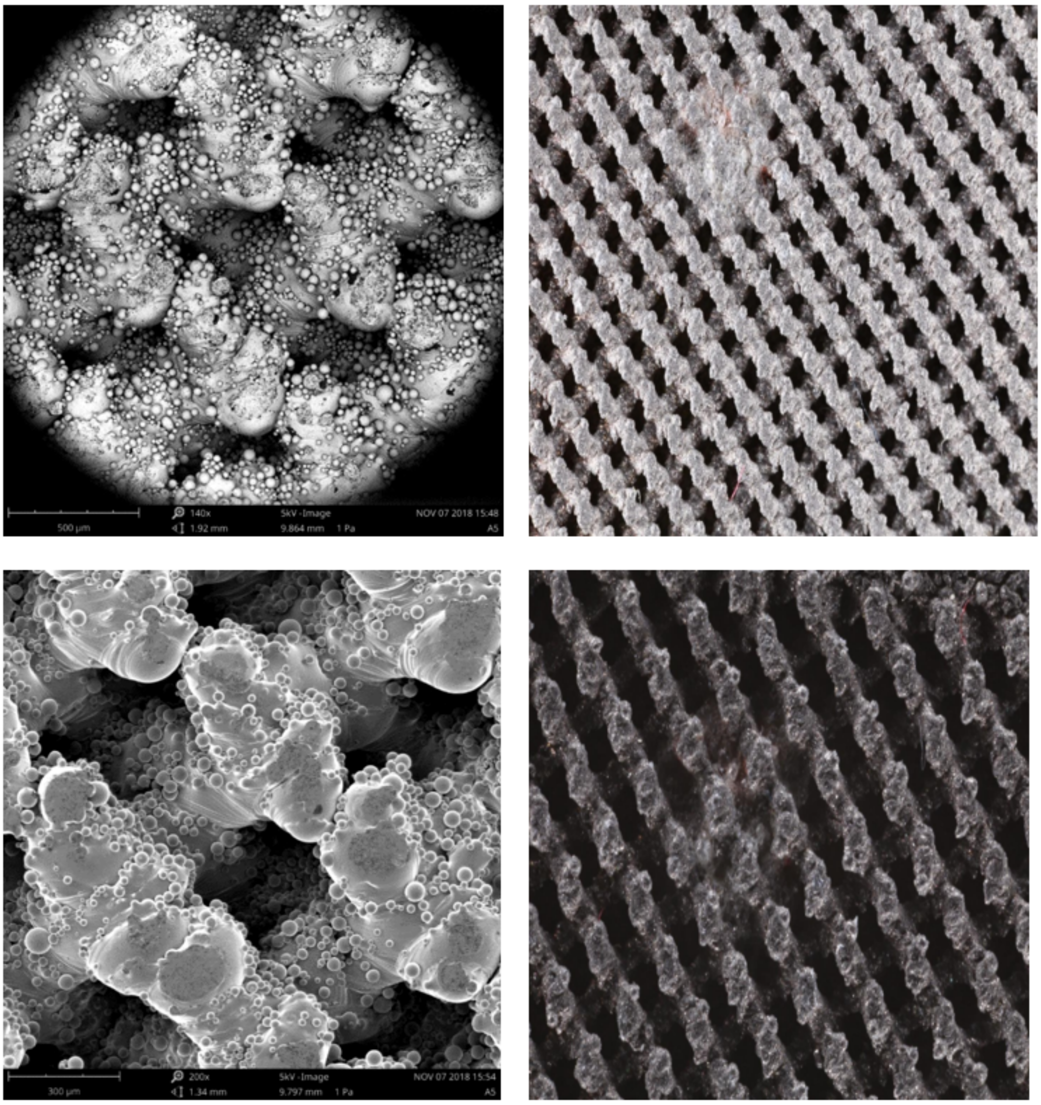

Figure 23: Discontinuities of the trabecular structure (left column, made by ProSpon spol., s.r.o.), slag inside the trabecular structure (right column, made by Global Biomedica s.r.o.).

8 Macromechanical Analyses

This section describes the compressive uniaxial tests that were performed on trabecular and gyroid specimens. Notably, tensile tests were also performed on both trabecular and gyroid specimens but are not evaluated in this section. The first batch of the specimens failed because of bad specimen design (Figure 21). Other specimen designs were made in the hope of remedying this unwanted phenomenon (Figure 24). This design flaw—which caused an uneven heat distribution during printing and tearing at junctions—was later fixed by making a new design displayed in Figure 25.

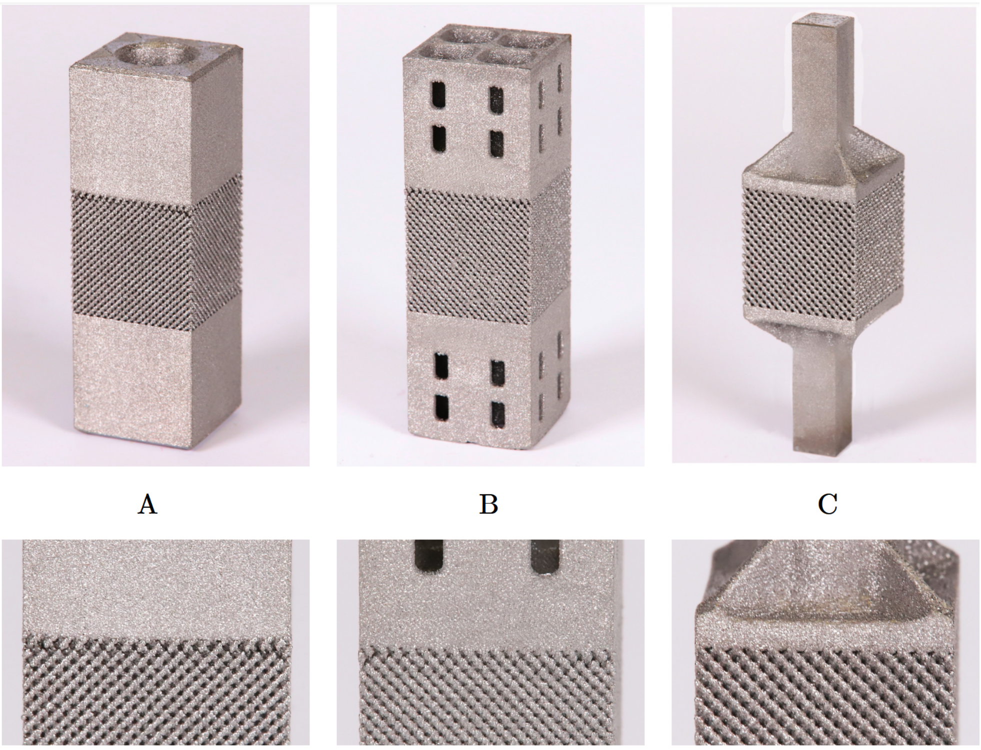

Figure 24: Evolution of the tensile trabecular specimen. Variants A) and B) both failed and tore at the trabecular-homogeneous junction. Eventually, variant C) provided a transition that enabled quick heat dissipation and did not tear after printing. Figure taken from a co-authored published work [123].

However, other trabecular and gyroid tensile specimen designs could not be successfully modified, and even the heat-optimized variant shown in Figure 24 had internal defects that were not initially identifiable and had brittle fractures or gripping failures (Figure 26). Therefore, the tensile tests had to be terminated because the results were unreliable. The following section, therefore, only offers results from uniaxial compressive tests.

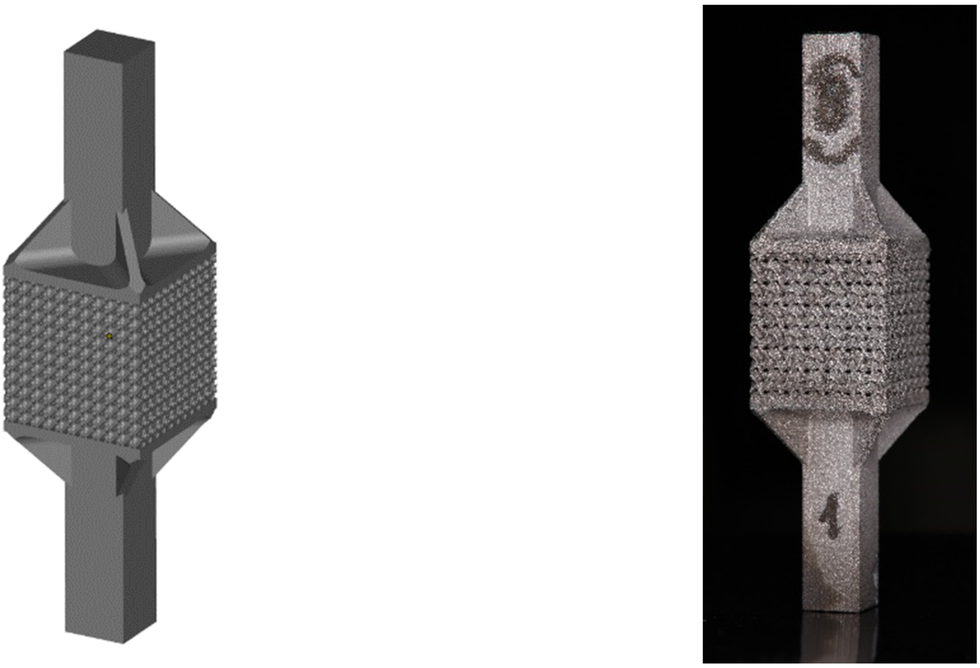

Figure 25: The modified model (left) and 3D-printed specimen (right) for the tensile test. This model solved the problem of tearing at the interfaces (Figure 21) [122].

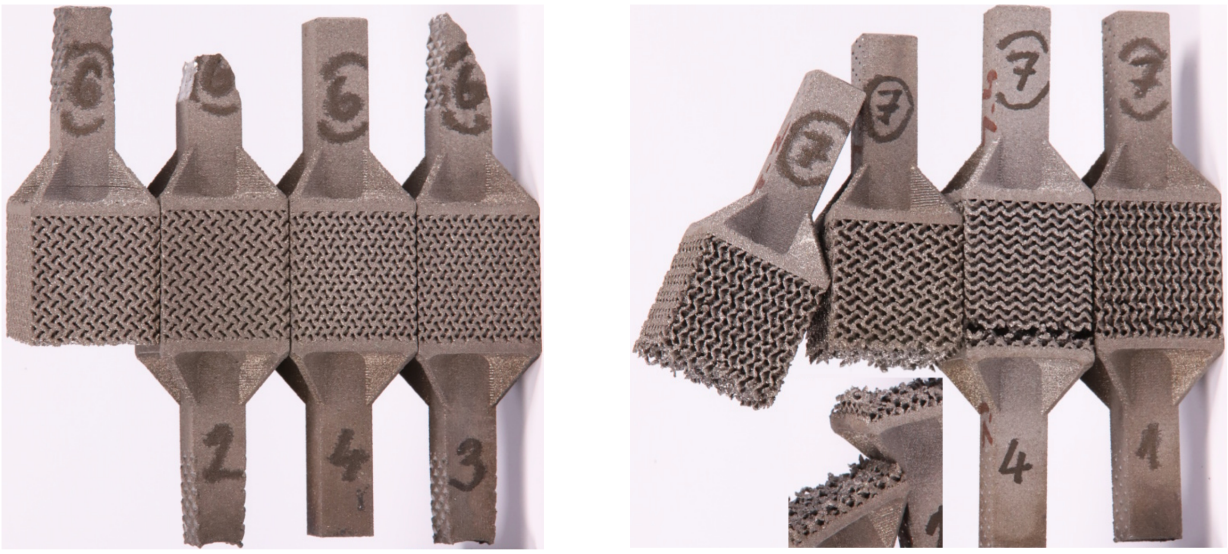

A

B

Figure 26: Defective gyroid tensile test specimens. Their brittle fracture and internal defects, which were not initially observable, made the tests unreliable and had to be terminated. The specimens are displayed upside-down from the direction of printing. Image taken from a co-authored work [124].

8.1 Macromechanical Evaluation of Trabecular Structures

8.1.1 Trabecular Specimens and Load

Evaluation of mechanical properties is important for numerical simulations using FEM. Trabecular structures are geometrically so complex that solving their behavior as a whole using the theory of large deformations is exceptionally demanding on computation times. A viable alternative for future analyses might be to homogenize the properties of the structure and use it as a layer of specified properties. For determination of these properties, macromechanical tests were performed on cubic specimens (Figure 19 and 27). These experiments aimed to determine the global elastic modulus of the entire structure. A total of six specimens were used, which differed in cell type (Diamond, Rhombic, Dode Thick) and cell density per edge of the specimen (Figure 28).

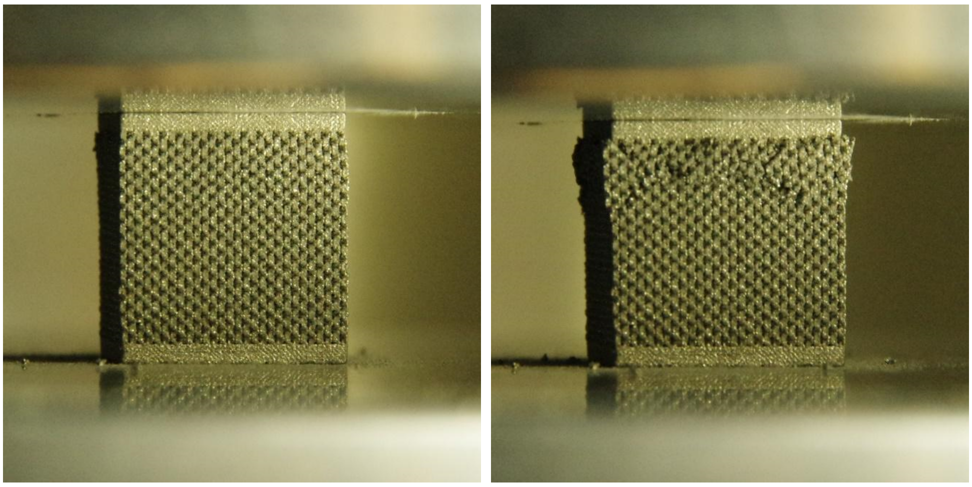

Figure 27: The mechanical loading in the MTS Alliance RT-30 machine: left—loaded structure before the collapse, right—deformed structure during loading [122].

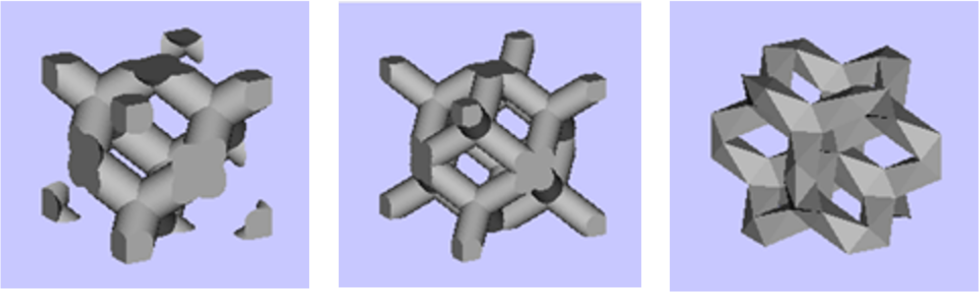

Figure 28: Geometry of BECs of individual specimens: left—Diamond, center—Rhombic, right—Dode Thick. Figure taken from a co-authored published work [124].

The dimensions of the test specimens were 14×14×16 mm. The trabecular part of the specimen had dimensions of 14×14×14 mm, and a 1 mm thick homogeneous slab was designed on the top and bottom parts for load distribution and also as a substitute for supports during 3D printing (this was done so that no supports have to be removed from the specimen after printing). Mechanical tests were performed according to the standard ISO 13314:2011 Mechanical testing of metals — Ductility testing — Compression test for porous and cellular metals [125]. The MTS Alliance RT-30 press located in the laboratories of FCE CTU was used. The material properties were determined from stress-strain curves, which were calculated from input parameters (dependence of deformation on applied force).

8.1.2 Trabecular Macromechanical Results

The resulting global elastic moduli are shown in Table 9. Values of E are significantly lower than those of a homogeneous material, confirming the null hypothesis of the structure. The global moduli approach values close to those of human cancellous bone, and the application of the structure on the stems of implants can, therefore, lead to two positive effects:

- Reduction in stiffness of the whole intraosseous implant system, therefore eliminating stress shielding
- Matching the stiffness of the contact layer between the implant and bone, therefore eliminating singular stress concentrations

The Dode Thick 11.5 and Rhombic 11.5 specimens did not achieve the first local maximum $\sigma_{first,max}$ and proof compressive stress $\sigma_{0.2}$ due to the limits of the testing machine—the specimens were very strong, and the test had to be terminated prematurely.

Table 9: Global elastic moduli of the trabecular structure specimens, n represents porosity. Results also published in a co-authored work [124].

Type of trabecular structure	E [GPa]	$\sigma_{first,max}$ [MPa]	$\sigma_{0.2}$ [MPa]	n —
Diamond 18	2.884	88.649	86.647	0.366
Dode Thick 11.5	2.838	98.211	84.694	0.408
Diamond 14	3.508	141.924	126.449	0.376
Dode Thick 14	3.713	N/A	142.218	0.374
Rhombic 11.5	3.822	N/A	N/A	0.261
Rhombic 9.5	2.631	90.201	78.388	0.493

The relationship between porosity and other parameters is determined by the amount of material (Rematitan) the structure is made from. The more material there is in the structure, the smaller the pores are and, therefore, the higher the global modulus and strength of the structure. Interestingly, the Diamond structure does not precisely replicate this trend as its porosity is second lowest with $n = 0.366$. This fact can be attributed to the beams' layout and the indirect proportion of beam width and cell size.

8.2 Macromechanical Evaluation of Gyroid Structures

8.2.1 Gyroid Specimens and Load

To test the failure behavior of the gyroid structure in compression, single gyroid structure specimens with dimensions of $25.12 \times 25.12 \times 25.12$ mm (circumscribed cube) were made. The models were created in Autodesk NetFabb. To ensure a good load transfer and even distribution of force, homogeneous top and bottom plates with 2 mm thickness were modeled and printed. The models of gyroid structures were created using Equation 3 with a period of 2π. For ease of printing and low cost, the specimens were made of PA12 nylon polymer material using the SLS 3D printer Sinterit Lisa Pro at FCE CTU Prague. Porosity was kept at $n = 0.75$ across all specimens to maintain some level of comparison between different structures (same amount of material per unit cube, different material layout).

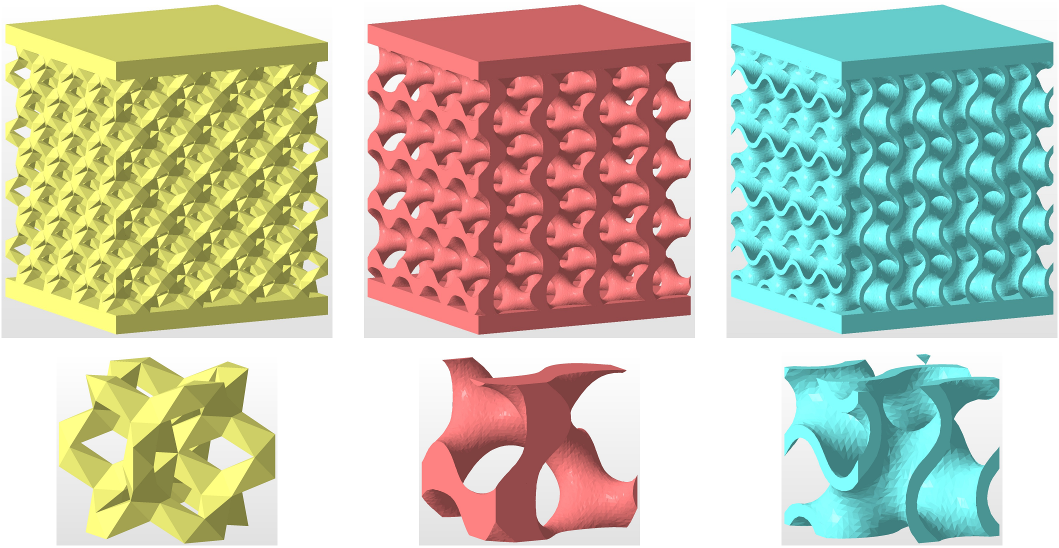

Figure 29: Top row—geometries of models generated using Equation 3 for the purpose of macromechanical tests. Bottom row—basic element cells (BEC). Structures: yellow—Dode-Thick, red—tubular gyroid, blue—sheet gyroid. All of the models were made to have the same porosity $n = 0.75$. Figure taken from my published work [115].

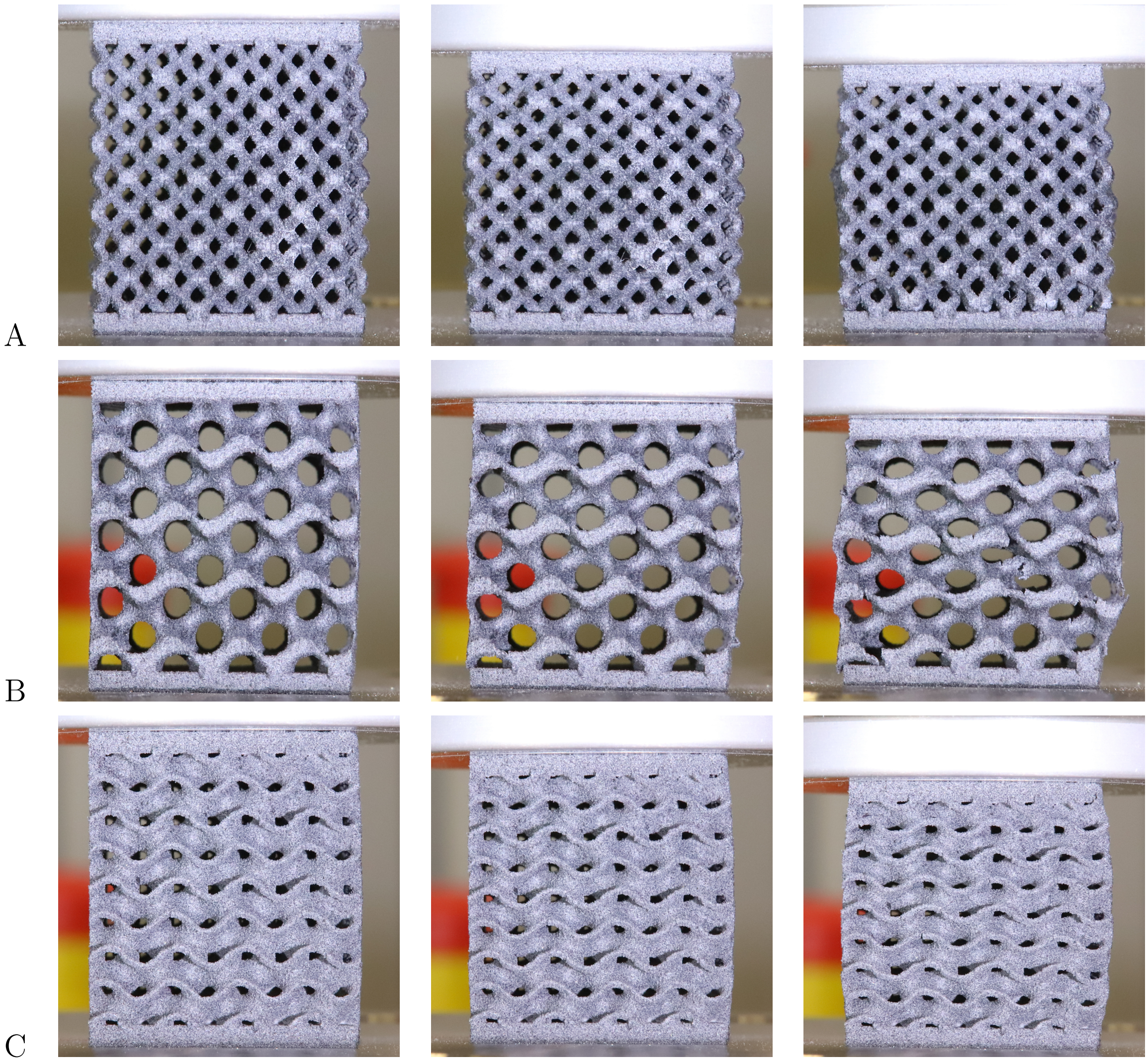

Figure 30: Deformations of specimens during the uniaxial mechanical compression test. Row A—Dode-Thick structure, row B—tubular gyroid, row C—sheet gyroid. The time of taking the pictures is the beginning of the test (first column), ca. 0.5τ (middle column) and the final time at failure τ (last column). Figure taken from my published work [115].

There were 3 tested variants in total:

1. Dode-Thick trabecular structure, porosity $n = 0.75$

2. Single gyroid, sheet variant, porosity $n = 0.75$, wall thickness 0.5 mm, $t = 0$

3. Single gyroid, tubular variant, porosity $n = 0.75$, $t = 0.78$

The models used for 3D printing were created using MSLattice [126]. It is a recent (2020) Matlab-based [127] tool developed by Dr. Oraib Al-Ketan for generation of TPMS published in Journal of Materials Design & Processing Communications. It works with any user-specified equation of a TPMS (e.g. Equation 3). I used this particular tool because it generates better tessellation for numerical analyses and is still usable for .STL file export and 3D printing. After printing, the specimens were processed in an SLS cleaner and checked for defects. Subsequently, they were tested on the pneumatic static press LiTeM. The mode of controlled displacement was used with a load speed of 0.04 mms^{-1}. The models of the structures are shown in Figure 29. The results of the uniaxial compression tests are shown in Figure 30 and in Table 10.

8.2.2 Gyroid Macromechanical Results

The tests were conducted to assess the structures' usefulness in the field of implants, where delamination, local damage, formation of debris and material loss are unacceptable as they pose a risk to the human body in various forms of contamination, inflammation and local immune reactions [128]. In this regard, it is useful to observe the character of the structures' failure, as structures prone to local damage are not acceptable.

The experiment has shown that while maintaining the same material density, the sheet gyroid variant has the highest stiffness and peak compressive stress among all other tested variants. This is true thanks to the sheet variant's wall-like character (elimination of local damage, no stress concentrations, better details without singularities).

As to the character of failure, the sheet variant of the gyroid structure also shows the best results, as the failure is simply a progressive compression of adjacent layers into each other without any loss of stability or any disconnections. If we look at Figure 30, we can see that the trabecular Dode-Thick structure loses some connections of beams, and the tubular gyroid variant suffers from loss of stability.

Table 10: Values of maximum peak stress σ_{max} and elastic modulus E of tested trabecular and gyroid structures made from the PA12 material [115]. Values of E obtained from linear parts of load curves of specimens according to the updated ISO 13314:2011 standard [125].

Structure type	σ_{max} [MPa]	E [MPa]
Dode-Thick	1.69 ± 0.25	27.30 ± 3.81
Tubular gyroid	1.75 ± 0.11	28.74 ± 1.80
Sheet gyroid	4.43 ± 0.47	72.43 ± 6.13

Another factor that weighs in on this experiment is the quality of the specimens. As discussed in Chapter 7.3.1, the trabecular structure suffers from manufacturability issues as its sharp edges, rapid changes of curvature and shape and other factors negatively influence the quality of the specimens (and by extension potentially the functional implant), degrading the structure's mechanical properties and bringing a level of uncertainty. On the other hand, the gyroid structures with fluent changes of geometry and curvature seem to have no problem in this regard.

9 Numerical Simulations

There were 2 general types of QCT/FEA simulations performed—the main CT simulation with the gyroid and threaded implants and supplementary X-ray simulations with an All-on-4 system. Subsections of Chapter 9.3 describe the main simulations with CT data, X-ray simulations follow in Chapter 9.4.

All simulations and modeling tasks mentioned below were performed on a 2020 personal computer equipped with an 8-core, 16-thread 4.7 GHz processor and 64 GB of DDR4 3200 MHz RAM and without the use of a graphics card for additional processing power.

9.1 Tessellation Quality

Usually, when a user wants to create a 3D-printed product, they take the time to prepare their model in CAD software, export an .STL file of their geometry and begin preparations for printing. While this is fine with the process of 3D printing itself, conventional CAD-generated tessellation is not usable for FEM simulations. Multitudes of errors in geometry of the output surface can emerge, making the CAD-generated tessellation unusable. While CAD software usually has means to adopt TPMS or structures (for 3D printing), the division of the output surface into triangles leaves a lot to be desired with a lot of intersecting surfaces, isolated or disconnected nodes and other defects that make finite element analysis (FEA) and mesh generation virtually impossible. This is clearly demonstrated in Figure 31. Therefore, modeling with Equation 3 in MSLattice [126] (implicit function modeling) had to be adopted for FEA. Notably, the traditional CAD process is not inferior but quite handy when used as an infill tool for the sole purpose of 3D printing, where tessellation does not require the geometry to be so precise.

Mesh sensitivity and element types are also worthy of consideration. Authors Peng and Tran [129] describe that by using shell elements, they were able to reduce computation times by a factor of 200 (70 minutes for tetrahedral elements down to ca. 20 seconds for shell elements). Although the agreement between the results for both simulations is good, I am skeptical as the tetrahedral elements used were second-order, 10-node elements, and the mesh was much finer compared to the shells. Furthermore, using shell elements is unreliable when porosity decreases as wall thickness increases, and the out-of-plane normal and shear stresses cannot be neglected any longer [130]. However, these studies bring the topic of mesh sensitivity to attention and call for a mesh sensitivity study on gyroid BECs with tetrahedral first-order elements with varying coarseness.

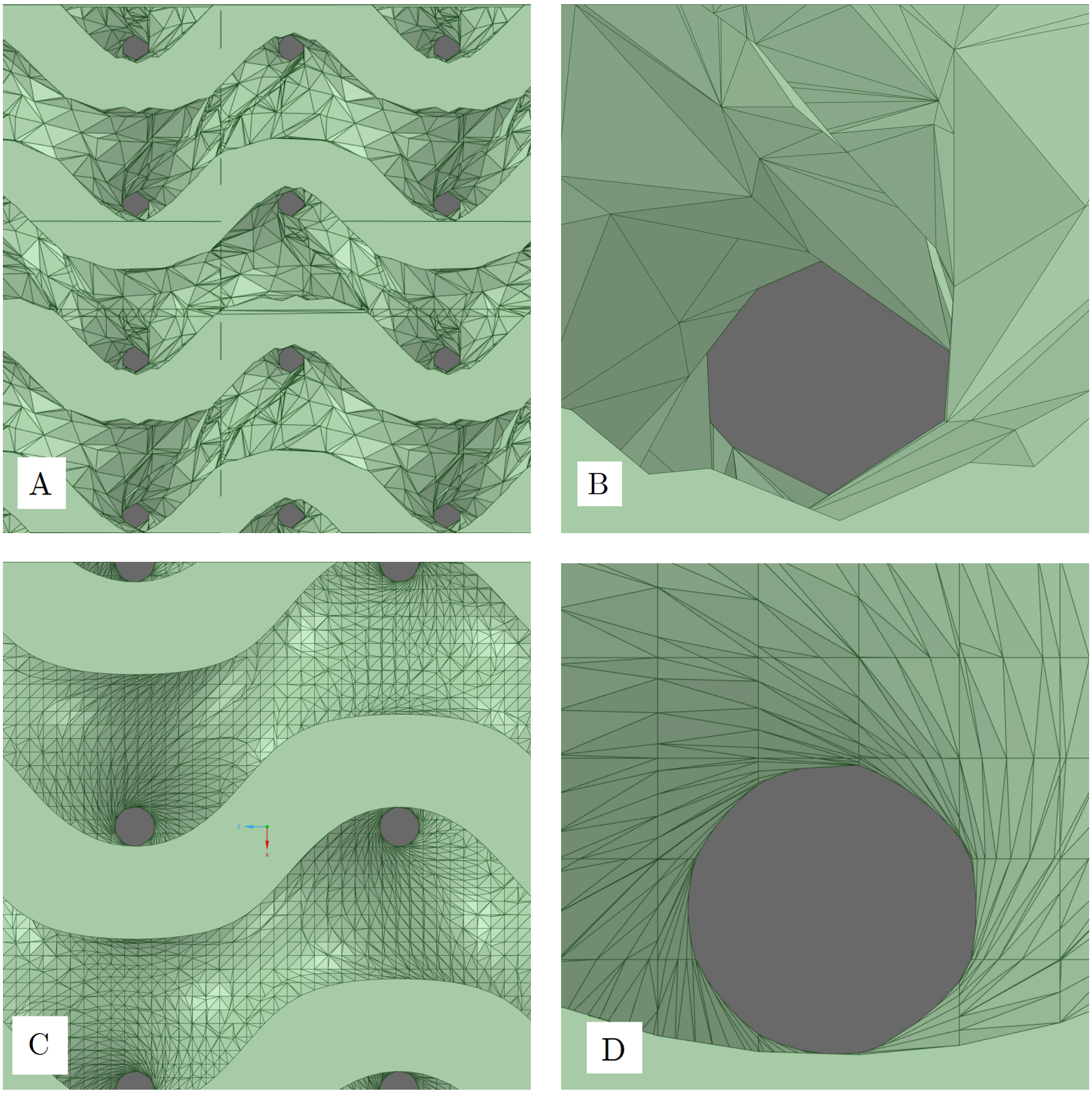

Figure 31: Demonstration of flaws, intersecting small faces, geometry errors and overall bad tessellation on gyroid structures generated in a CAD environment (A, B). C and D show good tessellation achievable with direct modeling via Equation 3 in MSLattice [126]. The CAD approach (A, B) is sufficient for 3D printing but not for a mesh for FEM. Variants C and D have good enough geometrical precision for FEM. The coarseness of tessellation (division of the surface domain into triangles) on C and D can be chosen arbitrarily. Figure taken from my published work [115].

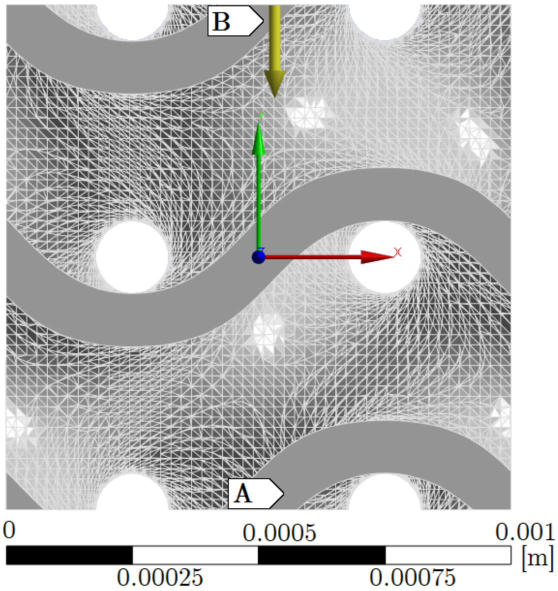

Figure 32: The single gyroid structure model that was used for the mesh sensitivity study. The model is a BEC with an edge length of 1 mm and varying mesh sizes. The figure does not show the mesh but rather the triangular surface facets. Bottom (A) is fixed in all directions while top (B) is incrementally loaded by displacement up to 0.05 mm.

9.2 Mesh

9.2.1 Mesh Sensitivity Study

To properly assess the findings of Chapter 9.2 and 6.3, a mesh sensitivity study was performed to find out the response of a basic single gyroid model to changes in element sizes. The BEC model with porosity $n = 0.7$ was generated using MSLattice, imported into ANSYS SpaceClaim [131] and analyzed in ANSYS Workbench [132]. The model is described in Figure 32. The tessellation of the geometry model (the .STL file) was made with 50 divisions in the direction of each axis. To assess mesh sensitivity, the analysis considered non-linear material behavior with bilinear hardening and without softening.

9.2.2 Mesh Elements

In the final simulations, two types of elements were used. Four-node solid, first-order elements were used for the inside areas of bone and implant parts, and three-node shell elements were used for outer areas where thin cortical bone surrounds the cancellous bone.

Four Node Solid Elements have displacement degrees of freedom U_x, U_y, U_z, stress components σ_x, σ_y, σ_z, τ_{xy}, τ_{yz}, τ_{zx} and strain components ε_x, $\varepsilon_y, \varepsilon_z, \gamma_{xy}$, γ_{yz}, γ_{zx}. The strain inside the element is constant. The elements have four integration points.

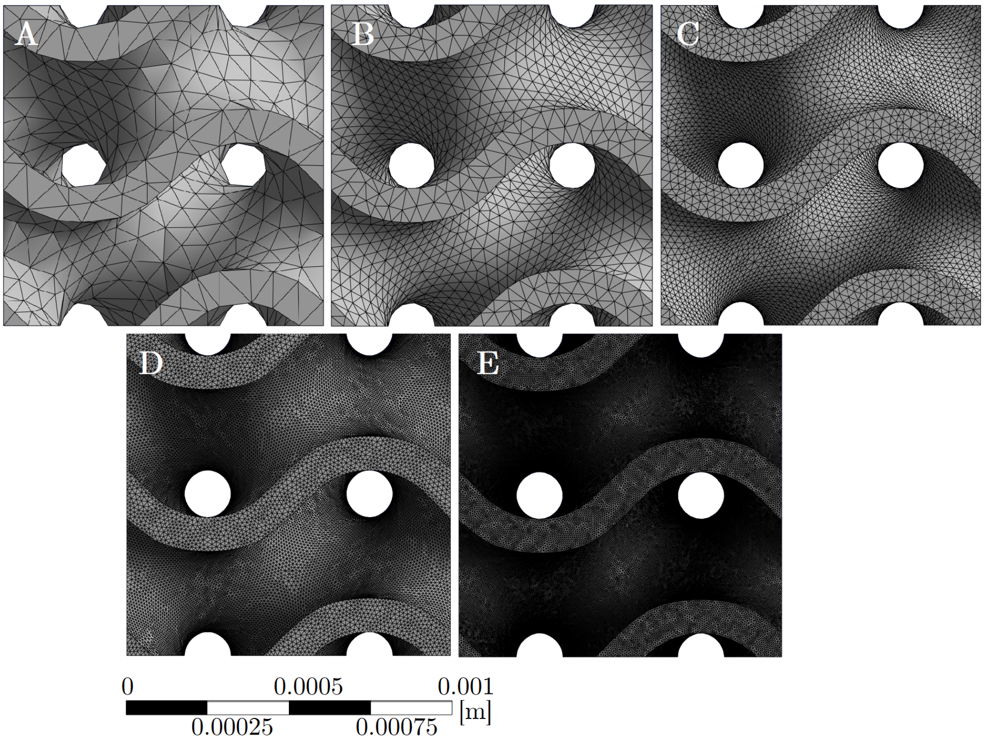

Figure 33: Five different mesh sizes used for the sensitivity study. Average element sizes, counts and solution times: A) $5 \cdot 10^{-4}$ m, 4 703 elements, 4 s; B) $5{\cdot}10^{-5}$ m, 33 713 elements, 25 s; C) $2.5 \cdot 10^{-5}$ m, 268 181 elements, 3:33 min; D) $1.125 \cdot 10^{-5}$ m, 1 382 656 elements, 24:28 min; E) $6.75 \cdot 10^{-6}$ m, 6 246 314 elements, 4:26:34 h. Tetrahedral elements are linear.

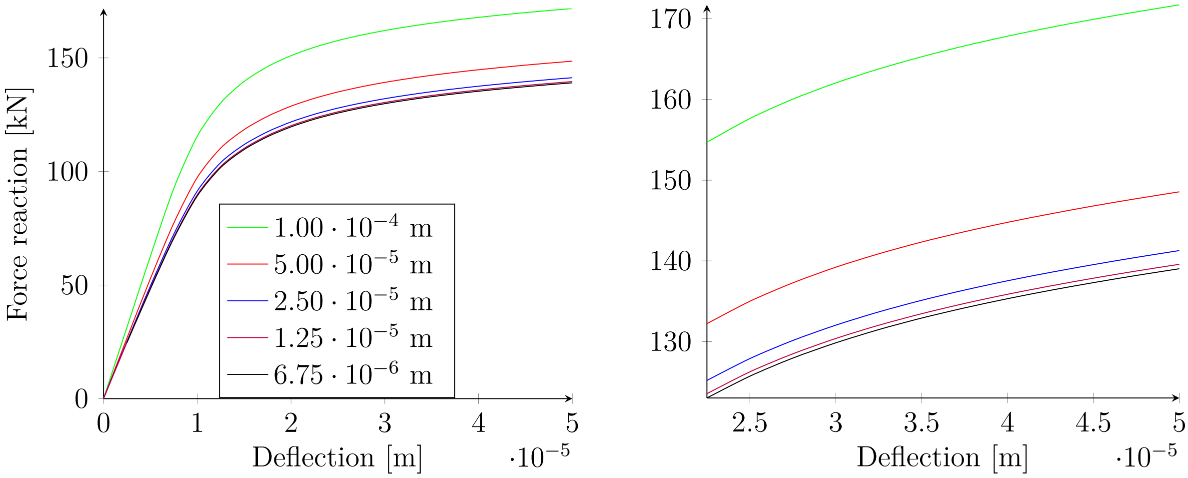

Figure 34: Results of the mesh sensitivity study on a single gyroid BEC. The brief study shows that results in close agreement with finer meshes can be obtained by using element size of $2.5 \cdot 10^{-5}$ m, or $\frac{1}{40}$ of the BEC's edge length, or 4 elements per wall width. However, QCT/FEA simulations proved that this fine mesh cannot be worked with in real time, so the final size was set to 2 elements per wall width (red), where the response is ca. 8% stiffer compared to the finest mesh. Left—the whole diagram, right—a zoomed-in area of interest.

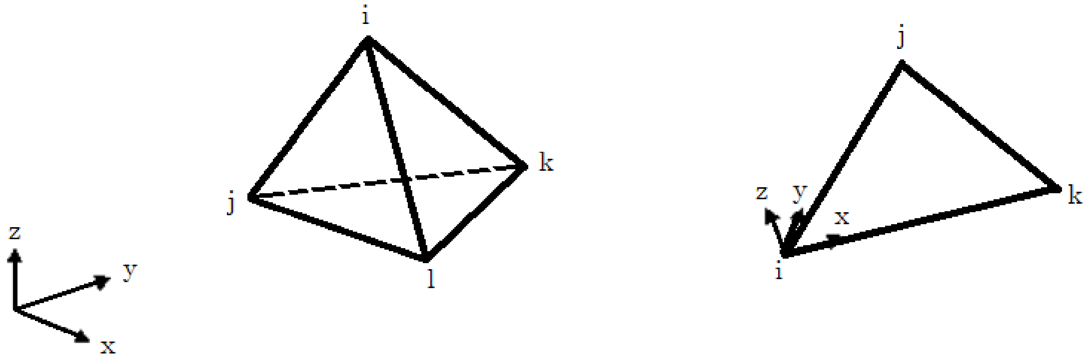

Figure 35: Left—Four node solid first-order tetrahedral elements used for the inside areas of bone. Right—Layered three-node shell element for thin areas of cortical bone. In some cases, the cortical bone is so thin that the edge length of a single element exceeds it. Therefore, the shell approach is a good way to represent the thin areas of cortical bone without needlessly inflating the model with fine elements.

Three Node Shell Elements have displacement degrees of freedom U_x, U_y, U_z, θ_x, θ_y, θ_z, stress components σ_x, σ_y, τ_{xy} and strain components ε_x, $\varepsilon_y, \varepsilon_z, \gamma_{xy}$. The shell elements have three layers. Stress and strain are calculated in each layer. The node displacement degree of freedom is five.

Conveniently, the Mechanical Finder v12 software [133], in which the bone-implant interaction is analyzed in Chapter 9.3, uses both ANSYS ICEM CFD [134] for generation of tetrahedral elements and the fTet Wild [135] meshing algorithms. Hence, the mesh sensitivity study remains relevant even if another software is used.

The implant insertion was performed by manually inserting the implant as an .STL file and securing its right location via a guided process of translation and rotation with the aid of displaying the adjacent CT data, as illustrated in Figure 36. Afterwards, mesh element sizes and properties are specified and the implant is subtracted from the surrounding bone tissue by Boolean operations. Then, the interface can either be defined to be bonded, or contact conditions between the implant and bone can be specified. The contact conditions that show one of the analyzed implant variants inserted in the bone of a reconstructed human mandible are shown in Figure 37 and introduce the subject of the next chapter.

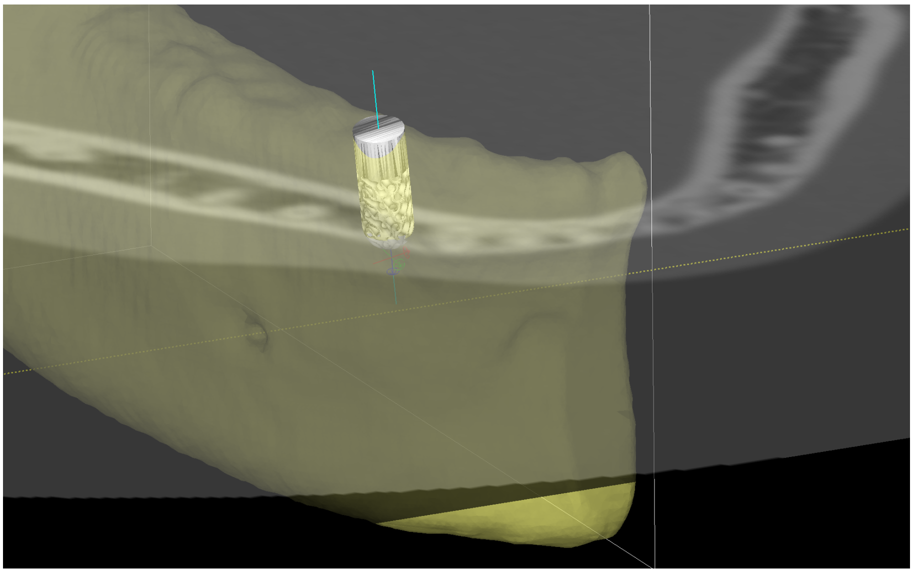

Figure 36: Position of the implant in a cutout of the reconstructed model of the human mandible. If needed, the final position can be checked against the CT data for location precision. The position was chosen to be in place of the first mandibular premolar tooth according to the common placement of an implant of these dimensions.

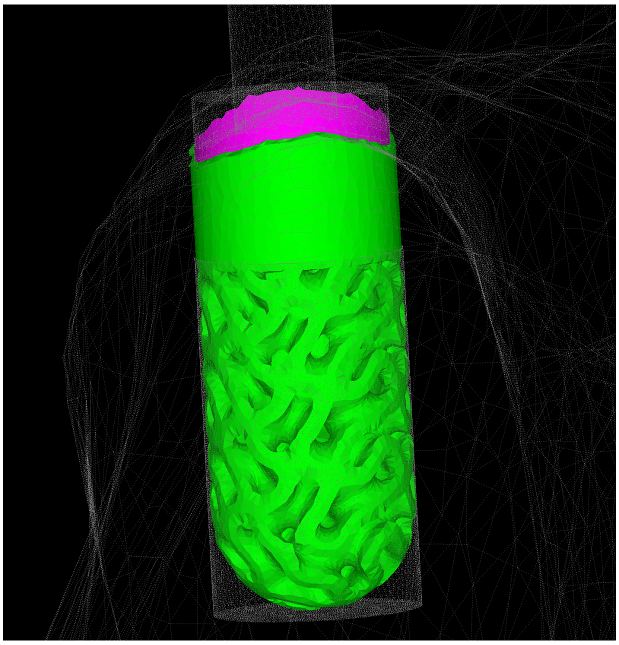

Figure 37: Mesh and contact settings between the gyroid implant (master nodes, purple) and surrounding bone of a CT-reconstructed human mandible (slave nodes, green). Grey lines represent mesh elements on the surface. Note that the mesh is refined in the area surrounding the implant (cylindrical region). Here, the mesh size for both bone and implant is 0.1 mm, but in the anterior and posterior regions of the mandible, the mesh of bone is more coarse at 2 mm per element. The homogeneous parts of the implant have a mesh size of 0.2 mm. The load-transferring member has a mesh size of 0.3 mm.

9.3 CT Numerical Model

The CT simulations aimed to compare two variants of dental implants with the same bounding box (or outer dimensions) but a different geometry in a reconstructed model of the human mandible (lower jaw). These two variants are the gyroid-equipped implant and the conventional, threaded implant. The first of the two variants was analyzed using two different numerical models—a geometry-true gyroid model and a homogenized model (same geometry, only the porous part is modeled as a homogeneous layer with specified properties). The conventional, threaded implant is a common dental implant with a slight taper that is screwed into the bone. The values for the homogenized variant are derived from my co-authored paper [124], where a single sheet gyroid structure with the same porosity has modulus $E = 1.24$ GPa and proof compressive stress $\sigma_{0.2} = \sigma_y = 30.95$ MPa. The simulations can serve as a means of custom-tailoring the porous structure to meet specific needs of the patient.

9.3.1 Geometry Model

The software chosen for modeling of the 3D geometry was a combination of MSLattice [126] and Ansys Spaceclaim [131]. The former was used to generate the geometry of the gyroid structures by using the approach described in Chapter 6.3, namely Equation 3. Then, the gyroid structure was imported into the Ansys environment, and individual dental implant models were created. The geometries of the true gyroid and the homogenized gyroid variants are shown in Figure 38. Additionally, a third simulation of a common, threaded homogeneous implant was performed to compare against the normal and homogenized gyroid implant models.

The geometry of the gyroid implant is in agreement with the findings presented in Chapter 2.2, where the optimal pore size was concluded to be—based on the researched literature—600 µm (or 0.6 mm). The following important structural measurement, wall thickness (200 µm), is basically determined from the constraints of the SLS machine. I have previous experience with 3D-printed metal gyroid and other porous (trabecular) implants and specimens as principal investigator of a TAČR ZÉTA project (TJ01000328) and an investigator of an MPO ”Partnerství znalostního transferu” project (OP PIK CZ.01.1.02/0.0/0.0/17_102/0011518) and I had the opportunity to evaluate the specimens together with my tutor, Mr. Aleš Jíra. As we approach wall thickness below 200 µm, the SLS machine can no longer maintain precise powder fusion and discontinuities and clumps of metal start to occur. Therefore, 200 µm was set as a safe, conservative minimum. There is very little space and thickness remaining around the inner core of a dental implant, and going much over 200 µm—the opposite direction—is not feasible either. This is true for

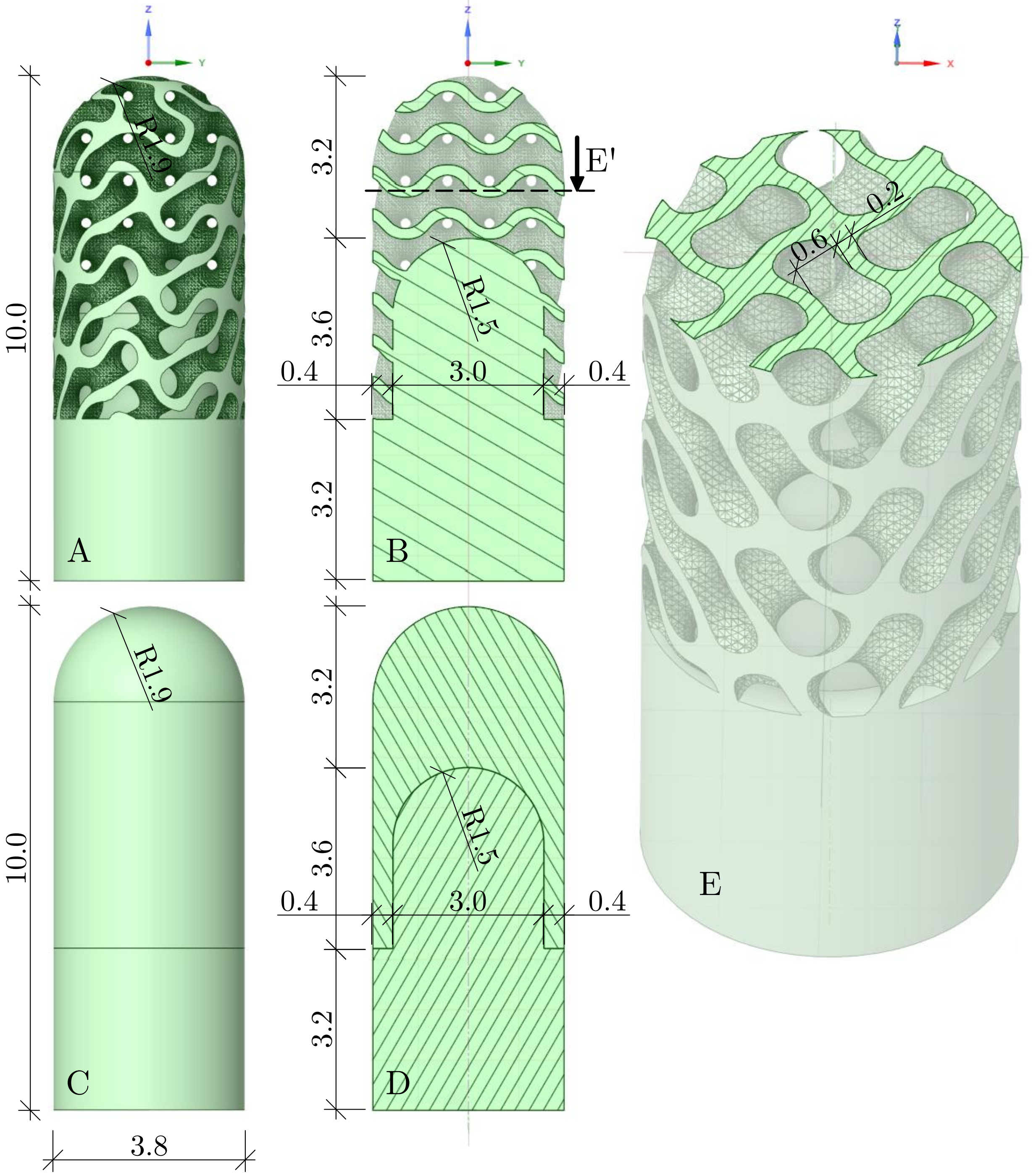

Figure 38: Geometries of the first tested implant variant. Pictures A, B and E represent different views of the gyroid implant model. Pictures C and D represent the homogenized model with mechanical properties of the gyroid structure from [124] (E = 1.24 GPa and $\sigma_{0.2} = \sigma_y$ = 30.95 MPa). All measurements are in mm.

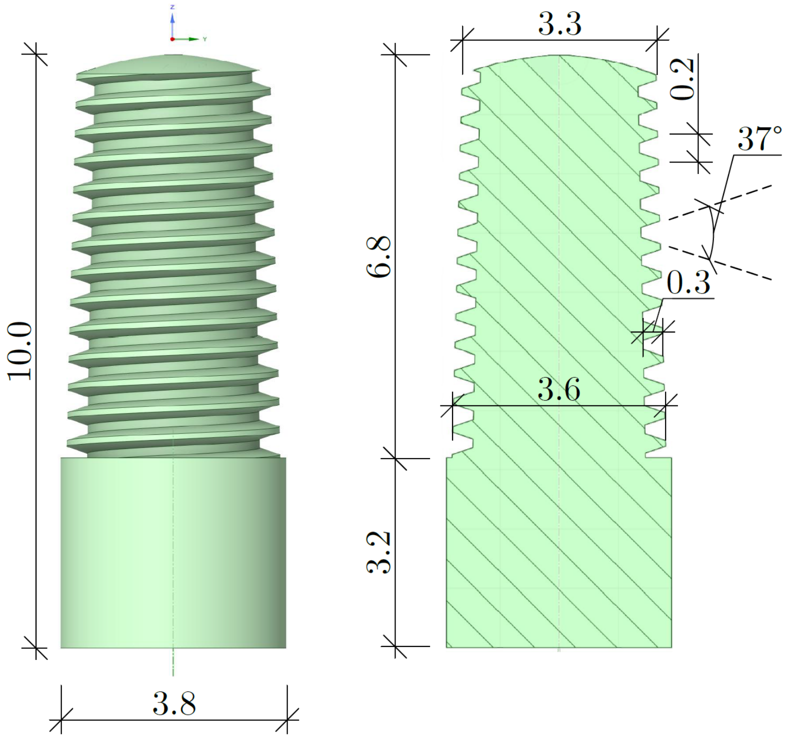

Figure 39: Control geometry. This implant would be conventionally machined and then screwed into the bone. All measurements are in mm. The outer dimensions are identical to the first two variants in Figure 38.

the implants in the frontal section of the human dentition, which are much thinner than implants replacing molars.

9.3.2 Implant Material Model

The two materials modeled in this work are bone and metal. Let us begin with the material model for the metal parts—the Ti-6Al-4V alloy—as it is much simpler and more conventionally used in other software.

The Ti-6Al-4V material is modeled as a ductile material whose yielding is described by the von Mises yield criterion that basically specifies the distance from the hydrostatic axis and is not pressure-dependent:

$$\sigma_{vM} = \frac{\sigma_y}{\sqrt{3}} = \sqrt{J_2} \tag{6}$$

where σ_{vM} is the von Mises stress criterion that is set equal to σ_y, the yield stress. Component J_2 is the second invariant of the deviatoric part of Cauchy stress, which the Cauchy stress tensor components can substitute as shown in Equation 7.

$$\begin{aligned} \sigma_{vM} &= \frac{1}{6} \cdot \left[(\sigma_1 - \sigma_2)^2 + (\sigma_2 - \sigma_3)^2 + (\sigma_3 - \sigma_1)^2 \right] = \\ &= \sqrt{\frac{1}{2} \cdot \left((\sigma_{11} - \sigma_{22})^2 + (\sigma_{22} - \sigma_{33})^2 + (\sigma_{33} - \sigma_{11})^2 + 6 \cdot (\sigma_{12}^2 + \sigma_{23}^2 + \sigma_{31}^2) \right)} \end{aligned} \tag{7}$$

where the Cauchy stress components σ_{ii} are in the direction normal to the plane—normal stresses—and σ_{ij} are perpendicular to the plane—shear stresses—and can be described in three dimensions on a cubic element as shown in Figure 40. The equation for the von Mises yield criterion implies that it is independent of hydrostatic stresses. The material properties assigned to the Ti-6Al-4V material are listed in Table 11.

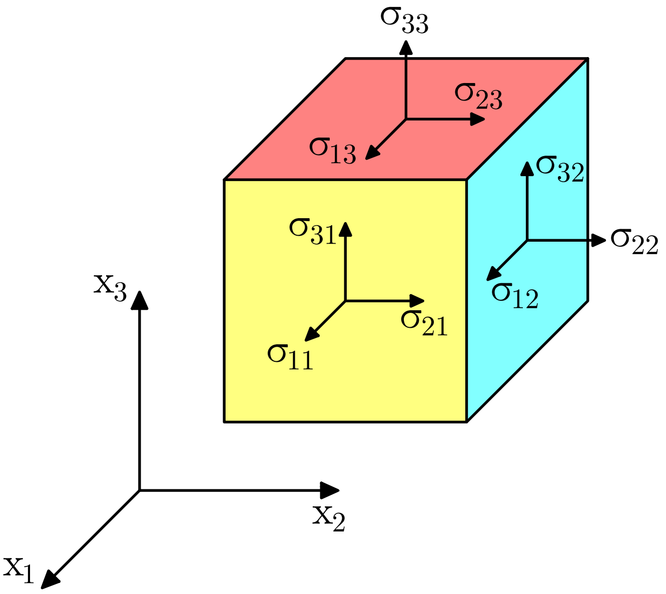

Figure 40: The Cauchy stress components used in Equation 7 that are used in the Cauchy stress tensor.

9.3.3 QCT/FEA Reconstruction and Bone Material Model

Quantitative computed tomography-based finite element analysis (QCT/FEA) is a noninvasive method used to reconstruct image slices into a 3D model that can be used to evaluate stresses and other important quantities. The software used for the numerical analyses was Mechanical Finder (MECHANICAL FINDER v12, Research Center for Computational Mechanics, Osaka, Japan) [133]. It is a QCT/FEA software that uses patient-specific CT data using a Phantom-calibrated CT scan to obtain specific results. This way, every pixel in the extracted range of interest (ROI) is assigned an individual value of the Hounsfield

Table 11: Material properties of the model used for the Ti-6Al-4V implant material.

Material Property	Value	Unit
Young's Modulus	108.854	GPa
Density	4430	kgm^{-3}
Yield Stress	824.74	MPa
Critical Stress	899.27	MPa
Stress Relaxation	0.1	—
Crush Strain	10000	$\times 10^{-6}$

unit. Therefore, the final reconstruction of the bone has an individual value for every voxel (and then every element), making the model completely *inhomogeneous*. This is a significant step up from former modeling methods, where bone was usually represented as a two-phase solid (cortical and cancellous bone). This way, we can have a completely inhomogeneous matrix of stiffness. The values of the Hounsfield unit scale (HU) are calculated from the following equation:

$$HU = 1000 \times \frac{\mu_{tissue} - \mu_{water}}{\mu_{water} - \mu_{air}} \tag{8}$$

where μ_{water} is the value of water and is assigned arbitrarily as 0 HU and the value of air is $\mu_{air} = -1000$ HU and other values are calculated [136].

The QCT/FEA method implemented in Mechanical Finder uses a fully inhomogeneous patient-specific material for bone tissue with each element having individual stiffness k_i that is governed by an equation proposed by Keyak [137]:

$$\rho\ [\mathrm{mgcm}^{-3}] = \mathrm{CT\ value\ [HU]} \times a + b \tag{9}$$

where symbol ρ represents material density and $\rho \geq 0$. The calibration phantom then determines the values of parameters a and b based on known values of densities of calibration rods. It is, therefore, important to provide the CT with the phantom calibration device if the user wants to have a reference point for the HU values. The analysis can still be carried out even without the phantom. However, the user will only know the relations between values of the scan without an external reference, so they will have to assign a reference value themselves, which might negatively affect the analysis outcome. The calculation of Young's modulus is then performed according to Table 12.

Table 12: The conversion equations for varying densities (calculated from Equation 9) to values of Young's modulus E. Settings are based on Keyak [137].

Density ρ [gcm^{-3}]	Young's Modulus E [MPa]
0	0.001
$0 < \rho \leq 0.27$	$33900\rho^{2.20}$
$0.27 < \rho < 0.60$	$5307\rho + 469$
$0.60 \leq \rho$	$10200\rho^{2.01}$

After Young's moduli are determined, we also have to pay attention to the calculation of yield stresses, as shown in Table 13.

Table 13: The conversion equations for varying densities (calculated from Equation 9) to values of yield stress σ_y. Settings are based on Keyak [137].

Density ρ [gcm^{-3}]	Yield Stress σ_y [MPa]
$\rho \leq 0.200$	$1.0 \cdot 10^{20}$
$0.200 < \rho < 0.317$	$137\rho^{1.88}$
$0.317 \leq \rho$	$114\rho^{1.72}$

Therefore, elements which have a density of less than 0.2 gcm^{-3} are effectively set as elastic by specifying a large number for yield stress σ_y.

Yielding of bone material is described by the Drucker-Prager yield criterion, first developed for soils and rocks [138] and subsequently modified multiple times and used for different materials like concrete, bone and other materials [139]. It represents a generalization of the Mohr-Coulomb criterion and can be expressed in the following equation:

$$\sqrt{J_2} = \lambda I_1 + \kappa \tag{10}$$

where λ and κ represent material constants and J_2 is again the second invariant of the deviatoric part of the Cauchy stress and I_1 is the first invariant of the Cauchy stress:

$$\begin{aligned} I_1 &= \sigma_1 + \sigma_2 + \sigma_3 \\ J_2 &= \frac{1}{6} \cdot \left[(\sigma_1 - \sigma_2)^2 + (\sigma_2 - \sigma_3)^2 + (\sigma_3 - \sigma_1)^2 \right] \end{aligned} \tag{11}$$

where σ_1, σ_2 and σ_3 are the three principal stresses. Therefore, if we combine Equation 10 and 11, we obtain Equation 12.

$$\sqrt{\frac{1}{6}\cdot\left[(\sigma_1-\sigma_2)^2+(\sigma_2-\sigma_3)^2+(\sigma_3-\sigma_1)^2\right]}=\lambda(\sigma_1+\sigma_2+\sigma_3)+\kappa \tag{12}$$

therefore, we can see that if $\lambda = 0$ and $\kappa = \frac{\sigma_y}{\sqrt{3}}$, then we receive the previously mentioned von Mises failure criterion (Equation 6 and 7). The Drucker-Prager criterion could, therefore, be said to be an extension of the von Mises criterion. The main advantage of the Drucker-Prager yield criterion lies in being able to capture the behavior of materials with different tensile and compressive yield strengths, such as bone or concrete. Among many interpretations for different materials, we could obtain λ and κ in their simplest forms by performing uniaxial tensile and compression tests of the modeled material. Obtaining κ and λ from experiments can be done by evaluating uniaxial tensile and compressive tests of the material and determining values of yield compressive stress σ_c and yield tensile stress σ_t. If σ_c is the uniaxial compressive yield stress, then Equation 12 provides:

$$\frac{1}{\sqrt{3}}\sigma_c=\kappa-\lambda\sigma_c \tag{13}$$

and if σ_t is the uniaxial tensile yield stress, then the following is provided:

$$\frac{1}{\sqrt{3}}\sigma_t=\kappa+\lambda\sigma_t \tag{14}$$

Next, we can solve the above system of equations to receive the following expressions:

$$\kappa=\frac{2}{\sqrt{3}}\left(\frac{\sigma_c\sigma_t}{\sigma_c+\sigma_t}\right);\quad \lambda=\frac{1}{\sqrt{3}}\left(\frac{\sigma_t-\sigma_c}{\sigma_t+\sigma_c}\right); \tag{15}$$

After solving for κ and λ, we can plot the Drucker-Prager and also the von Mises yield surfaces in the $\sigma_1,\ \sigma_2,\ \sigma_3$ stress space, as shown in Figure 41.

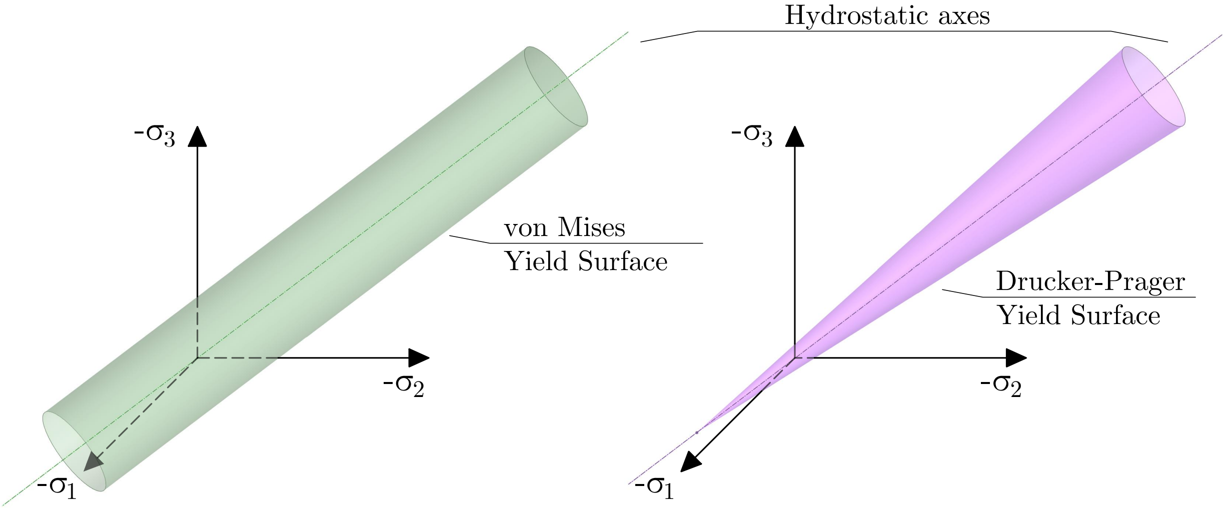

Figure 41: Left—the von Mises yield surface, right—the Drucker-Prager Yield surface. The former is used for the implant material, which predicts that yielding is independent of the hydrostatic stress state, while Drucker-Prager is used for bone and is pressure dependent.

After all these conversions are made, the user still has the option to modify other material properties of bone which are not automated by the QCT/FEA conversion process described above in this chapter. The properties which were used are listed in Table 14. In this case, the yield stress σ_y is defined for the compressive direction and the critical stress is defined as $\sigma_{cr} < \sigma_y$ for the tensile direction and if $\sigma_{max} > \sigma_{cr}$, a crack perpendicular to the direction of principal stress occurs.

Table 14: Material properties of bone which can be changed and either are or are not automated by the QCT/FEA processes. The process of automation (making the inhomogeneous material) is shown in Tables 13 and 12.

Property	Value	Unit
Young's Modulus	Automated	[MPa]
Poisson's Ratio	0.4	—
Critical Stress	$0.8\sigma_y$	[MPa]
Yield Stress	Automated	[MPa]
Stress relax.	0.05	—
Density	Automated	[gcm^{-3}]
Crush Strain	3000	$\times 10^{-6}$

The process of CT reconstruction and creating a FEM model is shortly described on a workflow chart in Figure 42.

Table 15: CT conditions of patient's exposure and CT parameters.

X-ray Tube Voltage	120 kVp
Irradiation Time	925 ms
X-ray Tube Current	80 mA
Irradiation Dose	2090 mAs
CT Power	9600 kW
No. of Slices	414
Pixel Size	0.488281×0.488281 mm

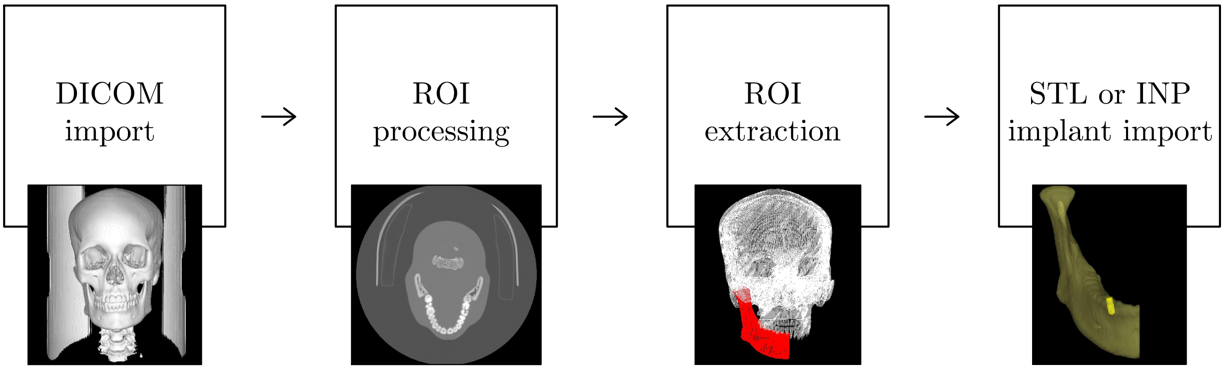

Figure 42: Illustration of QCT/FEA workflow for geometry preparation. For most cases, the second step (ROI processing) will be the most time-consuming.

The precision of the geometry depends on the quality of the DICOM (Digital Imaging and Communications in Medicine) data imported. The quality of the resolution depends on tube current, voltage and exposure time. The patient's data is anonymous, but CT machine parameters are listed in Table 15. Phantom-calibrated, anonymized CT data is extremely difficult for a researcher to find and is usually only available to the patient and the physician to work with on the condition of the patient's consent. I would like to acknowledge and thank for the help of Mr. Hideyuki Mimata from RCCM with provision of clinical data. ROI processing involves a combination of manual and automated operations that add or subtract material or noise from the CT slice and can be a time-consuming process if the model is large or has a lot of unwanted noise. A typical workflow is illustrated in Figure 43.

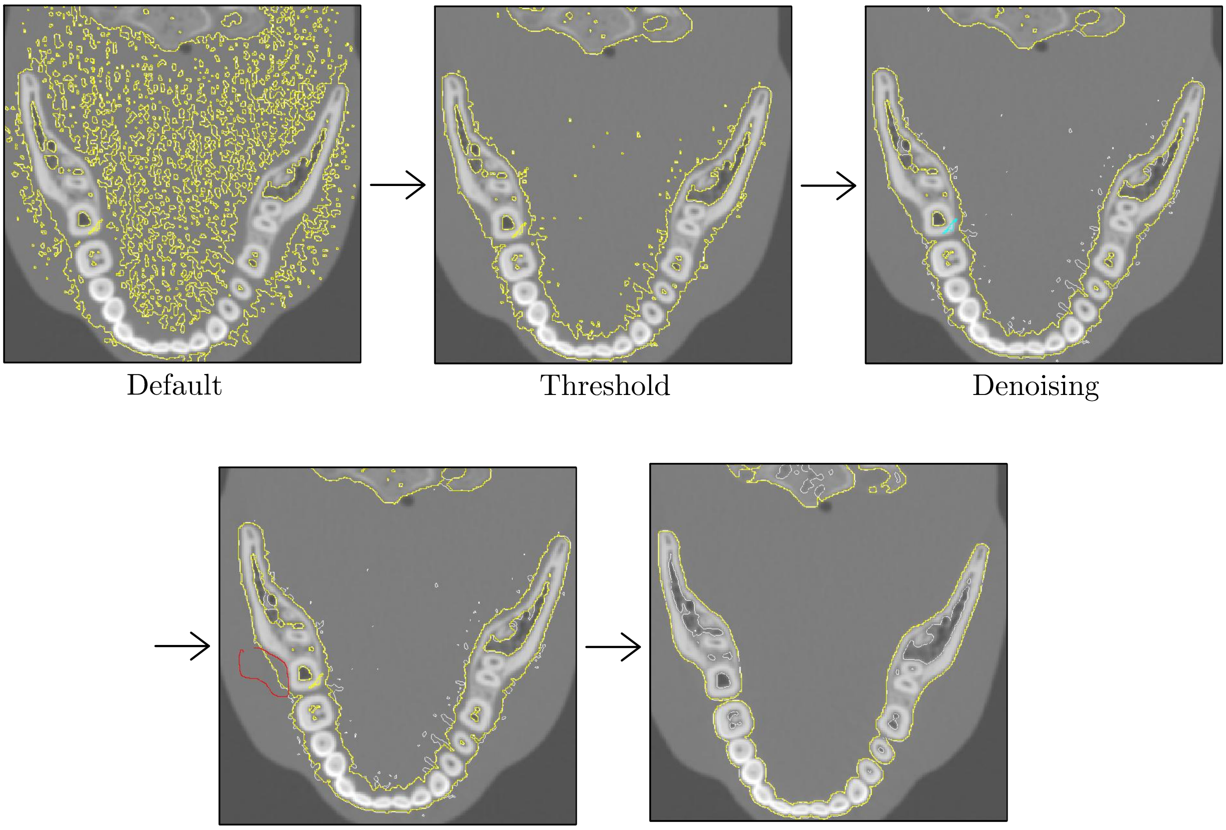

Default

Threshold

Denoising

Manual Operations

Filling, Clean Slice

Figure 43: Range of Interest (ROI) reconstruction workflow. These operations must be performed on each slice (of which there can be hundreds), or ca. each third or fourth slice and interpolate the geometry in between. Also, transparent operations (operations on an arbitrarily large number of slices) are available to the user. This process is usually the most time-consuming part of preparing a QCT/FEA model and has to be performed carefully. The first picture shows a typical default state. Then, a threshold for the Hounsfield unit (Equation 8) is set and through denoising, enclosing gaps, manual drawing and other processes, the slice is prepared. This workflow refers to the second step in Figure 42. This skull model is 400 slices total, of which ca. 180 had to be reconstructed.

This particular human skull CT scan that was used in the thesis was taken on a healthy person who had their entire dentition intact. I recognize that an edentulous lower jaw that had proper time to heal before implant insertion would be the best for this simulation (provided that new bone material formed), but almost impossible to come by, considering confidentiality and the requirement for Phantom calibration. Therefore, this available high-resolution model with teeth was used, and an upper threshold for the HU value of the teeth roots inside the mandible was specified. This way, satisfactory results can still be obtained. The map of Young's moduli on a working section of the reconstructed model is shown in Figure 44.

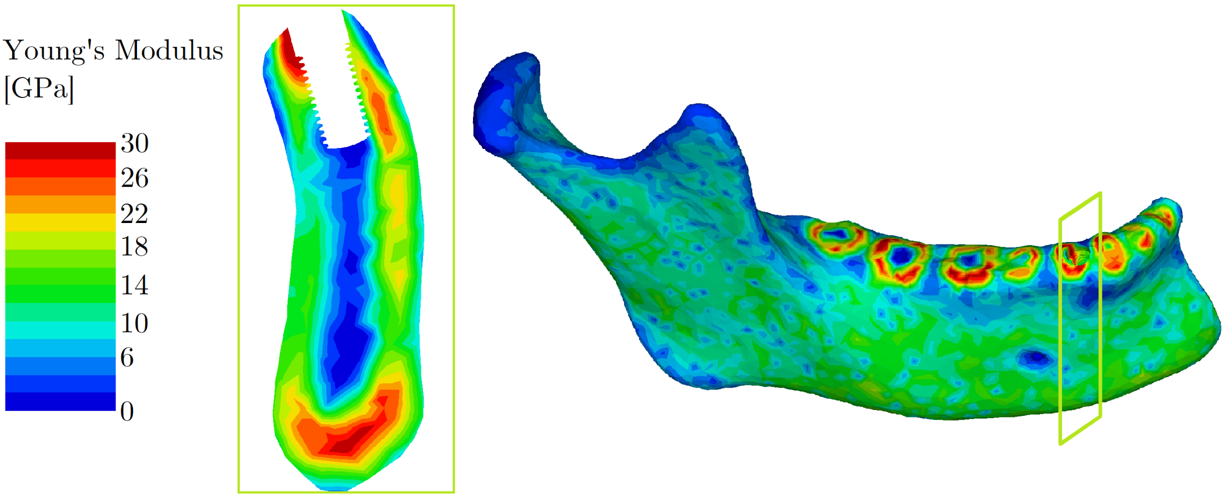

Figure 44: Map of Young’s Moduli from the final reconstruction of the mandible shown on a working section (left) and on the whole half of the mandible (right)—as will be discussed in Chapter 9.3.5, it is modeled as a symmetric half. The detailed section is highlighted in light green color. The figure shows bone with the threaded implant variant inserted. The maximum value for Young’s modulus for acceptable results was set to 30 GPa because there are still tooth roots present in the mandible (and their modulus would be higher). The CT scan of the mandible that was available was not one of an edentulous patient but of a patient who still had their teeth. The choice to make the upper limit at 30 GPa was made because there are still some parts of the mandible that have that high modulus (see the bottom part of the section on left). This is, of course, only a necessary compromise, and a model of an edentulous patient with newly grown bone in places where roots were before would be a great improvement.

9.3.4 Solver

The FEM solver variant used for my analyses was the ”Solver V2” version of Mechanical Finder 12.0. It has the option to consider geometric and material non-linearities as well as perform static or dynamic analyses. In this case, at first, the analyses were set to consider large deformations, which later turned out to be redundant. Since the implant and the porous part are largely embedded in bone, the final simulations only considered material nonlinerities and the compressive and tensile failure of elements in static mode.

The FEM analysis uses the displacement method, and the solution procedure using substeps can be formulated as follows:

1. Loading step, setting incremental load $\mathbf{dF}$

2. Individual element stiffness matrix $\mathbf{K_e}$ and global stiffness matrix $\mathbf{K}$ calculation as:

$$\mathbf{K_e} = \int_V \mathbf{B^T D B}\, dv; \quad \mathbf{K} = \sum_{i=1}^{n} \mathbf{K_e} \tag{16}$$

where **B** is the strain-displacement matrix and **D** is the stress-strain matrix

3. Calculation of incremental displacement **dU** from:

$$\mathbf{dF} = \mathbf{KdU} \;\Rightarrow\; \mathbf{dU} = \mathbf{K^{-1}dF} \tag{17}$$

4. Stresses and strains of individual elements are calculated from incremental displacement **dU**:

$$\begin{aligned} \mathbf{d}\boldsymbol{\varepsilon} &= \mathbf{BdU}; \qquad \boldsymbol{\varepsilon}^{\mathbf{n}} = \boldsymbol{\varepsilon}^{\mathbf{n-1}} + \mathbf{d}\boldsymbol{\varepsilon} \\ \mathbf{d}\sigma &= \mathbf{D}\mathbf{d}\boldsymbol{\varepsilon}; \qquad \boldsymbol{\sigma}^{\mathbf{n}} = \boldsymbol{\sigma}^{\mathbf{n-1}} + \mathbf{d}\boldsymbol{\sigma} \end{aligned} \tag{18}$$

5. Judging whether a broken element exists or not—criteria are given by material characteristics specified in Chapters 9.3.2 and 9.3.3. If there are any broken elements, the respective stiffness matrix $\mathbf{K_e}$ is modified, and stress is recalculated using a modified incremental load **dF** reduced down to 10%. If there are no broken elements, the load increment is not modified, and the procedure continues with calculations of inner and unbalanced forces on the global level from element stress:

$$\begin{aligned} \text{Inner force:} \quad \mathbf{F_{in}} &= \sum_{i=1}^{n} \int_V \mathbf{B^T} \boldsymbol{\sigma}^{\mathbf{n}}\, dv \\ \text{Unbalanced force :} \quad \mathbf{R} &= \sum_{i=1}^{n} \Big(\mathbf{dF} - \mathbf{F_{in}} \Big) \end{aligned} \tag{19}$$

6. Unbalanced force is judged, and if unconverged, the loop returns back to Step 2 (Equation 16). If it is converged, the results are output, and the loop continues from the beginning.

Also, different matrices $\mathbf{d}\boldsymbol{\sigma}$ and $\mathbf{d}\boldsymbol{\varepsilon}$ need to be distinguished for different types of elements.

$$\begin{aligned}
&\text{For solid elements:} \quad &&\mathbf{d}\boldsymbol{\sigma}_{\mathbf{solid}} = \left\{\mathbf{d}\boldsymbol{\sigma}_{\mathbf{x}},\ \mathbf{d}\boldsymbol{\sigma}_{\mathbf{y}},\ \mathbf{d}\boldsymbol{\sigma}_{\mathbf{z}},\ \mathbf{d}\boldsymbol{\tau}_{\mathbf{xy}},\ \mathbf{d}\boldsymbol{\tau}_{\mathbf{yz}},\ \mathbf{d}\boldsymbol{\tau}_{\mathbf{zx}}\right\}^{\mathrm{T}} \\
& &&\mathbf{d}\boldsymbol{\varepsilon}_{\mathbf{solid}} = \left\{\mathbf{d}\boldsymbol{\varepsilon}_{\mathbf{x}},\ \mathbf{d}\boldsymbol{\varepsilon}_{\mathbf{y}},\ \mathbf{d}\boldsymbol{\varepsilon}_{\mathbf{z}},\ \mathbf{d}\boldsymbol{\gamma}_{\mathbf{xy}},\ \mathbf{d}\boldsymbol{\gamma}_{\mathbf{yz}},\ \mathbf{d}\boldsymbol{\gamma}_{\mathbf{zx}}\right\}^{\mathrm{T}} \\
&\text{For shell elements:} \quad &&\mathbf{d}\boldsymbol{\sigma}_{\mathbf{shell}} = \left\{\mathbf{d}\boldsymbol{\sigma}_{\mathbf{x}},\ \mathbf{d}\boldsymbol{\sigma}_{\mathbf{y}},\ \mathbf{d}\boldsymbol{\tau}_{\mathbf{xy}}\right\}^{\mathrm{T}} \\
& &&\mathbf{d}\boldsymbol{\varepsilon}_{\mathbf{shell}} = \left\{\mathbf{d}\boldsymbol{\varepsilon}_{\mathbf{x}},\ \mathbf{d}\boldsymbol{\varepsilon}_{\mathbf{y}},\ \mathbf{d}\boldsymbol{\gamma}_{\mathbf{xy}}\right\}^{\mathrm{T}}
\end{aligned} \tag{20}$$

The connection between the solid and shell elements is done by placing the shell elements on the face of the solid on the surface, making them share all nodes of one face of the tetrahedral element.

9.3.5 Boundary Conditions

Biological systems, such as the human jaw, are highly heterogeneous in their mechanical properties and exact locations of muscle insertions. The forces generated by the muscles are also greatly influenced by lifestyle choices and patterns of movement, such as the motions during mastication. Also, the relative position of teeth against each other when both jaws are in contact, i.e. *occlusion* matters to the final direction and magnitude of the forces applied on teeth from the masticatory system [140]. For a frame of reference, authors Raadsheer et al. [141] measured maximal voluntary bite forces to be 545 N for men (group of 58) and 383 N for women (group of 61). The absolute maximum biting force these authors measured was 888 N and 576 N for men and women, respectively.

Loads vary among different researchers. As our implant model does not have an abutment to represent the application of the force on the false tooth that is going to be on top of it, the load has to be performed by a combination of a force and a moment load. I have researched available literature for boundary conditions (BCs) and specifically loads made by other authors. It is summarized in Table 16.

As we can see from Table 16, authors who perform analyses of bone-implant interaction for occlusal loads apply their load near-arbitrarily. This is because most of the analyses do not consider an actual physiological load but rather serve as a means of comparison between different structural variants (e.g., threaded vs. push-in implants, various implant diameters or, as in our case, a homogeneous vs. porous intraosseous part). Considering the worst scenarios of occlusal loads that can happen, I think it is important to remember that however we choose to load our assembly—as a rule of thumb—it should always consist of an axial load, a load perpendicular to the implant's axis (buccolingual) and a moment. Most of the authors mentioned in Table 16 meet these criteria by applying an oblique

Table 16: A brief summary of some other authors' load conditions for similar analyses. The main reviewed parameters are various force magnitude and angle configurations. The lingual direction is perpendicular to the occlusal plane (almost horizontal, towards the tongue), and the mesiodistal direction is between adjacent teeth. The mentioned forces are applied on the top of the tooth and generate a bending moment.

Authors	Vertical Force [N]	Other Forces
Rubo and Souza [142]	100	Straight vertical force
Quaresma et al. [143]	100	Straight vertical force
Chen et al. [144]	50–300	Also constant 18 N lingual force
Kayabaşı et al. [145]	114.6	Also 17.1 N lingual & 23.4 N mesiodistal
Huang et al. [146]	70	Also 70 N lingual force
Pierrisnard et al. [147]	70	Only 500 N lingual force
Marcián et al. i [148]	150	Straight vertical force
Marcián et al. ii [148]	106	Also 106 N lingual force
Marcián et al. iii [148]	0	Only 150 N lingual force

force at the top of the tooth replacement, so its buccolingual component also generates a moment. Therefore, all three criteria are met. Since our model does not include the implant superstructure (abutment, abutment screw, tooth prosthesis) because we are primarily interested in what happens at the peri-implant area, our load will be applied as illustrated in Figure 45. To apply a representative load in the buccolingual direction, let us specify a vertical force of 150 N, a 50 N force in the lingual direction and a 0.5 Nm moment the latter force would generate if it were situated 10 mm above the implant on a prosthetic crown.

Constraints of the models also vary among researchers. Historically, the human mandible was modeled as fixed [149]. This model should provide acceptable accuracy. Authors Teixeira et al. [150] suggested that in the human mandible, modeling segments which are wider than 4.2 mm mesio-distally from the implant is of little additional accuracy or use. This fact is often cited in scientific literature by other authors. However, the idea was conceived at a time when two-phase bone models were the norm and I would like to expand the model to include these areas. The BCs are further influenced by the contact conditions at the BII. Under normal circumstances, the bone is not perfectly bonded with the implant—a fact that has been underestimated in previous studies [149]. Authors Patra et al. [151] found that the anterior mandible—the location of implant placement in this work—achieves as much as 100% osseointegration. Then, the level of osseointegration decreases towards the posterior mandible, and the weakest osseointegration can be observed in the posterior maxilla with as little as 25%. Applying the 100% osseointegration condition in our simulation is, therefore, convenient in decreasing model complexity and is backed by these findings. I am aware that the 100% level would not ever be fully achieved, but it is a small concession that I—as well as other authors—am willing to make for the sake of simplicity. Some studies [145] also use the convenience of symmetry by using only half of the bone block and implant. However, this is unusable in our analysis as the gyroid structure has translational symmetry, not mirror symmetry. Therefore, I will be modeling the problem as a symmetrical half of the mandible with the entire implant to include the posterior region of the mandible and still save on computation time.

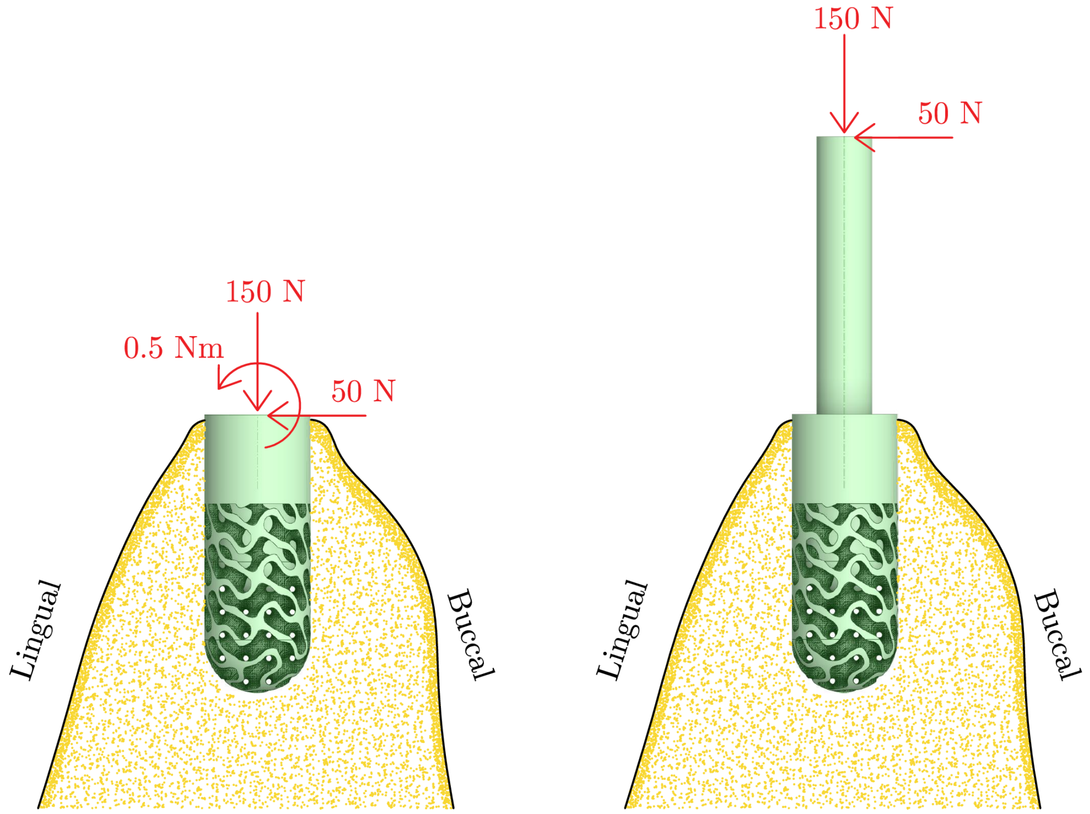

Figure 45: Loads applied to the implant variants, illustration on the gyroid-equipped implant. The choice is made arbitrarily based on short research listed in Table 16. Moment 0.5 Nm is equivalent to reducing the 50 N lingual force from ca. 10 mm higher, where the crown would typically be. Since in Mechanical Finder, it is not possible to simulate the load on the left, the variant on the right was adopted with a perfectly bonded, infinitely stiff rod that is 10 mm long and provides the moment load. The rod has a similar diameter to a real abutment screw.

Among similarly-oriented studies, such as [152, 153], the constraint of the model is limited to simply fixing (fully constraining) the bottom surface nodes of the mandible block cut-out. These BCs can be potentially refined by modeling the whole mandible by fixing only the top of the mandibular condyles, investigating forces generated by the muscles involved in mastication and their inclusion, modeling of the temporomandibular joint and other refinements. Most of these refinements are beyond the scope of this thesis and I am not investigating the true nature of stress distribution inside the bone during mastication but rather the differences between conventional and gyroid-equipped implants. However, with QCT/FEA, we can still improve upon modeling of block cut-outs and two-phase models of the mandible. In this analysis, I assume symmetry of the human mandible (in spite of the fact that mechanical properties might, of course, differ from one half to the other, it is still near-symmetrical) to reduce the complexity of the model and computation time. The model is shown in Figure 46.

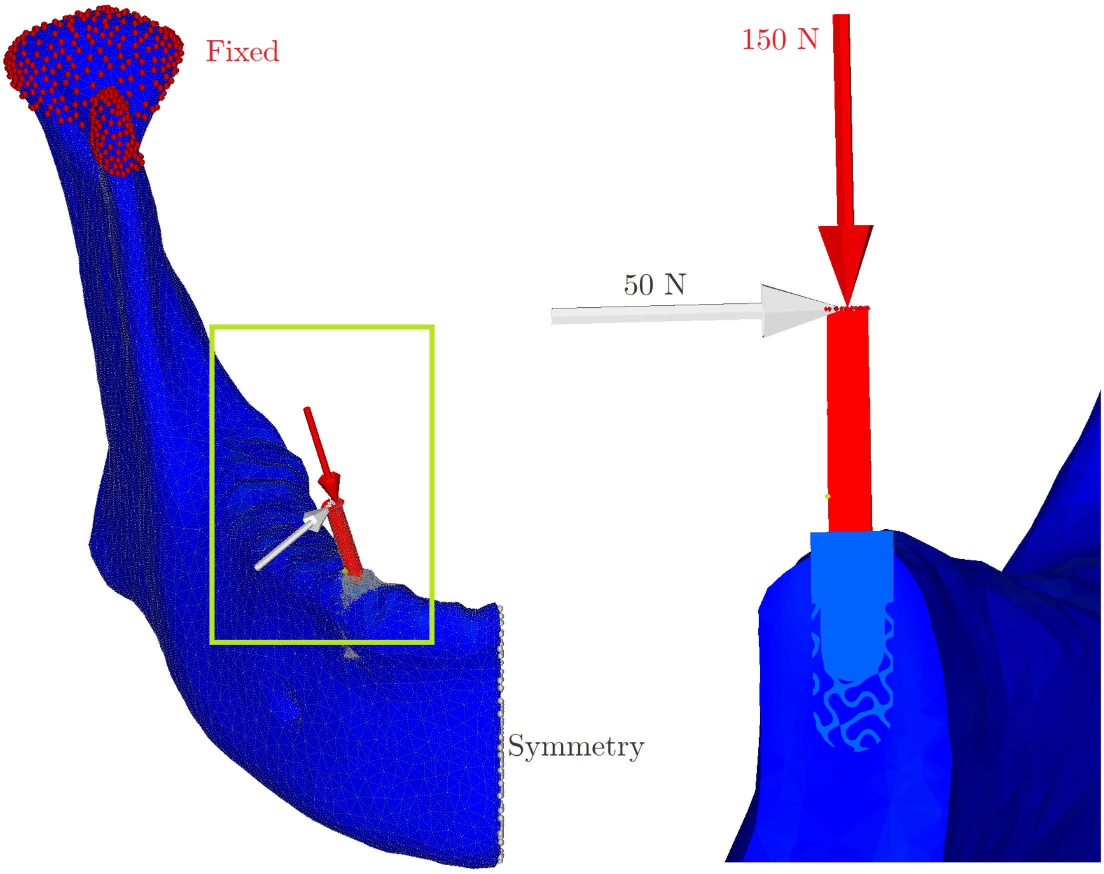

Figure 46: The 3D FEM model with visible boundary conditions. The problem is represented by a symmetrical half of the mandible. Light grey nodes on the right represent symmetry conditions. The jaw is fixed at the area of the temporomandibular joint (red nodes), and the loads are shown as two arrows. Left—the overall scene, right—detail of the light green rectangle displayed on a buccolingual section.

9.4 X-ray Numerical Model

This chapter is meant to be viewed as an addition to Chapter 9.3. It describes a different simulation using X-ray imaging with homogeneous implants. It should be viewed as the predecessor to the more detailed CT-based model with gyroid implants with the aim to describe some of the pitfalls of working with QCT/FEA. It arose as a collaborative work with MDDr. Mária Frolo from *Pražské centrum dentální implantologie* (Prague Center of Dental Implantology) in an effort to compare two variants of the *All-on-4* dental replacement system—the splinted and unsplinted system (or sometimes called the bar-supported and unsupported denture). The authors described the problem in detail in a recently published article [154]. The scene illustrating the situation is displayed in Figure 47.

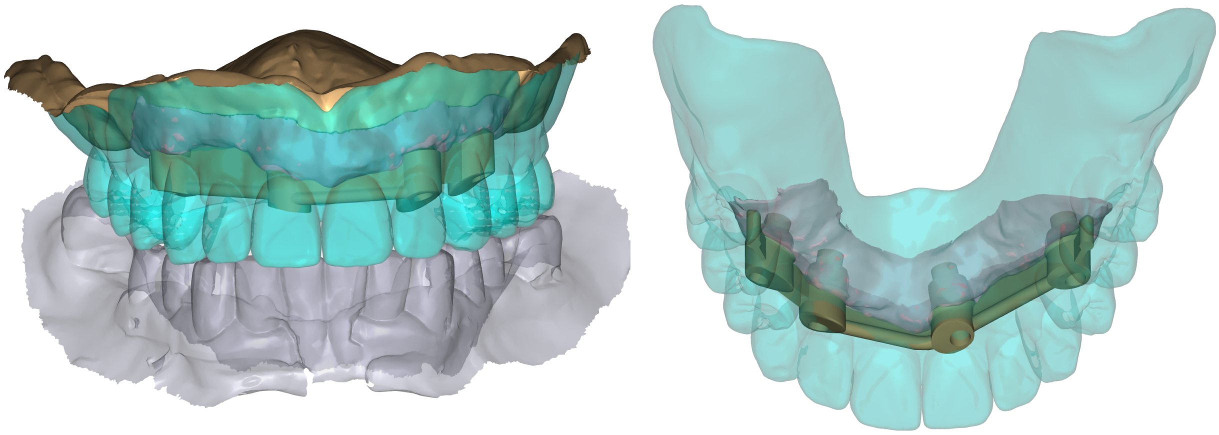

Figure 47: A scene illustrating the situation of the analyzed problem. Individual parts are visualizations of X-ray images of an anonymous patient with an individually modeled splinted implant assembly for their maxilla. Grey color represents the lower jaw, teal represents the maxillary overdenture, brown (on the right) represents the splinted assembly, and purple represents X-ray scans of the gums. This model provided the geometry for precise implant placement in the bone and position of the overdenture in relation to the implant assemblies. Intraosseous implants are not yet provided in this scene but rather modeled afterwards for QCT/FEA analyses of both variants. Figure taken from my co-authored work [154].

We can briefly examine some vital distinctions between X-ray and CT input data for QCT/FEA. Since no contemporary in vivo method offers any means of estimating the mechanical properties of bone, QCT/FEA remains the primary means of investigation. Edentulism (loss of all teeth) can be treated by preparing the jaw for four implants with a superstructure of either splinted or unsplinted metal parts and the overdenture [155]. The question is how much of a benefit does the splinting offer, as the splinted solution is more expensive and time-consuming. Usually, it would be employed where there are poor bone conditions in terms of mass and quality or where there are requirements for good connection (implant divergence), often in the maxilla (upper jaw) [156]. On the other hand, splinted implants offer better anti-rotational stability [157–159] and have a survival rate of 97% in 7 years post-operation [157, 160–162]. Another great benefit of splinted systems is their ease of maintenance and good stability of the overdenture [163], not being correlated with plaque accumulation, bone loss or peri-implantitis [164].

9.4.1 X-ray Reconstruction and Implant Geometries

The process of QCT/FEA reconstruction from CT was described in detail in Chapter 9.3.3. Now, let us focus on another area of imaging, the X-ray image. While much more available, convenient and cheaper to perform, an X-ray scan does not provide the imaging quality of a CT machine. While this is acceptable for the naked eye in clinical practice, working with X-ray data should be avoided in QCT/FEA. First, let us explore the differences in data processing. Mechanical Finder can process any sliced image data that is uncompressed. However, specific data need to be processed. Where a Phantom-calibrated CT scan is readily imported into the software, an X-ray scan has to be processed by first converting the data into JPG files, then converting to DICOM files and constructing a new project essentially by making a guess on the slice thickness and pixel size. After this process is done, one can continue with the reconstruction and ROI processing as described in Chapter 9.3.3. A comparison between typical X-ray and CT DICOM data is presented in Figure 48.

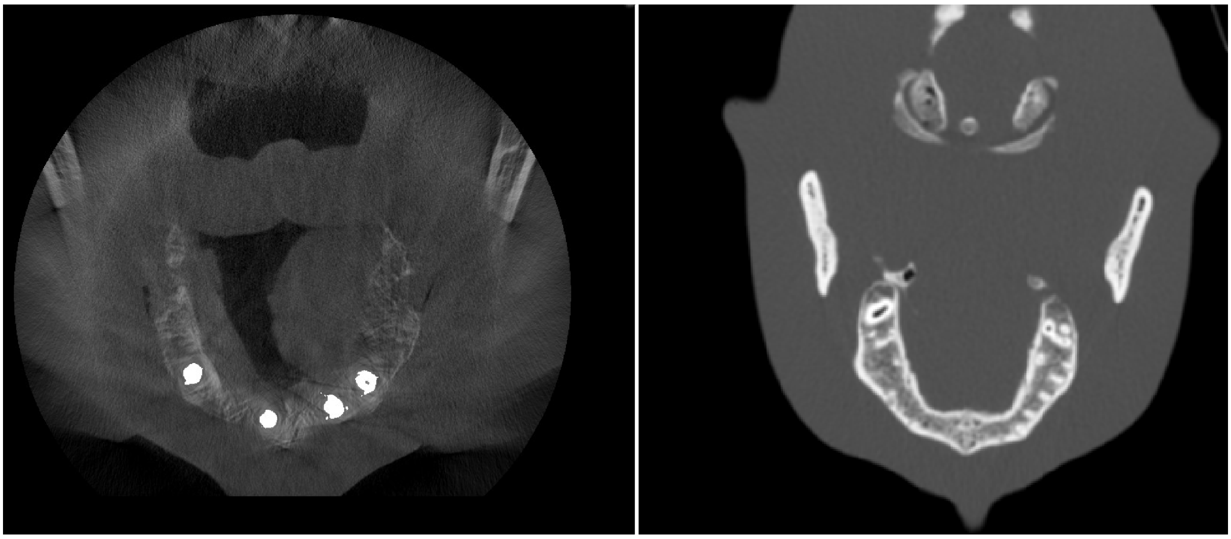

Figure 48: An arbitrarily chosen slice of X-ray (left) and CT (right) data of different patients. Notice the difference in quality—the CT image provides much clearer borders that indicate bone areas. When doing the process of manual ROI reconstruction, the CT data lends itself to much more precise and quicker processing.

Figure 49: The geometries that were analyzed inside the patient's maxilla. The All-on-4 splinted variant is on the left, and the unsplinted variant is on the right. This is a custom-made implant assembly designed to fit the individual patient. The geometries are near-identical, short of the stabilizing splints and the shape of the superstructure.

A special custom-fitted splinted dental implant assembly of an anonymous patient was provided. This assembly was carefully situated in the reconstructed bone model of the upper jaw according to the scene provided in Figure 47. The implant geometry can be seen in Figure 49.

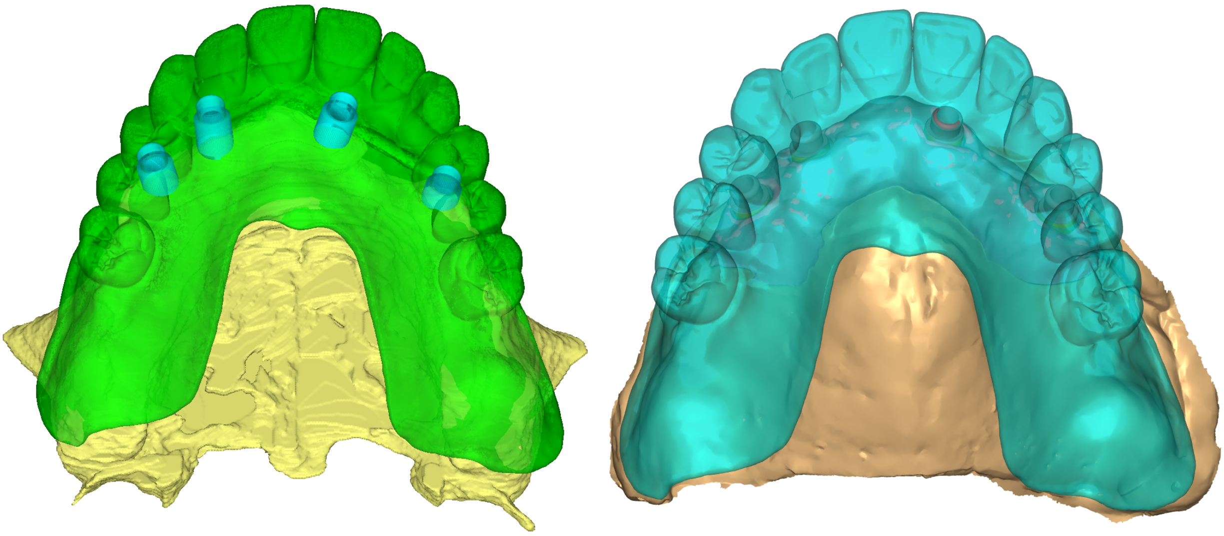

Figure 50: Left—The complete, reconstructed geometry of the modeled scene with a custom-made resin prosthetic. The location of the prosthetic with respect to the implants and to the bone was carefully fitted according to the supplied X-ray visualization shown on the right. The unsplinted variant is shown.

9.4.2 Boundary Conditions of the X-ray Analysis

The maxilla cutout made from the complete model of the X-ray data of the human skull was constrained by fixing the top planar cutout. Contact conditions were set for the areas where the resin prosthetic meets the bone, and the bone meets the implant. The BCs were different from the former CT analysis as now we need to describe a scene with the whole upper jaw, four implants and a prosthetic. Both incisors were loaded by a 150 N force slanted in the buccolingual direction by 35°. The analysis also included two other load cases—namely a 600 N force with a 15° slant applied on both molars and a 600 N force positioned directly above the second premolar tooth implant in the axis of the implant. The scene with one of the load cases and its BCs is displayed in Figure 51.

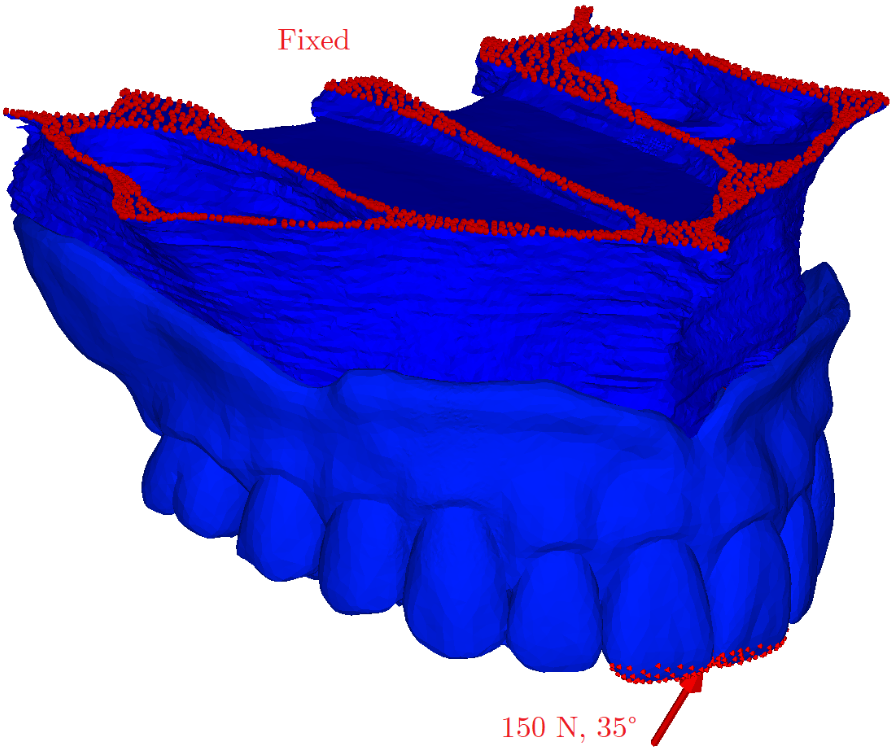

Figure 51: The boundary conditions of the X-ray analysis. As they are the same for both implant variants, only the unsplinted variant is displayed. The top planar cutout was fixed, and a 35° slanted 150 N force was applied to the first prosthetic tooth. The angle is measured in the buccolingual direction. There were more variants in the analyses, but showing them all would be redundant to illustrate the differences between CT and X-ray QCT/FEA. They included a 600 N force applied on the molars with a smaller buccolingual angle and a 600 N force positioned directly above the second premolar implant's axis.

9.4.3 X-ray Analysis with Gyroid Implants

A very interesting topic would be the investigation of stress differences between either the splinted or unsplinted variant with homogeneous implants and its gyroid-equipped counterpart. The null hypothesis is that the compressive stresses should be less localized and more evenly distributed along the length of the gyroid porous part. For this purpose, the model shown in Figure 52 was carefully created, replacing the original implants with a sheet-gyroid-equipped surface and keeping a homogeneous core. The length and width of the implants were kept.

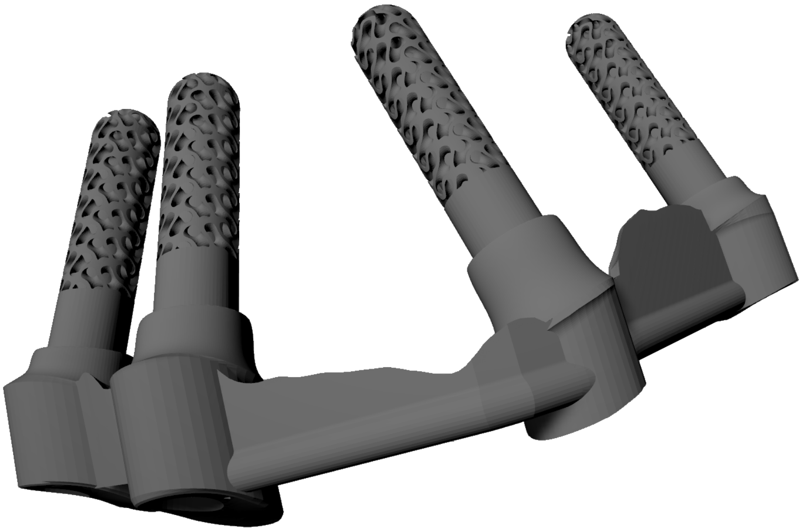

Figure 52: The newly designed splinted variant of the All-on-4 solution with a gyroid-equipped surface and a homogeneous core. The dimensions of the implant are the same as the analyzed one shown in Figure 49. The same gyroid implant assembly could be modeled for the unsplinted variant only by omitting the splints.

This kind of analysis, however, proves to be unrealistic on common PCs. In our QCT/FEA analysis of the mandible in Chapter 9.3, time requirements increased considerably when applying the gyroid porous structure on a conventional implant geometry. We should also consider that the model shown in Figure 52 has four implants instead of one, and each porous part is ca. twice as long. These factors inflate the element numbers of the final mesh of the QCT/FEA model into tens of millions, making it virtually unsolvable in real time (which I also tried, and I had to terminate the analysis). Also, the memory requirement for such analysis approaches a value near 100 GB—far more than contemporary non-professional, high-end PCs. If we wanted to solve complex porous structures this way, we would have to utilize the Message Passing Interface (MPI) technology to distribute the task to multiple computers. However, that would require significant effort and it would go against the idea of trying to simplify QCT/FEA for real-time use by clinical practitioners with low-end computers. An excellent solution to this problem could be researching further into the numerical homogenization method [124] and applying a layer of specified, homogenized material properties which should reduce the computational times significantly as the number of elements needed decreases. This could be a topic for further research in QCT/FEA analysis of porous structures, as discussed in Conclusions.

9.5 Results of Numerical Simulations

9.5.1 Results of the CT Analysis

In this chapter, we will compare the results of all the implant variants from Chapter 9.3 on stress distributions in bone and in the bodies of the implants. We are mainly interested in stress at the peri-implant area to investigate the effects of the gyroid structure on stress shielding. As the means of analyzing these complex geometries are difficult, I concede (as discussed in Chapter 9.3.5 on similar, non-gyroid oriented studies) that complete osseointegration of the implants (100% BIC at the peri-implant area) is assumed in all analyses.

Other quantities for evaluation were also considered. A stress-strain diagram, for example, could provide a good comparison. However, considering the porous part of the implant starts only below the bone level, the differences between the variants would be negligible. Even the standard that is used to evaluate fatigue strength of dental implants [165] specifies that this mechanical test be performed on specimens submerged into epoxy resin from a point before the porous structure begins (Figure 53). The idea of evaluation of any displacement was, therefore, discarded.

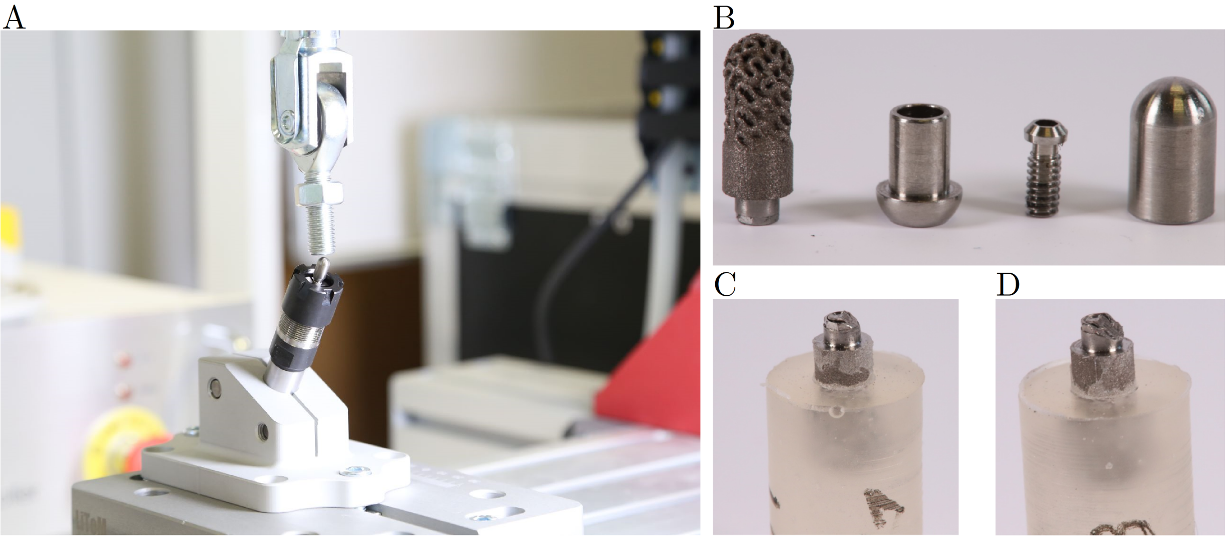

Figure 53: The ISO standard [165] setup that demonstrates the futility of evaluating force-displacement diagrams of intraosseous parts of dental implants. Taken from my other work [166]. Image is shown for illustration of embedding in the resin, not as an actual discussed part of the research. As the porous parts of the implants begin only below the point of submerging into epoxy resin, the measured and numerically simulated difference in response would be almost indistinguishable among our analyzed variants. A—a custom-made test apparatus that conforms with the standard, B—the tested specimen, C, D—screw failure during the test. Taken from my published work [167].

The evaluated results displayed on isolines that follow are the von Mises Equivalent Stress for metallic materials, Drucker-Prager Stress for bone materials (similar to von Mises, but pressure dependent, so suitable for bone), Minimum Principal Stress for bone materials (compressive stress in bone) and the Risk Factor, which is calculated as follows:

$$RF_t = \frac{\text{Max. Principal Stress [MPa]}}{\text{Critical Stress [MPa]}}\ [\%]; \quad RF_c = \frac{\text{Equivalent Stress [MPa]}}{\text{Yield Stress [MPa]}}\ [\%] \tag{21}$$

where RF_t and RF_c are Risk factors calculated for tensile and equivalent stress, respectively. Here, we use RF_c. The equivalent stress used is von Mises for metal materials and Drucker-Prager for bone.

The isolines of the Equivalent stress factor presented in Figure 59 show that the initial design of the porous structure could be problematic. While the gyroid variant in the same figure does not show an increased risk of fracture, the homogenized variant of the same structure shows that the porous layer should have higher yield strength. Figure 59 shows Equivalent Risk Factor values up to 20%, but the peak value in the homogenized outer porous layer goes up to 45%. This was discussed already between authors of the article about numerical homogenization [124] and I reanalyzed this variant with a porous outer homogeneous layer with higher values of mechanical properties ($E = 2.67$ GPa and $\sigma_y = 161.3$ MPa). The values can be arbitrarily higher, but they were chosen as values of the second least strong specimen from the previously mentioned article [124].

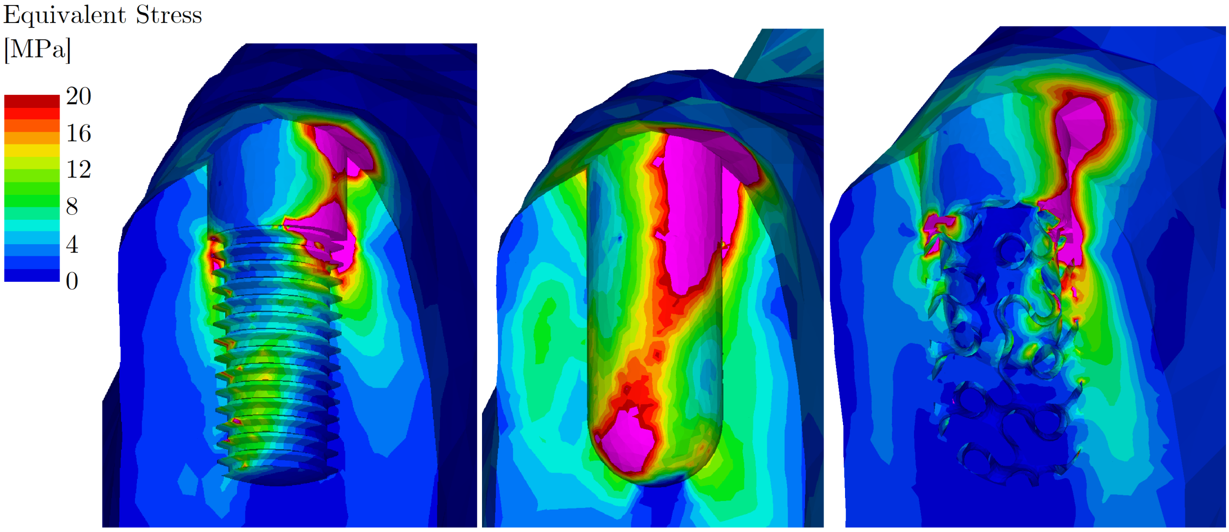

Figure 54: Equivalent stress in bone on a buccolingual section in the implants' centers. Left—the threaded implant variant, center—the homogenized variant, right—the gyroid variant. Pink color represents areas whose values are out of range of the color bar on the left. Their detailed extreme values are shown in Figure 55 instead.

The results are shown in Figure 64 and suggest that increasing E and mainly yield strength produces a structure that is much more reliable (for the given load). Increasing the yield strength by a large margin could potentially not be beneficial as E also increases (undesirable for bone at the peri-implant area [124]). Therefore, as a rule of thumb, the gyroid structure could be redesigned and tested to have its E somewhere higher in the units of GPa, perhaps in the range of $3 < E < 10$ GPa, which would have to be tested.

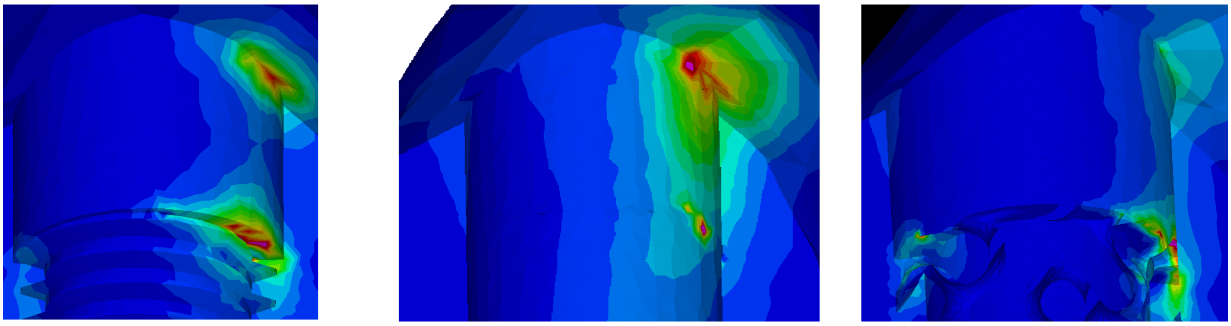

Figure 55: Detailed view of the extreme values of equivalent stress in bone from Figure 54. The extremes are all 120 MPa. They are located in the small, pink-colored areas.

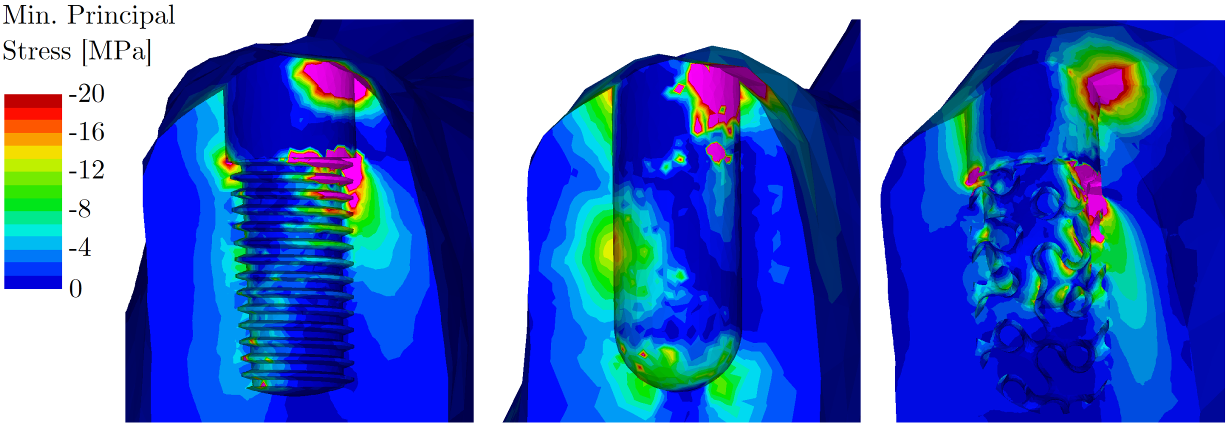

Figure 56: Minimum Principal Stress in bone on a buccolingual section in the implants' centers. Detailed extreme values are shown in Figure 57.

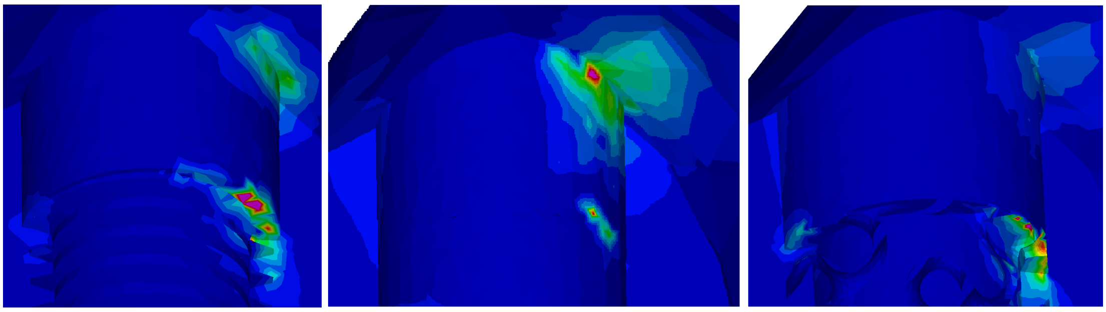

Figure 57: Detailed view of the extreme values of Minimum Principal Stress in bone from Figure 56. The extremes are—from the left—200 MPa, 150 MPa and 150 MPa.

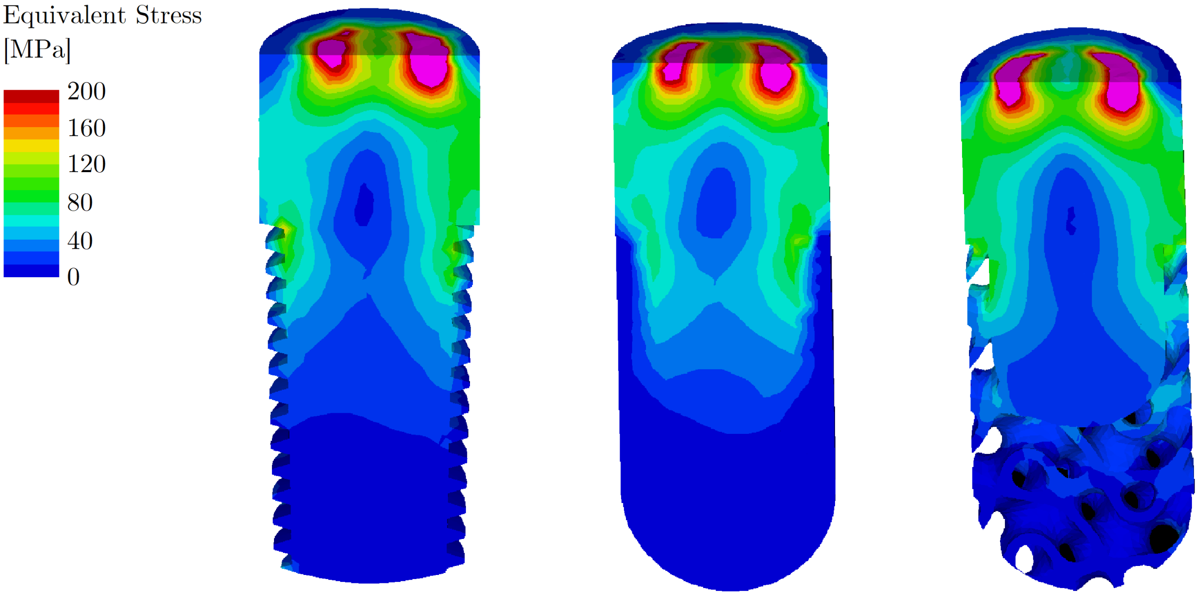

Figure 58: Equivalent stress in implants on a buccolingual section in the implants' centers. Left—the threaded implant variant, center—the homogenized variant, right—the gyroid variant.

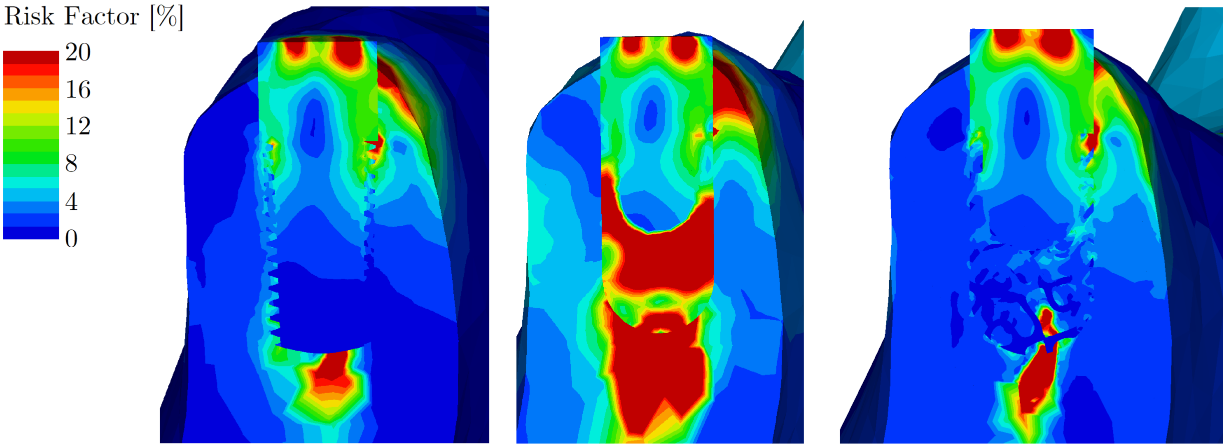

Figure 59: Equivalent Risk Factor RF_c (see Equation 21) in all materials displayed on a buccolingual section in the center of the implants. The details in bone can be seen in Figure 60.

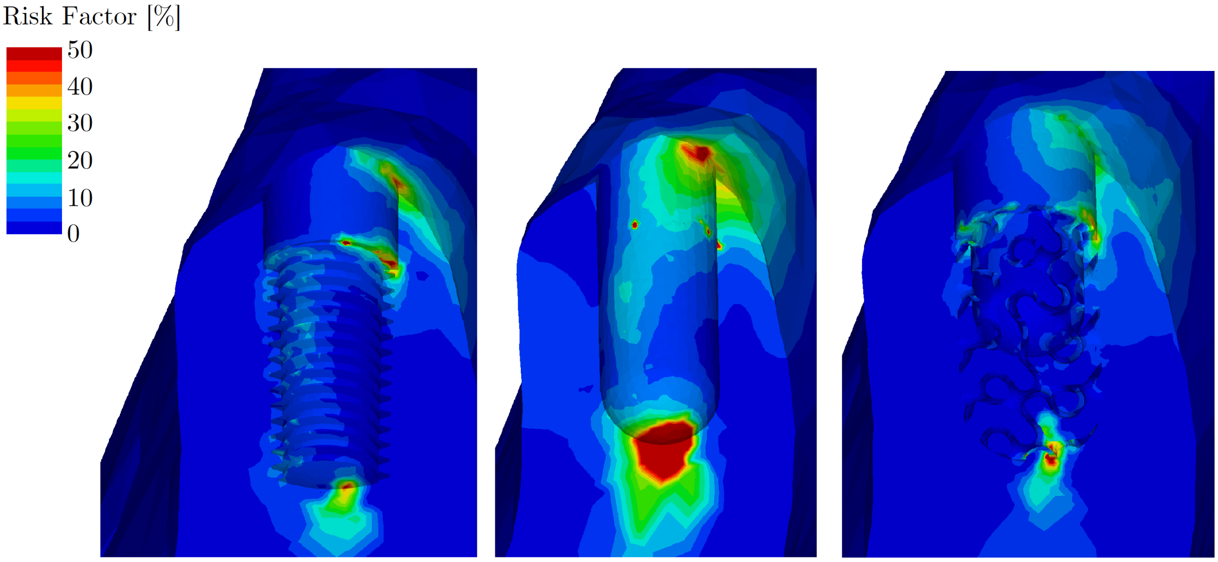

Figure 60: Equivalent Risk Factor RF_c in bone.

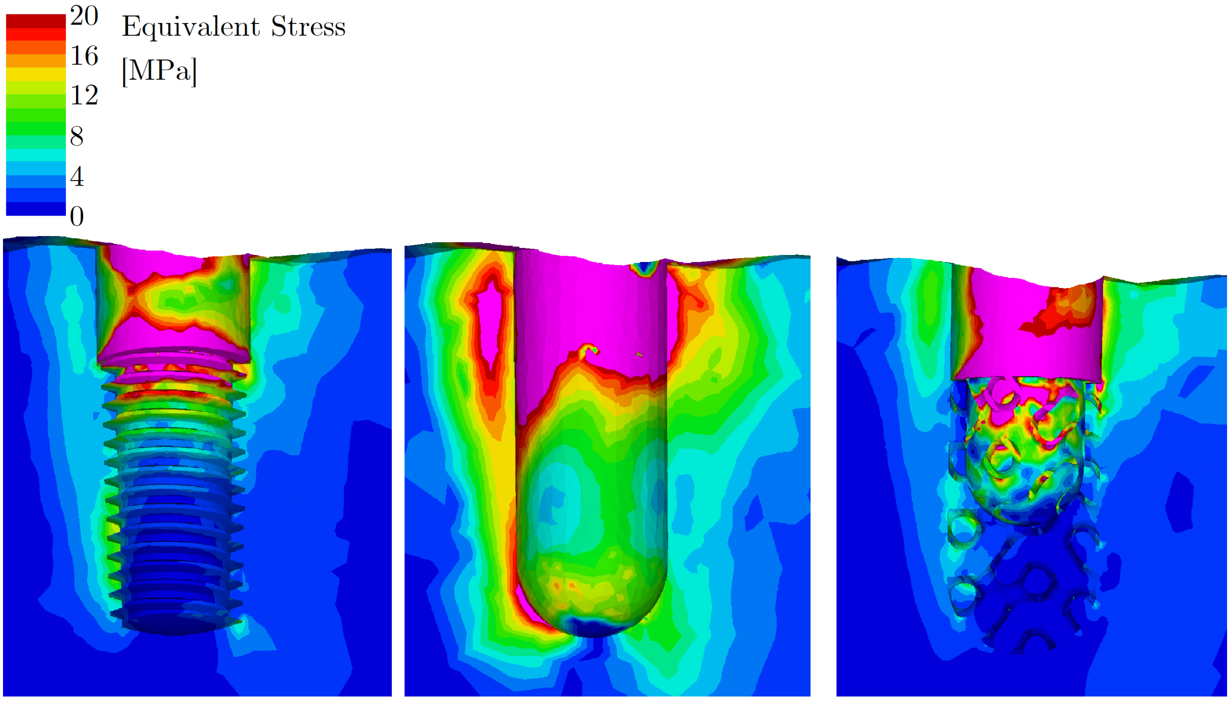

Figure 61: Equivalent stress in bone on a mesiodistal section in the implants' centers. Left—the threaded implant variant, center—the homogenized variant, right—the gyroid variant. Pink color represents areas whose values are out of range of the color bar on top. Their detailed extreme values are shown in Figure 62 instead.

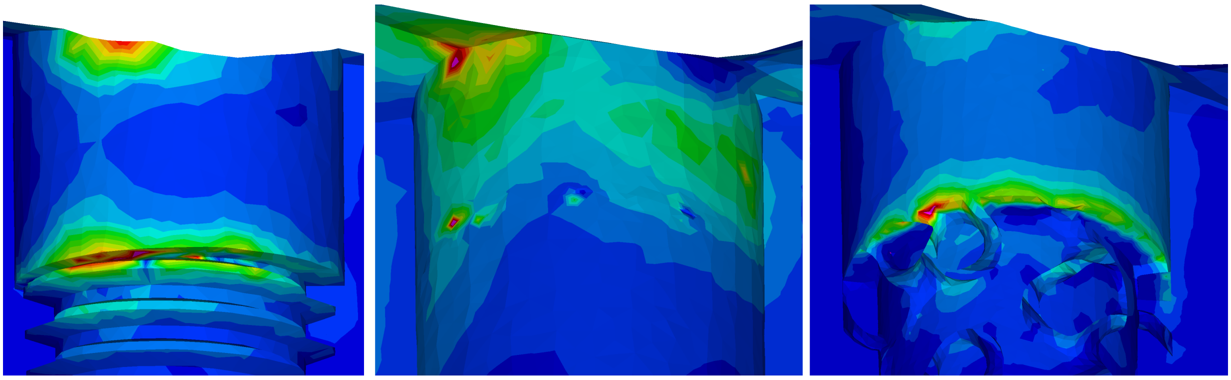

Figure 62: Detailed view of the extreme values of equivalent stress in bone from Figure 61. The extremes are—from the left—120 MPa, 130 MPa and 140 MPa.

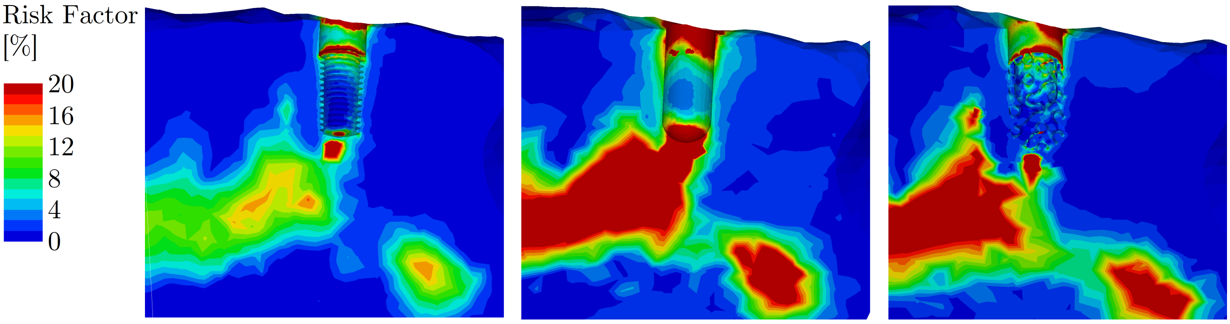

Figure 63: Equivalent Risk Factor RF_c in bone displayed on a mesiodistal section in the center of the implants. Values of RF_C on this section peak at ca. 30%.

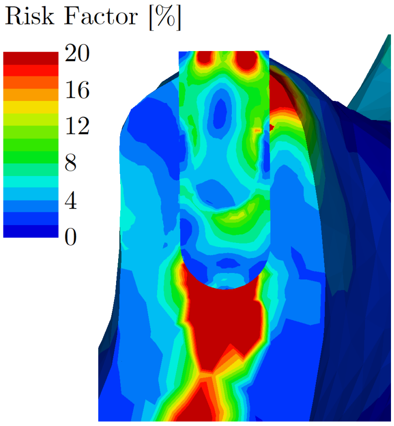

Figure 64: The modified homogenized, two-phase implant with a homogeneous core and an outer layer of specific properties. Values increased from $E = 1.24$ GPa and $\sigma_y = 31.0$ MPa to $E = 2.67$ GPa and $\sigma_y = 161.3$ MPa to match the second least strong specimen from [124].

9.5.2 Results of the X-ray Analysis

The results of the X-ray analysis show the differences between the splinted and unsplinted variant. As criteria, the Equivalent von Mises Stress was chosen for the implant and

Minimum Principal Stress was chosen for bone. The isolines of stress were normalized across all images, and only the relevant material was displayed to prevent confusion with large ranges of values. These results are a part of a research that has been recently published [154].

- **First load case**—150 N 35° slanted force—this load in the frontal section of the mandible showed small differences in equivalent stress between the implant variants as the loading force was located in the middle of the implant assembly. Therefore, the load can be distributed more evenly even in the unsplinted variant. The resin prosthetic on top of the implants also provides some additional stiffness in the xy plane to further prevent localization of stresses into the implant under load. The difference in compressive stress in bone is more pronounced between the variants as the splints provide good stiffness to prevent the individual implant from displacing too deep into bone. This is not present in the unsplinted variant and the compressive stresses are greater.
- **Second load case**—600 N 15° slanted force—this load case clearly demonstrates the strengths of the splinted variant as the splints can distribute the load to other implants and parts of the assembly. The unsplinted variant is forced to concentrate the whole load into the nearest implant, which is under significant bending. As for compressive stress in bone, this load case has perhaps the most pronounced difference between the analyzed variants. The z displacement of the outer implant in the unsplinted variant caused by the lack of splints accompanied by bending produces a significant difference.
- **Third load case**—600 N force parallel to underlying implant—in this variant, the difference in the stress distribution in implants is still recognizable, but bending is not present. Therefore the influence of splints is slightly diminished. Therefore, the difference in the stress state is less pronounced than in the second load case. The compressive stress in bone is again very distinguishable among the variants and overall higher than in the second load case. Even the splinted variant now experiences a small stress concentration, albeit much smaller than the unsplinted variant.

From Figures 65 and 66, we can see the stress distributions. The QCT/FEA method remains usable, but the results are negatively influenced by the quality of the X-ray reconstruction, which sometimes has to rely on guesswork during ROI reconstruction and manual assignments of values instead of precise automation and proper calibration by the Phantom device. The equivalent stress was used to evaluate stress distribution and peaks in the implants as it is a suitable measure for ductile materials like metals. In bone, it is more commonplace to be interested in either tensile or compressive stresses [168] (or pressure-dependent equivalent stresses) as bone lacks the ductility of metals and is relatively brittle. As the character of the load was predominantly compressive, and bending was in part prevented either by the splints or by the additional stiffness provided by the overdenture, Minimum Principal (compressive) Stress was chosen for bone assessment.

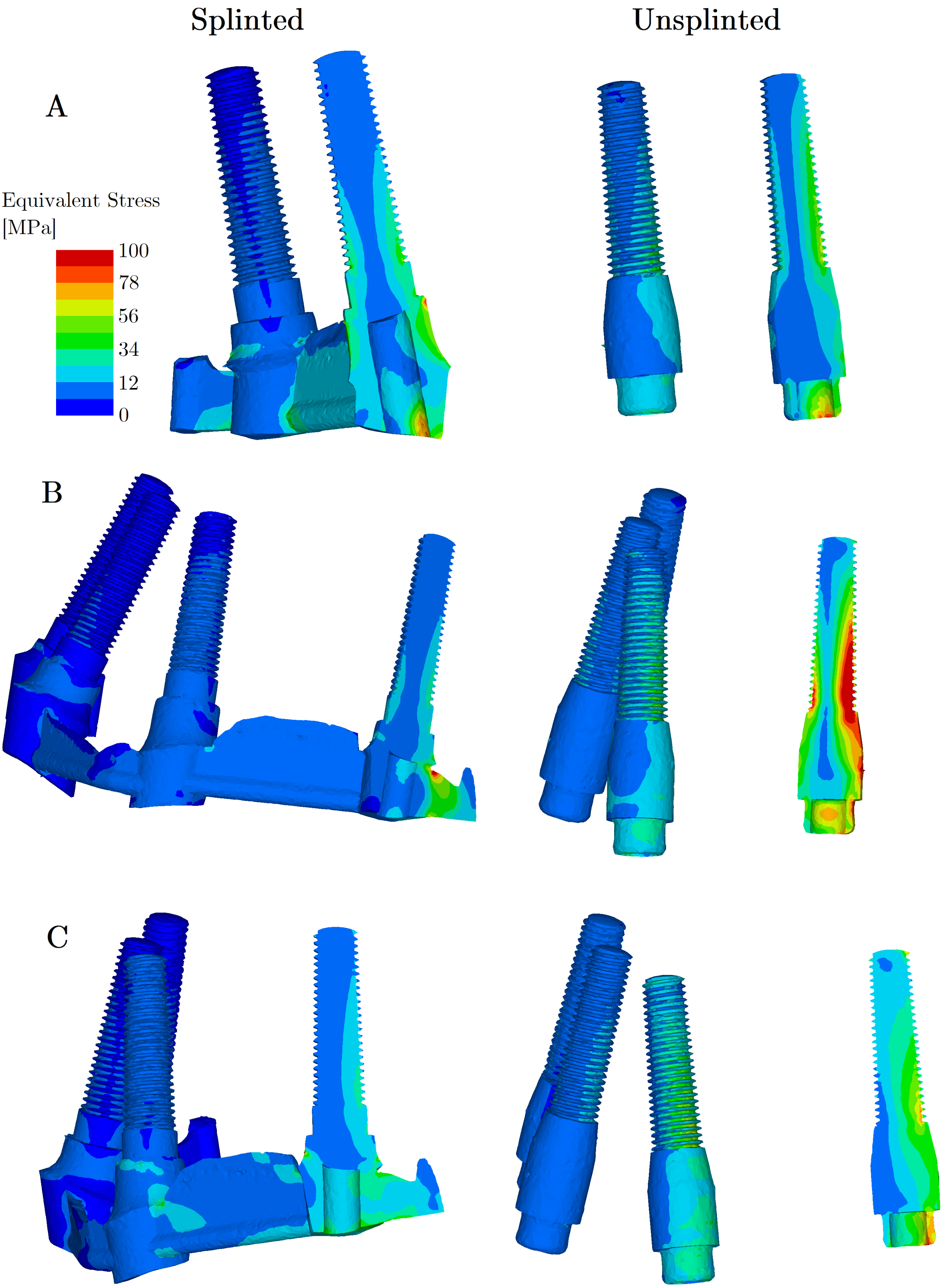

Figure 65: Equivalent stress in implants for all analyzed variants. Row A—first load case, row B—second load case, row C—third load case. Isolines normalized for all images. Figure taken from my co-authored work [154].

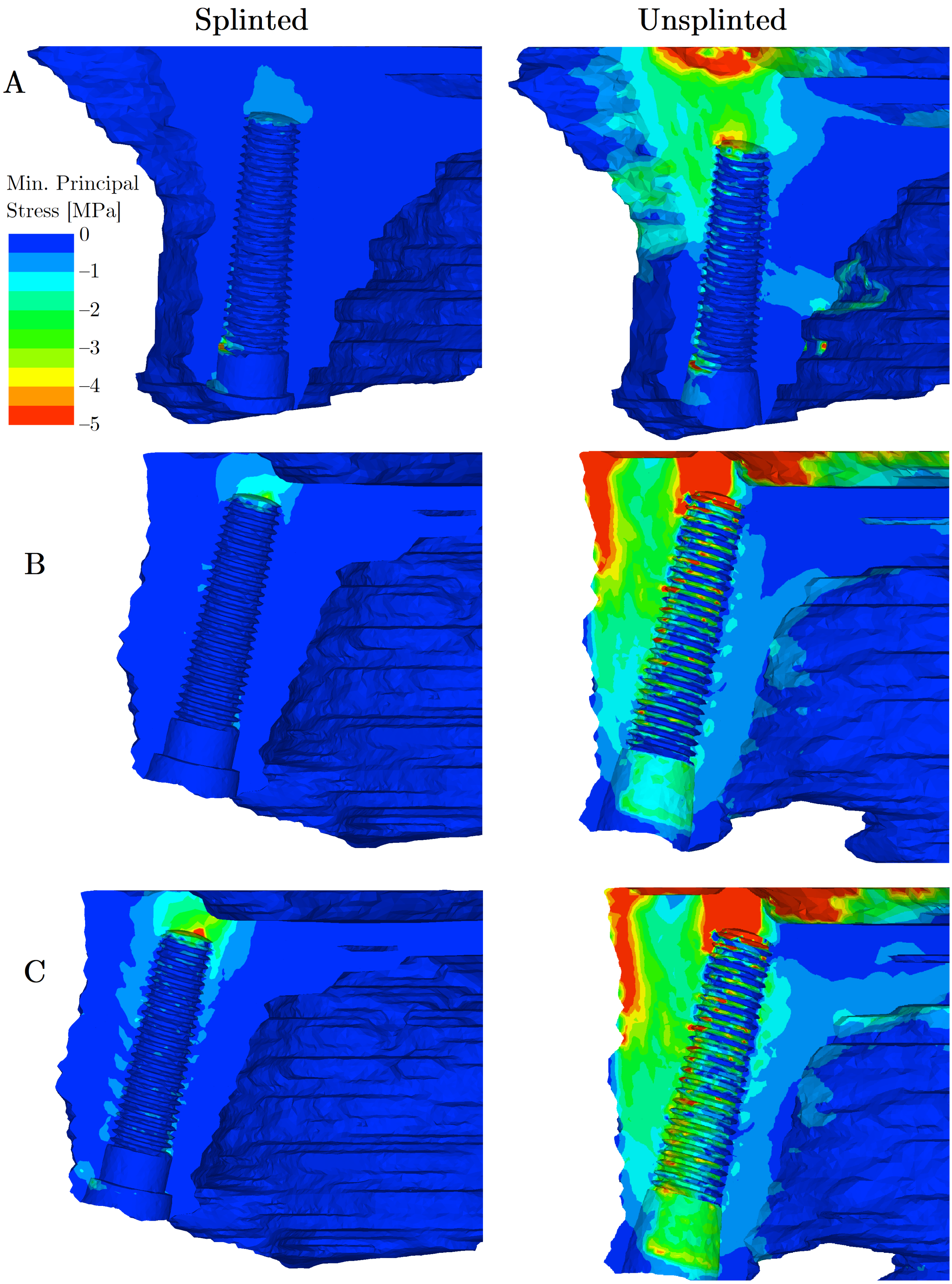

Figure 66: Minimum Principal Stress (compressive stress) in bone for all analyzed variants. Row A—first load case, row B—second load case, row C—third load case. Isolines normalized for all images. Figure taken from my co-authored work [154].

10 Conclusions

This dissertation aimed to propose an alternative to conventional implant surface treatment methods in the form of an outer porous layer that is a part of the implant itself. This is an attempt to help achieve good primary stability of the implant, prevent aseptic loosening and create a mechanical interlocking mechanism by allowing the bone beams to grow *inside* the implant itself, as opposed to conventional, machined implants, where the bone is only attached to the implant's surface by a smaller surface area. The proposed gyroid structure aims to improve the secondary, long-term stability and diminish the effects of stress shielding by reducing the *global* stiffness and allowing more load to be transferred to the bone so as to preserve its natural state and prevent demineralization as per the old Wolff's law.

After carefully investigating various requirements on intraosseous parts of implants, a novel gyroid-equipped dental implant was designed. The main biological requirement considered was pore size and shape. My previous participation in in vivo experiments [121] and literature research of other authors' works (Chapter 2) show that the broad range (300–1000 µm) of pore sizes is a good prerequisite for bone ingrowth. My choice for the design of the structure was a pore size of 600 µm and gyroid wall width of 200 µm, which should allow for good fluid flow through the system of interconnected pores and also for good mechanical resistance. The fluid flow inside the structure and the rate of capillary rise, which concern the transport of blood and nutrients, should be further investigated. As demonstrated in Chapters 7 and 8, the gyroid is superior to trabecular structures by eliminating the risks of local failures, chipping and discontinuities by introducing a smooth wall system with interconnected pores, as opposed to a beam system, where local defects can arise either during 3D printing or during the implant's clinical function.

We already investigated the beams of bone growing inside the body of a porous trabecular implant [121]. However, the amount of bone ingrowth inside a gyroid implant and the BIC is still to be determined experimentally. A MZ AZV VES (Ministry of Health) project submission with an extensive experimental in vivo program for this purpose is, therefore, currently underway. It also remains to be determined experimentally what pore sizes and porosity are optimal for bone ingrowth.

Recently, research has been trending toward developing alternative materials to conventional Ti, or Ti-6Al-4V, mainly in the form of β Ti alloys. As discussed in Chapter 4, these new materials benefit the implants by having lower elastic moduli that can match bone better and are also free of Al and V, which have various adverse health implications (Chapter 4.4.2). However, they are not currently viable for commercial 3D printing because materials like Ta and Nb, which these alloys usually contain, are much more expensive than Ti, Al and V, and the supply of their powder form for 3D printing is either very localized and scarce or not available at all at the present time. However, I think that going in this direction will be the right choice once the materials become more available in powder form. By having low moduli, they serve a similar purpose to the gyroid structure, reducing material mismatch and stress shielding.

For numerical modeling, it is essential to create a geometry with a high-quality tessellation, as usual methods of generating via CAD programs are sufficient for 3D printing but unusable for FEA. This was proven when I worked on providing working meshes for multiple variants of the gyroid and trabecular structures for the homogenization method. Working with more advanced instruments, such as the earlier mentioned MSLattice, worked well for generating meshes for FEA that do not suffer from inferior tessellation and overall bad quality caused by geometry errors.

The micromechanical and optical tests explain the reason for switching from trabecular structures, which were my former focus. They were carried out to investigate the mechanical properties at the micro level and local defects, respectively. The 3D-printed material was found to have properties matching those given by the manufacturer and, in fact, similar to conventionally machined products. The macromechanical tests showed that the sheet gyroid variant structure has ca. 2.5× higher peak stress values than its tubular variant and a control trabecular structure at the same porosity. Also, the sheet gyroid variant's character of collapse was superior to the tubular variant as it did not lose stability during compression and there were not any propagating defects and disconnections.

The QCT/FEA numerical model that was proposed used anonymous, patient-specific CT data of a human mandible with three different dental implant variants—a control, threaded implant, a gyroid-equipped implant and a homogenized implant. The analysis assumed complete osseointegration of the structures and, therefore, ideal contact conditions between the implant and bone. The contact surface between bone and implant is larger for a gyroid-equipped implant in comparison with a threaded or a conventional push-in implant and a compromise had to be made in mesh coarseness with the gyroid-equipped implant. For example, the simulation took about 1 hour to finish with the threaded implant with 240 000 elements. If we wanted ca. three elements per wall width with the gyroid variant, we would be approaching ca. 250 hours with 2 600 000 elements—which is far too long for real-time conditions and the intended use by clinical practitioners. The mesh had to be made more coarse with 2 elements per wall width to 1 270 000 elements and the analysis then took about 70 hours to complete on a standard PC mentioned in Chapter 9.

Another approach to numerical modeling is to homogenize the structure as described in a co-authored work mentioned in Chapter 9.3. This variant only demanded 130 000 elements and took 24 minutes to finish. However, choosing how to evaluate a simulation like that and verifying it should be investigated as an individual topic worth its own article or a thesis.

The results of numerical analyses shown in Chapter 9.5.1 indicate that the stress in bone is higher for the homogenized variant compared to the threaded variant, and the homogenized variant is intended to simulate the behavior of the gyroid structure. This is a positive effect because there are no significant unexpected stress concentrations besides the impacted part on the lingual side. However, the homogenized variant of the gyroid structure also revealed that the design should probably be improved so that the final structure is stronger and has a higher modulus. Since we are designing and homogenizing for modulus, I previously stated that $3 < E < 10$ GPa should be acceptable.

The threaded variant, which is the standard in dental implants, shows the highest concentrated stress values in bone among all the variants. It shows worse transfer of loads into bone compared to the homogenized variant. The gyroid variant provides comparable stress distribution in bone on the buccolingual section, but provides better, ca. 33 % lower peaks of stress compared to the threaded variant. Equivalent stress in implants is very similar. On the mesiodistal section, all variants provide similar peaks of equivalent stress and the gyroid and homogenized variants provide more favorable distribution. The difference is even more pronounced when comparing for the Compressive Risk Factor on the mesiodistal section, where both the gyroid and homogeneous variants load the bone in a larger area and provide ca. 2× greater stress values (peaks are ca. $RF_c = 15\%$ and $RF_c = 30\%$ for the threaded and both gyroid and homogenized variants, respectively).

Modeling the interaction between bone and the implant at the porous section will require additional FEA tools to be implemented and investigation of the contact conditions and the level of osseointegration. No significant non-linear effects, such as a large number of crushed or cracked elements, were produced for the selected load.

The simulations show that by applying a porous outer layer, we can achieve a better, less localized distribution of stresses at the peri-implant area in bone and reduce the effects of stress shielding. Higher but unlocalized compressive stress in bone is beneficial, as the bone is able to maintain its intended function and is not being demineralized. Bone loss can lead to severe complications and implant loosening, which requires reoperation, which then has to be performed on bone with even worse quality.

This thesis is a continuation of an ongoing research that started with my bachelor's thesis [169] on material properties of dental materials investigated by nanoindentation [169]. In that work, I laid out the properties of dental materials, including dentin, enamel and tooth filling (amalgam), for future research on dental implants. In my master's thesis [97], material properties of metallic trabecular structures were investigated along with creating an ANSYS Workbench numerical model of the trabecular structure that was curve-fitted with the experiment. Also, in vivo experiments on laboratory pigs that confirmed the possibility of bone ingrowth into porous implants were performed as a part of a research project. Working on a novel dental implant with a porous outer layer was mentioned at the end of my master's thesis. This dissertation expands on that idea by proposing a design of that dental implant in the form of a gyroid-equipped porous implant and also presents ways for optimization or tailoring of designs in the form of patient-specific QCT/FEA analyses, which are still to be improved upon, mainly in ease of operation and managing simulation times. Improvements in QCT/FEA—or FEA, generally—are desirable as they are quickly gaining popularity due to the high costs and complexity of in vitro and mainly in vivo experiments.

The areas of research that could be investigated in the future and would provide the greatest improvements for this dissertation's topic are the following:

- Determining optimal pore sizes and pore shapes from an extensive animal in vivo experiment followed with a histological analysis of bone segments and BIC evaluation;
- Searching for and developing means of manufacturing cheaper and more easily obtainable β Ti material powder materials for 3D printing;
- Investigating the printability of β Ti powders regarding their quality;
- Clarification of boundary and contact conditions like muscle and tendon insertions for better, more precise QCT/FEA modeling and predictions;
- Determining a realistic amount of bone ingrowth into the body of the porous implant and transferring that knowledge into FEA (this is hand in hand with Item 1 on this list and a project proposal has been submitted to investigate this topic);
- Simulations of fluid flow for numerical analyses of implants with porous layers (good fluid flow must be maintained so that vital nutrients can be transported through the system of pores);
- Designing an experiment for determining capillarity of the gyroid structure (a large system of pores is not useful if blood can only reach within the first millimeter of the structure);
- Novel design of a tensile test specimen that can withstand rapid heat exchange during 3D printing and also does not have defects preventing its testing;
- Designing an implant with a gradient gyroid structure to eliminate a sharp material transition between the homogeneous stem and the porous outer layer by continuously varying the porosity from its maximum to the homogeneous core.

List of Figures

As some of the figures and tables referenced in the List of Figures and List of Tables have very long descriptions, their lists only provide their shortened versions to prevent inflating the work. Chapter References is cited in full.

List of Tables

References

[1] Mohammad Abdelhamied Shuman. Patient's risk factors for dental implant success and failure (a retrospective study). *Egyptian Dental Journal*, 67(1-January (Oral Surgery)):219–223, 2021.

[2] Hassan Mohajerani, Roozbeh Roozbayani, Shahram Taherian, and Reza Tabrizi. The risk factors in early failure of dental implants: a retrospective study. *Journal of Dentistry*, 18(4):298, 2017.

[3] T Song, HP Tang, Y Li, and M Qian. Liquid metal dealloying of titanium-tantalum (ti-ta) alloy to fabricate ultrafine ta ligament structures: A comparative study in molten copper (cu) and cu-based alloys. *Corrosion Science*, 169:108600, 2020.

[4] Jinmeng Li, John A Jansen, X Frank Walboomers, and Jeroen JJP van den Beucken. Mechanical aspects of dental implants and osseointegration: A narrative review. *Journal of the mechanical behavior of biomedical materials*, 103:103574, 2020.

[5] T Hasegawa, S Kawabata, D Takeda, E Iwata, I Saito, S Arimoto, A Kimoto, M Akashi, H Suzuki, and T Komori. Survival of brånemark system mk iii implants and analysis of risk factors associated with implant failure. *International journal of oral and maxillofacial surgery*, 46(2):267–273, 2017.

[6] Luboš Řehounek and Aleš Jíra. Experimental and numerical analyses of a 3d-printed titanium trabecular dental implant. *Acta Polytechnica*, 57(3):218–228, 2017.

[7] Amit Bandyopadhyay, Felix Espana, Vamsi Krishna Balla, Susmita Bose, Yusuke Ohgami, and Neal M Davies. Influence of porosity on mechanical properties and in vivo response of ti6al4v implants. *Acta biomaterialia*, 6(4):1640–1648, 2010.

[8] Xiaojian Wang, Shanqing Xu, Shiwei Zhou, Wei Xu, Martin Leary, Peter Choong, Ma Qian, Milan Brandt, and Yi Min Xie. Topological design and additive manufacturing of porous metals for bone scaffolds and orthopaedic implants: A review. *Biomaterials*, 83:127–141, 2016.

[9] Naoya Taniguchi, Shunsuke Fujibayashi, Mitsuru Takemoto, Kiyoyuki Sasaki, Bungo Otsuki, Takashi Nakamura, Tomiharu Matsushita, Tadashi Kokubo, and Shuichi Matsuda. Effect of pore size on bone ingrowth into porous titanium implants fabricated by additive manufacturing: An in vivo experiment. *Materials Science and Engineering: C*, 59:690–701, 2016.

[10] Eric Alexander Lewallen, Scott M Riester, Carolina A Bonin, Hilal Maradit Kremers, Amel Dudakovic, Sanjeev Kakar, Robert C Cohen, Jennifer J Westendorf, David G Lewallen, and Andre J van Wijnen. Biological strategies for improved osseointegration and osteoinduction of porous metal orthopedic implants. *Tissue Engineering Part B: Reviews*, 21(2):218–230, 2015.

[11] Rima M Wazen, Louis-Philippe Lefebvre, Eric Baril, and Antonio Nanci. Initial evaluation of bone ingrowth into a novel porous titanium coating. *Journal of Biomedical Materials Research Part B: Applied Biomaterials*, 94(1):64–71, 2010.

[12] Sajad Arabnejad, Burnett Johnston, Michael Tanzer, and Damiano Pasini. Fully porous 3d printed titanium femoral stem to reduce stress-shielding following total hip arthroplasty. *Journal of Orthopaedic Research*, 35(8):1774–1783, 2017.

[13] Straumann BLX Regular Base Dental Implant. `https://www.spotimplant.com/en/dental-implants/straumann/blx-regular-base`. Accessed: 2022-08-09.

[14] Octalock Push-In. `https://www.spotimplant.com/en/dental-implants/dyna-dental/octalock-push-in`. Accessed: 2022-08-09.

[15] Afida Jemat, Mariyam Jameelah Ghazali, Masfueh Razali, and Yuichi Otsuka. Surface modifications and their effects on titanium dental implants. *BioMed research international*, 2015, 2015.

[16] Furqan A Shah, Anders Snis, Aleksandar Matic, Peter Thomsen, and Anders Palmquist. 3d printed ti6al4v implant surface promotes bone maturation and retains a higher density of less aged osteocytes at the bone-implant interface. *Acta biomaterialia*, 30:357–367, 2016.

[17] Ángel E Mercado-Pagán, Alexander M Stahl, Yaser Shanjani, and Yunzhi Yang. Vascularization in bone tissue engineering constructs. *Annals of biomedical engineering*, 43(3):718–729, 2015.

[18] Zimmer Biomet Trabecular Metal. `https://www.zimmerbiomet.com/medical-professionals/common/our-science/trabecular-metal-technology.html`. Accessed: 2021-03-09.

[19] David M Dohan Ehrenfest, Paulo G Coelho, Byung-Soo Kang, Young-Taeg Sul, and Tomas Albrektsson. Classification of osseointegrated implant surfaces: materials, chemistry and topography. *Trends in biotechnology*, 28(4):198–206, 2010.

[20] NA Athanasou. The pathobiology and pathology of aseptic implant failure. *Bone & joint research*, 5(5):162–168, 2016.

[21] *Experimental Stress Analysis - 57th International Scientific Conference*, Trabecular structures as efficient surface of dental implants, Luhačovice, Czechia, 2019. `www.experimentalni-mechanika.cz/cs/konference/konference/2019.html`.

[22] Sajad Arabnejad, R Burnett Johnston, Jenny Ann Pura, Baljinder Singh, Michael Tanzer, and Damiano Pasini. High-strength porous biomaterials for bone replacement: A strategy to assess the interplay between cell morphology, mechanical properties, bone ingrowth and manufacturing constraints. *Acta biomaterialia*, 30:345–356, 2016.

[23] A Yánez, A Herrera, O Martel, D Monopoli, and H Afonso. Compressive behaviour of gyroid lattice structures for human cancellous bone implant applications. *Materials Science and Engineering: C*, 68:445–448, 2016.

[24] D Barba, E Alabort, and RC Reed. Synthetic bone: design by additive manufacturing. *Acta biomaterialia*, 97:637–656, 2019.

[25] JD Bobyn, RM Pilliar, HU Cameron, GC Weatherly, and GM Kent. The effect of porous surface configuration on the tensile strength of fixation of implants by bone ingrowth. *Clinical orthopaedics and related research*, (149):291–298, 1980.

[26] Karl-Heinz Frosch, Florian Barvencik, Volker Viereck, Christoph H Lohmann, Klaus Dresing, Jürgen Breme, Edgar Brunner, and Klaus Michael Stürmer. Growth behavior, matrix production, and gene expression of human osteoblasts in defined cylindrical titanium channels. *Journal of Biomedical Materials Research Part A: An Official Journal of The Society for Biomaterials, The Japanese Society for Biomaterials, and The Australian Society for Biomaterials and the Korean Society for Biomaterials*, 68(2):325–334, 2004.

[27] Simon Van Bael, Yoke Chin Chai, Silvia Truscello, Maarten Moesen, Greet Kerckhofs, Hans Van Oosterwyck, J-P Kruth, and JJAB Schrooten. The effect of pore geometry on the in vitro biological behavior of human periosteum-derived cells seeded on selective laser-melted ti6al4v bone scaffolds. *Acta biomaterialia*, 8(7):2824–2834, 2012.

[28] Qichun Ran, Weihu Yang, Yan Hu, Xinkun Shen, Yonglin Yu, Yang Xiang, and Kaiyong Cai. Osteogenesis of 3d printed porous ti6al4v implants with different pore sizes. *Journal of the mechanical behavior of biomedical materials*, 84:1–11, 2018.

[29] Dong Wang, Guo He, Ye Tian, Ning Ren, Jiahua Ni, Wei Liu, and Xianlong Zhang. Evaluation of channel-like porous-structured titanium in mechanical properties and osseointegration. *Journal of Materials Science & Technology*, 44:160–170, 2020.

[30] Luana Marotta Reis de Vasconcellos, Daniel Oliveira Leite, Fernanda Nascimento de Oliveira, Yasmin Rodarte Carvalho, and Carlos Alberto Alves Cairo. Evaluation of bone ingrowth into porous titanium implant: histomorphometric analysis in rabbits. *Brazilian oral research*, 24(4):399–405, 2010.

[31] Peisheng Liu, Chao Fu, Tiefan Li, and Changxu Shi. Relationship between tensile strength and porosity for high porosity metals. *Science in China Series E: Technological Sciences*, 42(1):100–107, 1999.

[32] PS Liu, XS Wang, and HY Luo. Relationship between tensile strength and porosity for foamed metals under equal speed biaxial tension. *Materials science and technology*, 19(7):985–986, 2003.

[33] Markus LR Schwarz, Markus Kowarsch, Steffen Rose, Kristianna Becker, Tamara Lenz, and Lutz Jani. Effect of surface roughness, porosity, and a resorbable calcium phosphate coating on osseointegration of titanium in a minipig model. *Journal of Biomedical Materials Research Part A: An Official Journal of The Society for Biomaterials, The Japanese Society for Biomaterials, and The Australian Society for Biomaterials and the Korean Society for Biomaterials*, 89(3):667–678, 2009.

[34] Zena J Wally, William Van Grunsven, Frederik Claeyssens, Russell Goodall, and Gwendolen C Reilly. Porous titanium for dental implant applications. *Metals*, 5(4):1902–1920, 2015.

[35] GAP Renders, L Mulder, LJ Van Ruijven, and TMGJ Van Eijden. Porosity of human mandibular condylar bone. *Journal of anatomy*, 210(3):239–248, 2007.

[36] T Hara, M Takizawa, T Sato, and Y Ide. Mechanical properties of buccal compact bone of the mandibular ramus in human adults and children: relationship of the elastic modulus to the direction of the osteon and the porosity ratio. *The Bulletin of Tokyo Dental College*, 39(1):47–55, 1998.

[37] C Verna, B Melsen, and F Melsen. Differences in static cortical bone remodeling parameters in human mandible and iliac crest. *Bone*, 25(5):577–583, 1999.

[38] MS Stein, SA Feik, CDL Thomas, JG Clement, and JD Wark. An automated analysis of intracortical porosity in human femoral bone across age. *Journal of Bone and Mineral Research*, 14(4):624–632, 1999.

[39] KL Bell, N Loveridge, J Power, N Garrahan, BF Meggitt, and J Reeve. Regional differences in cortical porosity in the fractured femoral neck. *Bone*, 24(1):57–64, 1999.

[40] Richard B Ashman and Jae Young Rho. Elastic modulus of trabecular bone material. *Journal of biomechanics*, 21(3):177–181, 1988.

[41] Rod K Quinn and Neal R Armstrong. Electrochemical and surface analytical characterization of titanium and titanium hydride thin film electrode oxidation. *Journal of the Electrochemical Society*, 125(11):1790, 1978.

[42] CN Elias, JHC Lima, R Valiev, and MA Meyers. Biomedical applications of titanium and its alloys. *Jom*, 60(3):46–49, 2008.

[43] K Bordji, JY Jouzeau, D Mainard, E Payan, P Netter, KT Rie, T Stucky, and M Hage-Ali. Cytocompatibility of ti-6al-4v and ti-5al-2.5 fe alloys according to three surface treatments, using human fibroblasts and osteoblasts. *Biomaterials*, 17(9):929–940, 1996.

[44] Hironobu Matsuno, Atsuro Yokoyama, Fumio Watari, Motohiro Uo, and Takao Kawasaki. Biocompatibility and osteogenesis of refractory metal implants, titanium, hafnium, niobium, tantalum and rhenium. *Biomaterials*, 22(11):1253–1262, 2001.

[45] E Eisenbarth, D Velten, M Müller, R Thull, and J Breme. Biocompatibility of β-stabilizing elements of titanium alloys. *Biomaterials*, 25(26):5705–5713, 2004.

[46] D BomBač, Miha Brojan, Peter Fajfar, Franc Kosel, and Rado Turk. Review of materials in medical applications pregled materialov v medicinskih aplikacijah. *RMZ–Materials and Geoenvironment*, 54(4):471–499, 2007.

[47] Mitsuo Niinomi. Mechanical biocompatibilities of titanium alloys for biomedical applications. *Journal of the mechanical behavior of biomedical materials*, 1(1):30–42, 2008.

[48] JJ Jacobs, AK Skipor, J Black, RM Urban, and JO Galante. Release and excretion of metal in patients who have a total hip-replacement component made of titanium-base alloy. *The Journal of bone and joint surgery. American volume*, 73(10):1475–1486, 1991.

[49] JL Woodman, JJ Jacobs, JO Galante, and RM Urban. Metal ion release from titanium-based prosthetic segmental replacements of long bones in baboons: A long-term study. *Journal of Orthopaedic Research*, 1(4):421–430, 1983.

[50] K Merritt, RW Margevicius, and SA Brown. Storage and elimination of titanium, aluminum, and vanadium salts, in vivo. *Journal of biomedical materials research*, 26(11):1503–1515, 1992.

[51] Donald T Reilly, Albert H Burstein, and Victor H Frankel. The elastic modulus for bone. *Journal of biomechanics*, 7(3):271–275, 1974.

[52] J-E Bidaux, C Closuit, M Rodriguez-Arbaizar, D Zufferey, and E Carreño-Morelli. Metal injection moulding of low modulus ti–nb alloys for biomedical applications. *Powder Metallurgy*, 56(4):263–266, 2013.

[53] RM Pilliar, HU Cameron, AG Binnington, John Szivek, and I Macnab. Bone ingrowth and stress shielding with a porous surface coated fracture fixation plate. *Journal of Biomedical Materials Research*, 13(5):799–810, 1979.

[54] Petr Vakrčka, Aleš Jira, and Luboš Řehounek. Numerical analyses of the gyroid structure for use in dental and orthopaedic implants. pages 544–547, 2019. 57th International Scientific Conference on Experimental Stress Analysis (EAN), Luhacovice, CZECH REPUBLIC, JUN 03-06, 2019.

[55] Dale R Sumner and JORGE O Galante. Determinants of stress shielding. *Clinical orthopaedics and related research*, 274:203–212, 1992.

[56] Jochem Nagels, Mariëlle Stokdijk, and Piet M Rozing. Stress shielding and bone resorption in shoulder arthroplasty. *Journal of shoulder and elbow surgery*, 12(1):35–39, 2003.

[57] J Ryan Martin, Chad D Watts, Daniel L Levy, and Raymond H Kim. Medial tibial stress shielding: a limitation of cobalt chromium tibial baseplates. *The Journal of arthroplasty*, 32(2):558–562, 2017.

[58] Eyitayo Olatunde Olakanmi, RF Cochrane, and KW Dalgarno. A review on selective laser sintering/melting (sls/slm) of aluminium alloy powders: Processing, microstructure, and properties. *Progress in Materials Science*, 74:401–477, 2015.

[59] Selective laser sintering. `https://www.sciencedirect.com/topics/materials-science/selective-laser-sintering`. Accessed: 2022-03-07.

[60] Bharat Bhushan and Matt Caspers. An overview of additive manufacturing (3d printing) for microfabrication. *Microsystem Technologies*, 23(4):1117–1124, 2017.

[61] Emmanouil L Papazoglou, Nikolaos E Karkalos, Panagiotis Karmiris-Obratański, and Angelos P Markopoulos. On the modeling and simulation of slm and sls for metal and polymer powders: A review. *Archives of Computational Methods in Engineering*, pages 1–33, 2021.

[62] Hyub Lee, Chin Huat Joel Lim, Mun Ji Low, Nicholas Tham, Vadakke Matham Murukeshan, and Young-Jin Kim. Lasers in additive manufacturing: A review. *International Journal of Precision Engineering and Manufacturing-Green Technology*, 4(3):307–322, 2017.

[63] Lai-Chang Zhang, Yujing Liu, Shujun Li, and Yulin Hao. Additive manufacturing of titanium alloys by electron beam melting: a review. *Advanced Engineering Materials*, 20(5):1700842, 2018.

[64] C Körner. Additive manufacturing of metallic components by selective electron beam melting—a review. *International Materials Reviews*, 61(5):361–377, 2016.

[65] YJ Liu, SJ Li, HL Wang, WT Hou, YL Hao, R Yang, TB Sercombe, and Laichang C Zhang. Microstructure, defects and mechanical behavior of beta-type titanium porous structures manufactured by electron beam melting and selective laser melting. *Acta materialia*, 113:56–67, 2016.

[66] FH Froes and Bhaskar Dutta. *The additive manufacturing (AM) of titanium alloys*, volume 1019. Trans Tech Publ, 2014.

[67] Ryan Dehoff, Chad Duty, William Peter, Yukinori Yamamoto, Wei Chen, Craig Blue, and Cory Tallman. Case study: additive manufacturing of aerospace brackets. *Advanced Materials & Processes*, 171(3):19–23, 2013.

[68] Jeffrey W Stansbury and Mike J Idacavage. 3d printing with polymers: Challenges among expanding options and opportunities. *Dental materials*, 32(1):54–64, 2016.

[69] Tuan D Ngo, Alireza Kashani, Gabriele Imbalzano, Kate TQ Nguyen, and David Hui. Additive manufacturing (3d printing): A review of materials, methods, applications and challenges. *Composites Part B: Engineering*, 143:172–196, 2018.

[70] Nicolae Octavian Balc, Petru Berce, and Razvan Pacurar. Comparison between slm and sls in producing complex metal parts. *Annals of DAAAM & Proceedings*, pages 7–9, 2010.

[71] CY Wang. Rapid manufacturing: overview, 2002.

[72] Eyitayo Olatunde Olakanmi. *Direct selective laser sintering of aluminium alloy powders*. PhD thesis, University of Leeds, 2008.

[73] EO Olakanmi, RF Cochrane, and KW Dalgarno. Spheroidisation and oxide disruption phenomena in direct selective laser melting (slm) of pre-alloyed al-mg and al-si powders. In *Proceedings: TMS Annual Meetings and Exhibition*, pages 371–380, 2009.

[74] J-P Kruth, G Levy, F Klocke, and THC Childs. Consolidation phenomena in laser and powder-bed based layered manufacturing. *CIRP annals*, 56(2):730–759, 2007.

[75] Pere Barriobero-Vila, Katia Artzt, Andreas Stark, Norbert Schell, Martin Siggel, Joachim Gussone, Jan Kleinert, Wolfgang Kitsche, Guillermo Requena, and Jan Haubrich. Mapping the geometry of ti-6al-4v: From martensite decomposition to localized spheroidization during selective laser melting. *Scripta Materialia*, 182:48–52, 2020.

[76] Jiri Hajnys, Marek Pagac, J Mesicek, J Petru, and F Spalek. Research of 316l metallic powder for use in slm 3d printing. *Advances in Materials Science*, 20(1):5–15, 2020.

[77] Jacob C Simmons, Xiaobo Chen, Arad Azizi, Matthias A Daeumer, Peter Y Zavalij, Guangwen Zhou, and Scott N Schiffres. Influence of processing and microstructure on the local and bulk thermal conductivity of selective laser melted 316l stainless steel. *Additive Manufacturing*, 32:100996, 2020.

[78] John A Slotwinski and Edward J Garboczi. Metrology needs for metal additive manufacturing powders. *Jom*, 67(3):538–543, 2015.

[79] John J Dunkley. Metal powder atomisation methods for modern manufacturing. *Johnson Matthey Technology Review*, 63(3):226–232, 2019.

[80] K Geenen, A Röttger, and W Theisen. Corrosion behavior of 316l austenitic steel processed by selective laser melting, hot-isostatic pressing, and casting. *Materials and Corrosion*, 68(7):764–775, 2017.

[81] Shasha Lv, Huimin Tao, Yuanjian Hong, Yuanyuan Zheng, Chengshuang Zhou, Jinyang Zheng, and Lin Zhang. Surface treatment and corrosion behavior of 316l stainless steel fabricated by selective laser melting. *Materials Research Express*, 6(10):106518, 2019.

[82] MY Shaheen, AR Thornton, Stefan Luding, and Thomas Weinhart. Discrete particle simulation of the spreading process in additive manufacturing. In *Proceedings of the 8th International Conference on Discrete Element Methods (DEM8), The Netherlands*, 2019.

[83] R Narayan. Fundamentals of medical implant materials. *ASM handbook*, 2012.

[84] A Andrade, A Morcelli, and R Lobo. Deformation and fracture of an alpha/beta titanium alloy. *Matéria (Rio de Janeiro)*, 15(2):364–370, 2010.

[85] Daisuke Kuroda, Mitsuo Niinomi, Masahiko Morinaga, Yosihisa Kato, and Toshiaki Yashiro. Design and mechanical properties of new β type titanium alloys for implant materials. *Materials Science and Engineering: A*, 243(1-2):244–249, 1998.

[86] Saleem Hashmi. *Comprehensive materials finishing.* Elsevier, 2016.

[87] Donald M Brunette, Pentti Tengvall, Marcus Textor, and Peter Thomsen. *Titanium in medicine: material science, surface science, engineering, biological responses and medical applications.* Springer Science & Business Media, 2012.

[88] Buddy D Ratner. A perspective on titanium biocompatibility. In *Titanium in medicine*, pages 1–12. Springer, 2001.

[89] F ASTM. Standard specification for unalloyed titanium for surgical implant applications. *American Society for Testing and Materials, Philadelphia, PA*, 67, 67.

[90] Abdelrahman H Hussein, Mohamed A-H Gepreel, Mohamed K Gouda, Ahmad M Hefnawy, and Sherif H Kandil. Biocompatibility of new ti–nb–ta base alloys. *Materials Science and Engineering: C*, 61:574–578, 2016.

[91] MA Khan, Rachel L Williams, and David F Williams. The corrosion behaviour of ti–6al–4v, ti–6al–7nb and ti–13nb–13zr in protein solutions. *Biomaterials*, 20(7):631–637, 1999.

[92] SS Joseph and FH Froes. Titanium metallurgy and applications. *Light Met. Age*, 46(11):5–6, 1988.

[93] Carlos Oldani and Alejandro Dominguez. Titanium as a biomaterial for implants. *Recent advances in arthroplasty*, 218:149–162, 2012.

[94] F ASTM. 136-92: Standard specification for wrought ti-6a1-4v eli alloy for surgical implant applications. *Annual Book of ASTM Standards. Philadelphia, PA, American Society for Testing and Materials*, 1992.

[95] F ASTM. 1472-93: Standard specification for wrought ti-6a1-4v alloy for surgical implant applications. *Annual Book of ASTM Standards. Philadelphia, PA, American Society for Testing and Materials*, 1993.

[96] JC Wataha. Materials for endosseous dental implants. *Journal of oral rehabilitation*, 23(2):79–90, 1996.

[97] Luboš Řehounek. Mechanical and numerical analyses of titanium trabecular structures of dental implants formed by 3d printing. Master's thesis, CTU in Prague, Faculty of Civil Engineering, Department of Mechanics, 2016.

[98] R Prakash Kolli, William J Joost, and Sreeramamurthy Ankem. Phase stability and stress-induced transformations in beta titanium alloys. *Jom*, 67(6):1273–1280, 2015.

[99] R Kolli and Arun Devaraj. A review of metastable beta titanium alloys. *Metals*, 8(7):506, 2018.

[100] James D Cotton, Robert D Briggs, Rodney R Boyer, Sesh Tamirisakandala, Patrick Russo, Nikolay Shchetnikov, and John C Fanning. State of the art in beta titanium alloys for airframe applications. *Jom*, 67(6):1281–1303, 2015.

[101] Paul J Bania. Beta titanium alloys and their role in the titanium industry. *Jom*, 46:16–19, 1994.

[102] Qing Wang, Chuang Dong, and Peter K Liaw. Structural stabilities of β-ti alloys studied using a new mo equivalent derived from $[\beta/(\alpha+\ \beta)]$ phase-boundary slopes. *Metallurgical and Materials Transactions A*, 46:3440–3447, 2015.

[103] Mitsuo Niinomi. Recent metallic materials for biomedical applications. *Metallurgical and materials transactions A*, 33(3):477, 2002.

[104] Jose L Domingo. Vanadium: a review of the reproductive and developmental toxicity. *Reproductive Toxicology*, 10(3):175–182, 1996.

[105] Stephen C Bondy. The neurotoxicity of environmental aluminum is still an issue. *Neurotoxicology*, 31(5):575–581, 2010.

[106] Ma Geetha, Ashok K Singh, Rajamanickam Asokamani, and Ashok K Gogia. Ti based biomaterials, the ultimate choice for orthopaedic implants–a review. *Progress in materials science*, 54(3):397–425, 2009.

[107] Arne Biesiekierski, James Wang, Mohamed Abdel-Hady Gepreel, and Cuie Wen. A new look at biomedical ti-based shape memory alloys. *Acta biomaterialia*, 8(5):1661–1669, 2012.

[108] Pedro Akira Bazaglia Kuroda, Fernanda de Freitas Quadros, Karolyne dos Santos Jorge Sousa, Tatiani Ayako Goto Donato, Raul Oliveira De Araujo, and Carlos Roberto Grandini. Preparation, structural, microstructural, mechanical and cytotoxic characterization of as-cast ti-25ta-zr alloys. *Journal of Materials Science: Materials in Medicine*, 31:1–8, 2020.

[109] Qiang Li, Tengfei Liu, Junjie Li, Chao Cheng, Mitsuo Niinomi, Kenta Yamanaka, Akihiko Chiba, and Takayoshi Nakano. Microstructure, mechanical properties, and cytotoxicity of low young's modulus ti–nb–fe–sn alloys. *Journal of Materials Science*, 57(9):5634–5644, 2022.

[110] Giovana Collombaro Cardoso, Gerson Santos de Almeida, Dante Oliver Guim Corrêa, Willian Fernando Zambuzzi, Marília Afonso Rabelo Buzalaf, Diego Rafael Nespeque Correa, and Carlos Roberto Grandini. Preparation and characterization of novel as-cast ti-mo-nb alloys for biomedical applications. *Scientific Reports*, 12(1):11874, 2022.

[111] J Gunasekaran, P Sevvel, and I John Solomon. Metallic materials fabrication by selective laser melting: A review. *Materials Today: Proceedings*, 37:252–256, 2021.

[112] Thaisa T Oliveira and Andréa C Reis. Fabrication of dental implants by the additive manufacturing method: A systematic review. *The Journal of Prosthetic Dentistry*, 122(3):270–274, 2019.

[113] Hermann Karcher and Konrad Polthier. Construction of triply periodic minimal surfaces. 1996.

[114] Manfredo P Do Carmo. *Differential geometry of curves and surfaces: revised and updated second edition*. Courier Dover Publications, 2016.

[115] Luboš Řehounek and Aleš Jíra. Mesh generation and mechanical tests of basic element cells of porous structures. *Acta Polytechnica CTU Proceedings*, 34:80–84, 2022.

[116] Alan Hugh Schoen. *Infinite periodic minimal surfaces without self-intersections*, volume 5541. National Aeronautics and Space Administration, 1970.

[117] Dawei Li, Wenhe Liao, Ning Dai, Guoying Dong, Yunlong Tang, and Yi Min Xie. Optimal design and modeling of gyroid-based functionally graded cellular structures for additive manufacturing. *Computer-Aided Design*, 104:87–99, 2018.

[118] Jonathan Chin and Peter V Coveney. Chirality and domain growth in the gyroid mesophase. *Proceedings of the Royal Society A: Mathematical, Physical and Engineering Sciences*, 462(2076):3575–3600, 2006.

[119] Luboš Řehounek, Aleš Jíra, and František Denk. Influence of dental caries for dental materials and their micromechanical properties. In *Applied Mechanics and Materials*, volume 827, pages 371–374. Trans Tech Publ, 2016.

[120] Petra Hájková. Mikromechanické hodnocení dentinu a skloviny s ohledem na mechanické vlastnosti umělých materiálů užívaných ve stomatochirurgii. Master's thesis, České vysoké učení technické v Praze, Thákurova 2077/7, 166 29 Praha 6, 2018.

[121] Luboš Řehounek. Mechanical and numerical analyses of titanium trabecular structures of dental implants formed by 3d printing. *Acta Polytechnica*, 57(3):218–228, 2017.

[122] Aleš Jíra. Organické struktury jako základ inženýrských aplikací. Habilitation thesis, CTU in Prague, Faculty of Civil Engineering, Department of Mechanics, 2021.

[123] Tomáš Krejčí, Luboš Řehounek, Aleš Jíra, Michal Šejnoha, Jaroslav Kruis, and Tomáš Koudelka. Homogenization of elastic properties of trabecular structures for modern implants. In *AIP Conference Proceedings*, volume 2293, page 190008. AIP Publishing LLC, 2020.

[124] Aleš Jíra, Michal Šejnoha, Tomáš Krejčí, Jan Vorel, Luboš Řehounek, and Guido Marseglia. Mechanical properties of porous structures for dental implants: Experimental study and computational homogenization. *Materials*, 14(16):4592, 2021.

[125] International Standard. ISO 13314 Mechanical testing of metals, ductility testing, compression test for porous and cellular metals. *Reference number ISO*, 13314(13314):1–7, 2011.

[126] Oraib Al-Ketan and Rashid K Abu Al-Rub. Mslattice: A free software for generating uniform and graded lattices based on triply periodic minimal surfaces. *Material Design & Processing Communications*, page e205, 2020.

[127] The Mathworks Inc. MATLAB software version: 9.13.0 (R2022b). `https://www.mathworks.com`.

[128] Nadim J Hallab and Joshua J Jacobs. Biologic effects of implant debris. *Bulletin of the NYU hospital for joint diseases*, 67(2), 2009.

[129] Chenxi Peng and Phuong Tran. Bioinspired functionally graded gyroid sandwich panel subjected to impulsive loadings. *Composites Part B: Engineering*, 188:107773, 2020.

[130] Philip Bean, Roberto A Lopez-Anido, and Senthil Vel. Numerical modeling and experimental investigation of effective elastic properties of the 3d printed gyroid infill. *Applied Sciences*, 12(4):2180, 2022.

[131] ANSYS SpaceClaim Software v. 2023 R1. `https://www.ansys.com/products/3d-design/ansys-spaceclaim?spaceclaimredirect`.

[132] ANSYS Workbench Software v. 2023 R1. `https://www.ansys.com/products/ansys-workbench`.

[133] MECHANICAL FINDER. `https://mechanical-finder.com/`. Accessed: 2023-03-15.

[134] ANSYS ICEM CFD. `https://www.ansys.com/`. Accessed: 2023-03-15.

[135] Yixin Hu, Teseo Schneider, Bolun Wang, Denis Zorin, and Daniele Panozzo. Fast tetrahedral meshing in the wild. *ACM Trans. Graph.*, 39(4), July 2020.

[136] DR Dance, S Christofides, ADA Maidment, ID McLean, and KH Ng. Diagnostic radiology physics: A handbook for teachers and students. endorsed by: American association of physicists in medicine, asia-oceania federation of organizations for medical physics, european federation of organisations for medical physics. 2014.

[137] Joyce H Keyak, Stephen A Rossi, Kimberly A Jones, and Harry B Skinner. Prediction of femoral fracture load using automated finite element modeling. *Journal of biomechanics*, 31(2):125–133, 1997.

[138] Daniel Charles Drucker and William Prager. Soil mechanics and plastic analysis or limit design. *Quarterly of applied mathematics*, 10(2):157–165, 1952.

[139] Leandro R Alejano and Antonio Bobet. Drucker–prager criterion. *The ISRM Suggested Methods for Rock Characterization, Testing and Monitoring: 2007-2014*, pages 247–252, 2015.

[140] Stephen Davies. What is occlusion? In *A Guide to Good Occlusal Practice*, pages 1–22. Springer, 2022.

[141] MC Raadsheer, TMGJ Van Eijden, FC Van Ginkel, and B Prahl-Andersen. Contribution of jaw muscle size and craniofacial morphology to human bite force magnitude. *Journal of dental research*, 78(1):31–42, 1999.

[142] José Henrique Rubo and Edson Antonio Capello Souza. Finite-element analysis of stress on dental implant prosthesis. *Clinical implant dentistry and related research*, 12(2):105–113, 2010.

[143] Sergio ET Quaresma, Patricia R Cury, Wilson R Sendyk, and Claudio Sendyk. A finite element analysis of two different dental implants: stress distribution in the prosthesis, abutment, implant, and supporting bone. *Journal of Oral Implantology*, 34(1):1–6, 2008.

[144] Liang-jian Chen, HE Hao, Yi-Min Li, LI Ting, Xiao-Ping Guo, and Rui-Fang Wang. Finite element analysis of stress at implant–bone interface of dental implants with different structures. *Transactions of Nonferrous Metals Society of China*, 21(7):1602–1610, 2011.

[145] Oğuz Kayabaşı, Emir Yüzbasıoğlu, and Fehmi Erzincanlı. Static, dynamic and fatigue behaviors of dental implant using finite element method. *Advances in engineering software*, 37(10):649–658, 2006.

[146] Heng-Li Huang, Chin-Han Chang, Jui-Ting Hsu, Alison M Faligatter, and Ching-Chang Ko. Comparison of implant body designs and threaded designs of dental implants: a 3-dimensional finite element analysis. *International Journal of Oral & Maxillofacial Implants*, 22(4), 2007.

[147] Laurent Pierrisnard, Guy Hure, Michel Barquins, and Daniel Chappard. Two dental implants designed for immediate loading: a finite element analysis. *International Journal of Oral & Maxillofacial Implants*, 17(3), 2002.

[148] Petr Marcián, Jan Wolff, Ladislava Horáčková, Jozef Kaiser, Tomáš Zikmund, and Libor Borák. Micro finite element analysis of dental implants under different loading conditions. *Computers in Biology and Medicine*, 96:157–165, 2018.

[149] Jian-Ping Geng, Keson BC Tan, and Gui-Rong Liu. Application of finite element analysis in implant dentistry: a review of the literature. *The Journal of prosthetic dentistry*, 85(6):585–598, 2001.

[150] ER Teixeira, Y Sato, Y Akagawa, and N Shindoi. A comparative evaluation of mandibular finite element models with different lengths and elements for implant biomechanics. *Journal of oral rehabilitation*, 25(4):299–303, 1998.

[151] Abani K Patra, Jason M DePaolo, Karl S D'Souza, Daniel DeTolla, and Michael A Meenaghan. Guidelines for analysis and redesign of dental implants. *Implant Dentistry*, 7(4):355–368, 1998.

[152] Jie Yang and Hong-Jun Xiang. A three-dimensional finite element study on the biomechanical behavior of an fgbm dental implant in surrounding bone. *Journal of biomechanics*, 40(11):2377–2385, 2007.

[153] RC Van Staden, Hong Guan, and Yew-Chaye Loo. Application of the finite element method in dental implant research. *Computer methods in biomechanics and biomedical engineering*, 9(4):257–270, 2006.

[154] Mária Frolo, Luboš Řehounek, Aleš Jíra, Petr Pošta, and Lukáš Hauer. Biomechanical analysis of palateless splinted and unsplinted maxillary implant-supported overdentures: A three-dimensional finite element analysis. *Materials*, 16(15):5248, 2023.

[155] M Taruna, B Chittaranjan, N Sudheer, Suchita Tella, and MD Abusaad. Prosthodontic perspective to all-on-4® concept for dental implants. *Journal of clinical and diagnostic research: JCDR*, 8(10):ZE16, 2014.

[156] Luis Vega, Rachel Strait, and Tyler E Ames. Bar-retained zygomatic implant overdenture as a first line of treatment. *Compendium*, 43(7), 2022.

[157] Gerald Krennmair and Eva Piehslinger. Removable implant-supported maxillary prostheses anchored on milled bars: a retrospective evaluation of two concepts. *International Journal of Prosthodontics*, 22(6), 2009.

[158] L Tang, JP Lund, R Tache, CML Clokie, and JS Feine. A within-subject comparison of mandibular long-bar and hybrid implant-supported prostheses: psychometric evaluation and patient preference. *Journal of dental research*, 76(10):1675–1683, 1997.

[159] Steven J Sadowsky. Mandibular implant-retained overdentures: a literature review. *The Journal of prosthetic dentistry*, 86(5):468–473, 2001.

[160] Sven Rinke, Hajo Rasing, Nikolaus Gersdorff, Ralf Buergers, and Matthias Roediger. Implant-supported overdentures with different bar designs: A retrospective evaluation after 5-19 years of clinical function. *The journal of advanced prosthodontics*, 7(4):338–343.

[161] Gerald Krennmair, Martin Krainhöfner, and Eva Piehslinger. The influence of bar design (round versus milled bar) on prosthodontic maintenance of mandibular overdentures supported by 4 implants: a 5-year prospective study. *Int J Prosthodont*, 21(6):514–520, 2008.

[162] Marina Andreiotelli, Wael Att, and Jörg-Rudolf Strub. Prosthodontic complications with implant overdentures: a systematic literature review. *Int J Prosthodont*, 23(3):195–203, 2010.

[163] Gerald Krennmair, Martin Krainhöfner, and Eva Piehslinger. Implant-supported mandibular overdentures retained with a milled bar: a retrospective study. *International Journal of Oral & Maxillofacial Implants*, 22(6), 2007.

[164] Karl Martin Lehmann, Peer W Kämmerer, Julia Karbach, Herbert Scheller, Bilal Al-Nawas, Wilfried Wagner, et al. Long-term effect of overdenture bar design on peri-implant tissues. *Int J Oral Maxillofac Implants*, 28(4):1126–1131, 2013.

[165] Standardization IOf. International standard iso 14801–dentistry–implants-dynamic fatigue test for endosseous dental implants. *Geneva: International Organization for Standardization*, 2007.

[166] Luboš Řehounek, Aleš Jíra, Gabriela Javorská, and Daniel Bodlák. Numerical comparison of transgingival and subgingival dental implants in regard to their stress distributions. *Acta Polytechnica CTU Proceedings*, 30:81–86, 2021.

[167] Luboš Řehounek, Aleš Jíra, Gabriela Javorská, and Daniel Bodlák. Numerical comparison of transgingival and subgingival dental implants in regard to their stress distributions. *Acta Polytechnica CTU Proceedings*, 30:81–86, 2021.

[168] Semih Benli, Sami Aksoy, Hasan Havıtcıoğlu, and Mumin Kucuk. Evaluation of bone plate with low-stiffness material in terms of stress distribution. *Journal of Biomechanics*, 41(15):3229–3235, 2008.

[169] Luboš Řehounek. Experimental micromechanical analysis of the tooth dentin. Bachelor’s thesis, CTU in Prague, Faculty of Civil Engineering, Department of Mechanics, 2015.